2003-11-03

A Closed-Form Dynamic Model of the Compliant Constant-Force Mechanism Using the Pseudo-Rigid-Body Model

Cameron Boyle
Brigham Young University - Provo

BYU ScholarsArchive Citation

Boyle, Cameron, "A Closed-Form Dynamic Model of the Compliant Constant-Force Mechanism Using the Pseudo-Rigid-Body Model" (2003). *Theses and Dissertations*. 53.
https://scholarsarchive.byu.edu/etd/53

A CLOSED-FORM DYNAMIC MODEL OF THE COMPLIANT CONSTANT-FORCE MECHANISM USING THE PSEUDO-RIGID-BODY MODEL

by

Cameron L. Boyle

A thesis submitted to the faculty of

Brigham Young University

in partial fulfillment of the requirements for the degree of

Master of Science

Department of Mechanical Engineering

Brigham Young University

August 2001

BRIGHAM YOUNG UNIVERSITY

GRADUATE COMMITTEE APPROVAL

of a thesis submitted by

Cameron L. Boyle

This thesis has been read by each member of the following graduate committee and by majority vote has been found to be satisfactory.

Date	Mark S. Evans, Chair
Date	Larry L. Howell
Date	Craig C. Smith

BRIGHAM YOUNG UNIVERSITY

As chair of the candidate's graduate committee, I have read the thesis of Cameron L. Boyle in its final form and have found that (1) its format, citations, and bibliographical style are consistent and acceptable and fulfill university and department style requirements; (2) its illustrative materials including figures, tables, and charts are in place; and (3) the final manuscript is satisfactory to the graduate committee and is ready for submission to the university library.

Date

Mark S. Evans
Chair, Graduate Committee

Accepted for the Department

Craig C. Smith
Graduate Coordinator

Accepted for the College

Douglas M. Chabries
Dean, College of Engineering and Technology

ABSTRACT

A CLOSED-FORM DYNAMIC MODEL OF THE COMPLIANT CONSTANT-FORCE MECHANISM USING THE PSEUDO-RIGID-BODY MODEL

Cameron L. Boyle

Department of Mechanical Engineering

Master of Science

A mathematical dynamic model is derived for the compliant constant-force mechanism, based on the pseudo-rigid-body model simplification of the device. The compliant constant-force mechanism is a slider mechanism incorporating large-deflection beams, which outputs near-constant-force across the range of its designed deflection. The equation of motion is successfully validated with empirical data from five separate mechanisms, comprising two configurations of compliant constant-force mechanism. The dynamic model is cast in generalized form to represent all possible configurations of compliant constant-force mechanism. Deriving the dynamic equation from the pseudo-rigid-body model is useful because every configuration is represented by the same model, so a separate treatment is not required for each configuration. An unexpected dynamic trait of the constant-force mechanism is discovered: there exists a range of frequencies for which the output force of the mechanism accords nearer to constant-force than does the output force at static levels.

ACKNOWLEDGEMENTS

I wish to thank the many friends and associates who helped in this endeavor.

Dr. Mark S. Evans directed and instructed me through every phase of the research, and his guidance has been invaluable. Dr. Larry Howell and Dr. Craig Smith as committee members also spent time and effort helping to resolve new issues as the research developed. I would also like to thank Dr. Spencer Magelby, as a director of the Center of Excellence for Compliant Mechanisms, for advisory help. Their time and support is greatly appreciated.

Many thanks go to Scott Lyon, who selflessly spent many hours helping me "master" the art of instrumentation, from building analog filters to eliminating ground loops, and then helping me analyze the data. I would like to thank Brent Weight for his experience with constant-force mechanisms, his suggestions for manufacturing them, and his finite-element modeling skills. Thanks also to Keith Neilson for helping me with signal processing. I would like to thank everyone in the lab for their approachability in helping me tackle various problems, and for their friendship.

I express gratitude to my parents for their constant love and support. Finally, I would like to thank my wife, Jueneta, for her abiding love and endless patience.

This research was supported by funding from the Utah Center of Excellence Program.

Table of Contents

List of Tables

List of Figures

CHAPTER 1 Introduction

1.1 Thesis Statement

The purpose of this thesis is (1) to illuminate the dynamic behavior of compliant constant-force mechanisms, and (2) to further evaluate the pseudo-rigid-body model as a dynamic modeling tool.

This thesis hypothesizes that the pseudo-rigid-body model, a proven technique for static design and analysis of compliant mechanisms, can be used to derive a viable closed-form dynamic model of the compliant constant-force mechanism. A dynamic model is derived for a common constant-force mechanism configuration and then generalized to all configurations. Experimental validation of the model is performed with five mechanisms, comprising two constant-force mechanism configurations. Dynamic phenomena unique to the compliant constant-force mechanism are then explored.

1.2 Background

1.2.1 COMPLIANT MECHANISMS AND THE PSEUDO-RIGID-BODY MODEL

The emergence of the pseudo-rigid-body model in recent years coincides with the building realization of the aptness of compliance in engineering. Even a cursory look at the natural world reveals the strength and ofttimes superiority of compliance, such as the flexible wings of a bee or hummingbird, the contraction and springing back of the heart as it pumps, or the versatility of the human hand and wrist (Vogel, 1995). However, nature is difficult to mimic because of the complex nonlinear analysis required to understand all but small-deflection compliance. The pseudo-rigid-body model is a method of circumventing some of the obstacles that arise when engineering compliance into mechanical devices. It provides a welcome middle ground between designing merely by trial and error, and devising exact mathematical formulations.

Compliant mechanisms are mechanisms that obtain some or all of their motion through the deflection of flexible members. Historically, the most common method of compliant mechanism design has been trial and error. However, the conception of the pseudo-rigid-body modeling technique has successfully opened the way for simple design and analysis of many compliant mechanisms (Howell et al., 1996). The premise of the pseudo-rigid-body model is that many compliant mechanisms behave sufficiently similar to a corresponding rigid-body mechanism, making it possible to perform analysis on the rigid-body mechanism instead. Rigid-body mechanisms, as opposed to compliant mechanisms, are well understood and more readily lend themselves to conventional analysis. The pseudo-rigid-body model's assumptions adhere remarkably well to the actual kinematics of a wide variety of compliant mechanisms.

The pseudo-rigid-body model has been used almost exclusively for static kinematic design and modeling, where dynamic effects are not a large factor in mechanism performance. The fact that the pseudo-rigid-body model has a proven track record as a reliable predictor of static kinematics for compliant mechanisms (Millar et al., 1996; Howell et al., 1996) begs the question, how well would the pseudo-rigid-body model account for dynamic effects? This thesis addresses the desire to understand how certain compliant mechanisms behave dynamically, namely compliant constant-force mechanisms and mechanisms incorporating compliant constant-force mechanisms. This understanding is attempted by using the pseudo-rigid-body model.

1.2.2 COMPLIANT CONSTANT-FORCE MECHANISMS

A constant-force mechanism yields a constant output force over a range of input displacements. Constant-force mechanisms are useful in applications requiring a constant force to be applied to a time-varying or non-uniform surface, such as grinding, swiping, deburing, welding, and assembly. They may also be used to maintain constant force between electrical connectors regardless of part tolerances; as gripping devices to hold delicate parts of varying size; for wear testing, where a constant force must be applied to a surface even as the surface is worn; in manufacturing processes that involve tool diameter changes such as grinding or honing; or as safety valves to maintain a system at constant pressure when power is lost. In these and other applications, the constant-force mechanism eliminates the need for expensive and elaborate force control, replacing it with a simple mechanical device (Evans and Howell, 1999).

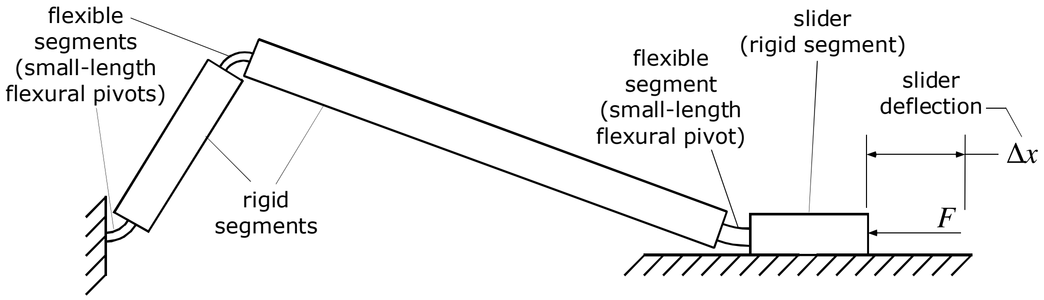

Figure 1.1 A compliant slider mechanism.

Compliant constant-force mechanisms are essentially compliant slider mechanisms with flexible and rigid segment dimensions optimized to minimize the variation in the output force over a designed range of displacement. Consider the compliant slider mechanism depicted in Figure 1.1. Given an input displacement Δx, a compliant constant-force mechanism will yield the same force F over the full range of its designed deflection, plus or minus a small variation.

There exist 28 possible configurations of the compliant constant-force mechanism, identified by type synthesis techniques (Howell, 2001). Of these, fifteen configurations are illustrated in Figure 1.2 (Millar et al., 1996). Experimental validation of dynamic models of two of these configurations is performed in this thesis, and a generalized dynamic model representing all 28 configurations is presented.

1.3 Motivation for the Research

The constant-force mechanism provides a constant-force output for various deflections. One way to make such a mechanism deviate from constant-force is by compressing

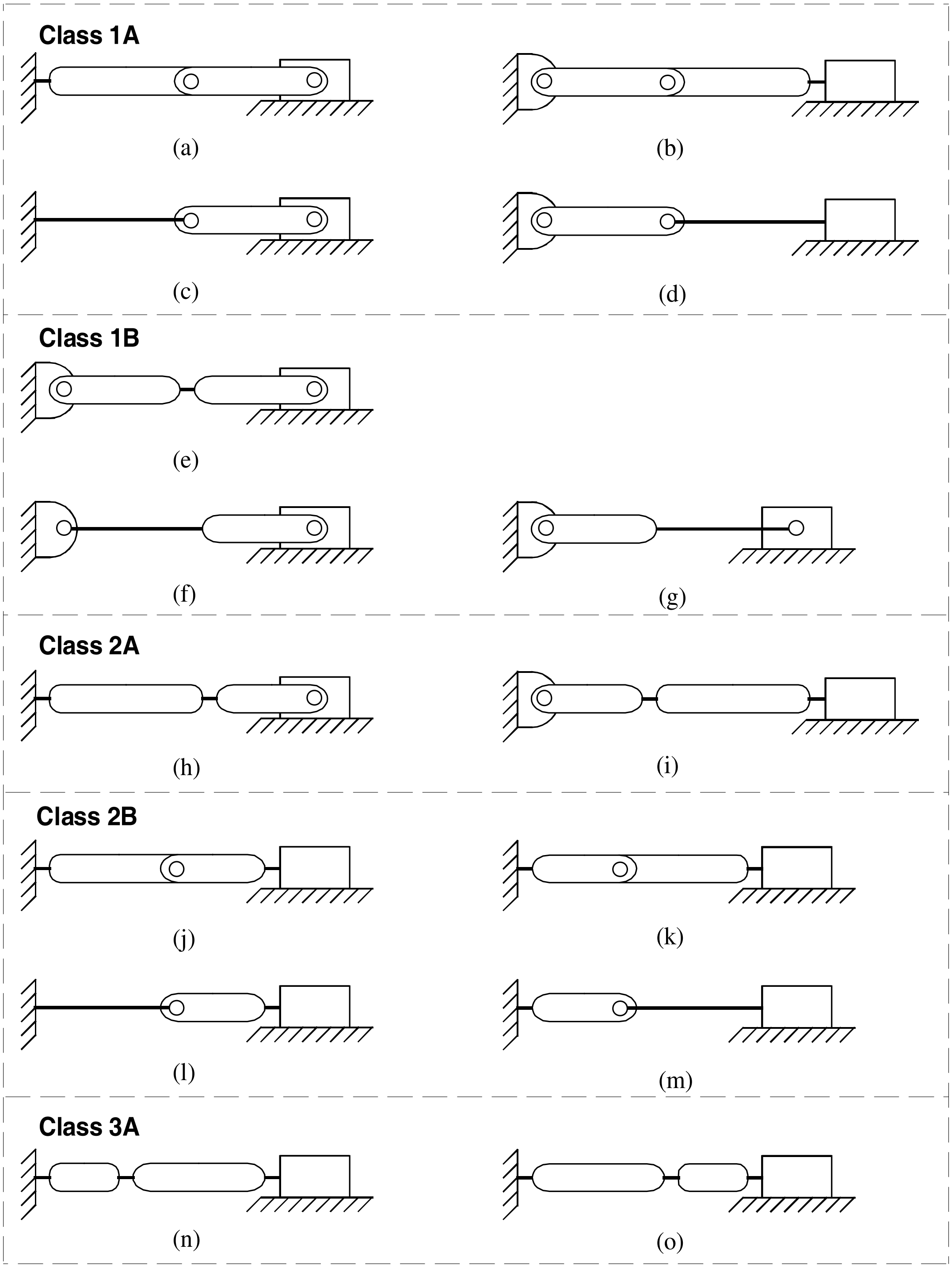

Figure 1.2 Fifteen configurations of the compliant constant-force mechanism. Flexible segments are depicted by a single line, and rigid segments are depicted by two parallel lines.

it beyond its designed deflection. Another way is to subject it to dynamic motion, interfering with the device's static constant-force characteristics. Under what dynamic conditions does the output of a constant-force device depart significantly from its static force behavior?

In answering this question, a simple method for modeling the dynamic response of constant-force mechanisms would be useful. Of course, many approaches to modeling compliant mechanisms exist, few of which are very simple or intuitive (these will be discussed in more detail in Chapter 2). Ideally, a simpler method for obtaining a viable closed-form dynamic model would be desirable. Because the constant-force mechanism was discovered through application of the pseudo-rigid-body model (Howell, 1994), it follows that the same model might be used to adequately describe its dynamics. Another reason for selecting the pseudo-rigid-body model as an aid in dynamics modeling is to test its ability to predict the dynamic response of compliant mechanisms in general.

The pseudo-rigid-body model approximates the deflection and force characteristics of a complaint mechanism's flexible members by assigning them torsional spring and rigid-link counterparts. Applying the model to the entire compliant mechanism using a series of heuristic rules results in a rigid-link model. Herein lies the power of the pseudo-rigid-body model: its ability to convert a difficult-to-analyze compliant mechanism into a familiar rigid-body mechanism which can be analyzed using traditional kinematics. The model does not represent compliant mechanisms perfectly, but it has been shown to represent them very well, making it a powerful design tool. Though the pseudo-rigid-body model has been shown to be valid for the static analysis of compliant mechanisms, very little research has been performed to explore the usefulness of the pseudo-rigid-body model in dynamic analysis. If the model can be shown to approximate well the dynamic response of compliant mechanisms, then its usefulness is extended even further.

It was anticipated from the outset that the pseudo-rigid-body model would approximate actual mechanism dynamics well, because the model's transformation from compliant mechanism to rigid-link mechanism does not result in a significant redistribution of mass. This is readily seen in the pseudo-rigid-body model examples of Chapters 3 and 6, and in APPENDIX A, *Pseudo-Rigid-Body Model*. The pseudo-rigid-body model makes large assumptions by lumping a compliant mechanism's distributed compliance at distinct points; but the changes it makes to the mechanism's distribution of mass are very small, so modeled and actual dynamic inertial forces should be reasonably consistent. Inertial forces acting on the mechanism masses, it is assumed, dominate over other dynamic forces.

1.4 Research Contributions

The main contribution of this research is that it adds to the body of knowledge concerning compliant constant-force mechanisms. A closed-form dynamic model based on the pseudo-rigid-body model of the compliant mechanism is derived, elucidating the dynamic behavior of compliant constant-force mechanisms. The relative simplicity of employing the pseudo-rigid-body model to streamline the dynamic analysis, compared with existing dynamical methods (described in Chapter 2), combined with the fact that the dynamic model can be represented mathematically, is a large step forward. Empirical results show the dynamic model's validity, and a closer examination of the dynamic response of the mechanism as a function of frequency reveals a dynamic effect that promises to be quite useful in constant-force mechanism design (see Section 5.2 *Dynamic Characterization of the Model* on page 44).

This thesis also evaluates how effectively the pseudo-rigid-body model can be used to predict the dynamic response of compliant mechanical systems. It is hoped that this research will extend the pseudo-rigid-body model's usefulness as a design and modeling tool, beyond static systems to systems in which dynamics play a large part in mechanism performance.

1.5 Thesis Outline

Chapter 2, *Review of Literature*, concludes the introductory material with a review of literature pertinent to the area. Chapter 3, *Dynamic Model*, presents the derivation of a closed-form dynamic model based on the pseudo-rigid-body model of a selected configuration of compliant constant-force mechanism. Chapter 4, *Experimental Setup*, describes the design of a constant-force mechanism used to validate the dynamic model, the equipment and instrumentation used to collect the data, and how the data was processed. Chapter 5, *Empirical and Theoretical Findings*, presents the data collected from the test mechanism of Chapter 4 and compares it to that predicted by the dynamic model of Chapter 3. The performance of the dynamic model is evaluated, and an unexpected dynamic effect is examined. Chapter 6, *Generalized Dynamic Model*, introduces a dynamic model based on the existing derivation, only generalized for all configurations of compliant constant-force compression mechanism. Chapter 7, *Testing of Additional Mechanisms*, gives the results of tests performed on four additional constant-force mechanisms, two of the same configuration as the mechanism of Chapter 4, and two of a different configuration. Finally, Chapter 8, *Conclusions and Recommendations*, reviews important aspects of the work and recommends further areas of study.

CHAPTER 2 Review of Literature

Important topics covered in this work include compliant mechanism modeling, static and dynamic analysis of flexible-body mechanisms, the pseudo-rigid-body model, and constant-force mechanisms.

2.1 Compliant Mechanism Modeling (Static and Dynamic)

Along with the emergence of the pseudo-rigid-body modeling technique in recent years, other methods for designing and/or analyzing large-deflection compliant mechanisms have arisen, including both static and dynamic methods. One approach is the formulation of an exact mathematical model to describe large-deflection beam mechanisms. Bisshopp and Drucker (1945), Burns and Crossley (1968), and Sevak and McLarnan (1974) used elliptic integral solutions to derive ordinary nonlinear differential equations to represent cantilever beam mechanisms. Simo and Posbergh (1988) performed a geometrically exact formulation of a three-dimensional compliant rod coupled with a rigid body, with no restriction on the degree of flexibility. Wang (1997) set up a dynamic equation to describe the dynamics of an elastic four-bar linkage mechanism with large elastic deformation. Atanackovic and Cveticanin (1996) developed coupled partial differential equations in two coordinate systems to model the dynamic response of an unloaded pinned-roller beam under compression. Recently, Panza (2000) published a nonlinear integro-partial differential equation representing the large-deflection dynamics of a compliant beam mechanism, incorporating mass loading and friction/damping effects.

A much more common approach to modeling compliant mechanisms is applying nonlinear finite-element modeling techniques in one form or another. One novel approach uses structural optimization to determine possible topologies a compliant mechanism can have in order to meet a specified force-displacement relationship (Ananthasuresh & Kota, 1995). For dynamic analysis, many methods have been successful, from the use of finite rotation theory (Honke et al., 1997; Sugano et al., 1999) and Extended Bond Graph formulation (Yen and Masada, 1994), to the use of Flexible Multibody Dynamics methods such as Floating Frame of Reference, Incremental Finite Element, Finite Segment, and Absolute Nodal Coordinate (Megahed and Hamza, 2000) techniques. Another approach to dynamic modeling is the work of Pascal and Gagarina (1999), who discretized flexible components by a Rayleigh-Ritz procedure, and then numerically simulated the dynamic response using dynamical codes devoted to rigid multibody systems. Similar work was performed by Petroka and Chang (1989), Darcovich (1992), and Zakhariev (1999).

Lyon et al. (1997) used the pseudo-rigid-body model in conjunction with Lagrange's method to develop linear ordinary differential equations that successfully described compliant parallel-guiding mechanisms. It is the only work to date that investigates the possibility of using the pseudo-rigid-body model to predict the dynamic response of compliant mechanisms. This thesis represents the second work exploring the use of the pseudo-rigid-body model to predict the dynamic behavior of compliant mechanisms.

Note that for many of the dynamic modeling techniques reviewed in this section it is difficult, if not impossible, to obtain a mathematical model. A mathematical solution is easily obtained by using the pseudo-rigid-body model to derive a dynamic equation, as demonstrated by this work.

2.2 Constant-Force Mechanisms

Using a synthesis technique, Jenuwine and Midha (1989) developed an exact constant-force mechanism incorporating linear springs and rigid links. The many configurations of compliant constant-force slider mechanism, inspired by this original rigid-body device, came about later through topological synthesis (Howell et al., 1994). Each of these appear in United States Patent No. 5,649,454 (Midha et al., 1995).

Millar et al. (1996) presents a detailed development of compliant constant-force mechanism theory, with static validation of three configurations. The validation shows the theory to be sound, barring what was assumed to be undesirable friction in the joints.

Evans and Howell (1999) designed and constructed a robotic end-effector coupling device, pictured in Figure 2.1, incorporating compliant constant-force mechanisms. It acted as a coupling device between a robotic arm and its end-effector, for instance a glass-cutter or grinder. The end-effector mechanism was made of four constant-force mechanisms placed between two end plates and a center cage, allowing the mechanisms to compress as pairs in two symmetric stages. Throughout its range of compression, the

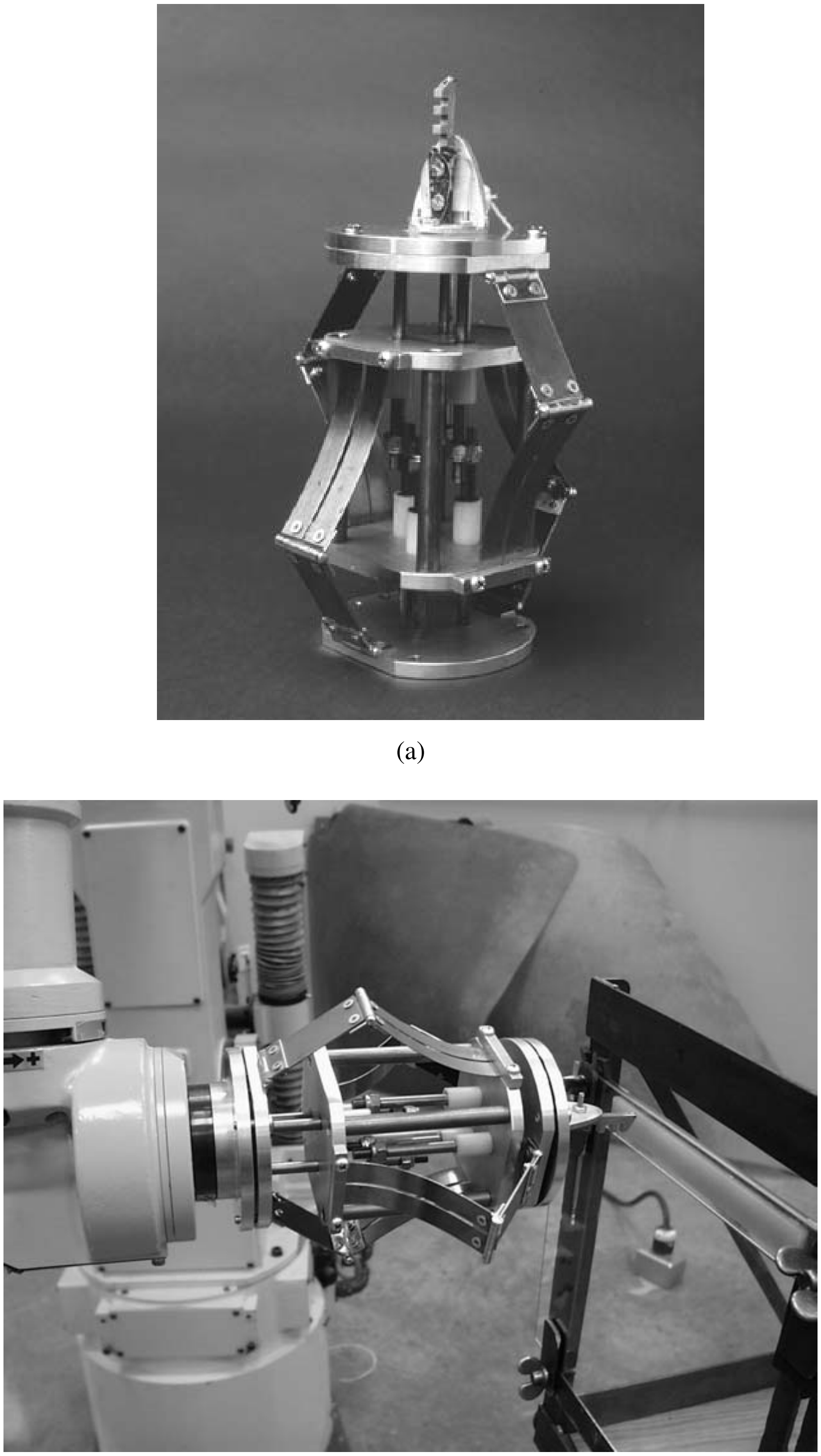

(a)

(b)

Figure 2.1 Robotic end-effector coupling device (a) on display and (b) successfully scoring a pane of glass oriented out-of-plane of the robot arm's path; even with severe misalignment of the glass, the end-effector deflects with a constant-force and does not break the glass.

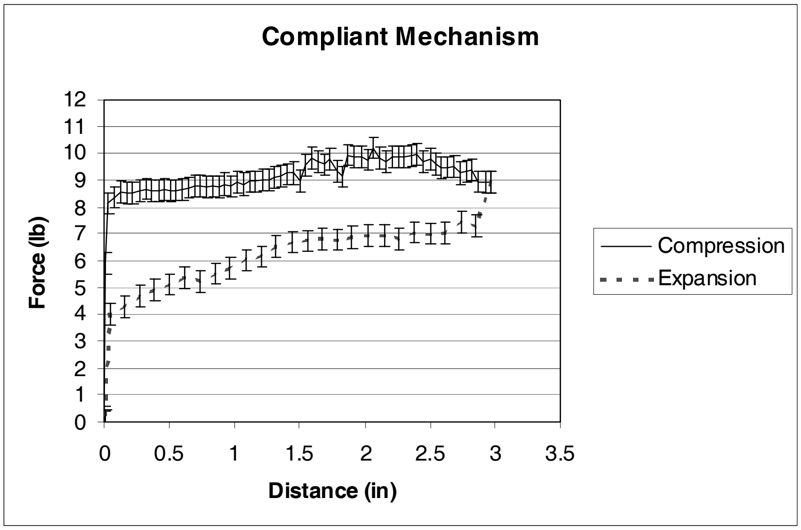

Figure 2.2 Measured force from a static test of the end-effector coupling device.

coupler caused the end-effector to exert a near-constant-force on any surface or object to which the end-effector was applied. For instance, as depicted in Figure 2.1 (b), the prototype demonstrated that it could successfully score a pane of glass without breaking it, even though the glass was grossly misaligned with the path of the robot arm.

The end-effector device was tested to verify that, statically, it would output near-constant-force of the magnitude specified in its design, approximately 40 *N* (9 lb_f). The experimental results are repeated in Figure 2.2 because they illustrate an important issue dealt with in this work. The measured force deviated from the predicted 40 *N* output force in two ways. First, the average output force over both compression and expansion of the device were below 40 *N* (9 lb_f). Second, the force output of the mechanism was higher in compression than in expansion. Evans and Howell attributed the first deviation to "minor flexibility of the portion of the compliant mechanism that was assumed to be rigid." The rigid link of each constant-force mechanism in the device was made of steel sheet metal which was approximately twice as thick as the spring steel was used for the flexible links. The second deviation was attributed to friction between the pistons, bushings, and pin-joints of the device, which acted to oppose the motion of the device. While the device was being compressed, the frictional forces opposed the direction of the output force, and vice versa when the device was allowed to expand. This friction caused the actual output force of the device to band the predicted output force of the device by an amount proportional to the level of friction.

CHAPTER 3 Dynamic Model

Recall that the dual undertaking of this thesis is to further evaluate the pseudo-rigid-body model as a dynamics modeling tool, and to illuminate the dynamic behavior of constant-force mechanisms. This chapter presents the derivation of a closed-form dynamic model for constant-force mechanism configuration “Class 1A-d,” as designated in Figure 1.2.

First, the compliant mechanism is modeled as a rigid-body mechanism with lumped compliance using the pseudo-rigid-body model. Converting the mechanism to its rigid-body counterpart greatly simplifies kinematic and dynamic analysis by allowing the use of rigid-body modeling techniques. Lagrange’s method is then used to obtain an equation of motion for the mechanism. The constant-force mechanism has only one degree of freedom, so only one generalized coordinate and one instance of Lagrange’s equation are required. The choice of non-conservative forces included in the generalized force is explained, as well as any assumptions made by the model.

What is important in the derivation is not the method chosen to arrive at the closed-form dynamic model (in this case Lagrange’s method), but the fact that the method is applied to the pseudo-rigid-body simplification of the mechanism. The dynamic model obtained is faithful to the pseudo-rigid-body model of the mechanism, not necessarily to the compliant mechanism itself.

Test data from a constant-force mechanism of the same configuration (Class 1A-d) will be presented in Chapter 5. As discussed in Section 1.3 *Motivation for the Research* on page 4, it was expected from the outset of this research that a dynamic model derived from the pseudo-rigid-body model of a compliant mechanism would approximate its actual dynamic response well. How closely the dynamic model response matches the measured response of a constant-force mechanism will substantiate or invalidate this hypothesis.

3.1 Selection of a Configuration

Recall from Figure 1.2 that there are a number of different configurations of compliant constant-force mechanism. The configuration modeled in this chapter is configuration Class 1A-d, illustrated again in Figure 3.1. It consists of a rigid link pinned to ground and to a long flexible segment rigidly connected to a slider. This configuration was chosen for its ease of manufacturability, and because it is the same configuration of constant-force spring used in the robotic end-effector prototype (see page 14). Experimental validation of a model for this configuration will lead to a better understanding of the end-effector device as a whole.

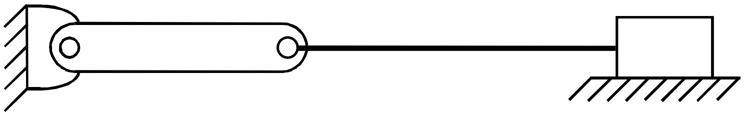

Figure 3.1 Compliant constant-force mechanism, configuration Class 1A-d.

3.2 The Pseudo-Rigid-Body Model

The pseudo-rigid-body model of constant-force spring, configuration Class 1A-d, is shown in Figure 3.2. The mechanism is converted to its rigid-body counterpart by using the pseudo-rigid-body model rule for a cantilever beam with a force at the free end (see APPENDIX A), as described below.

The flexible segment of length l is replaced by two rigid links, links 3 and 6, with lengths r_3 and r_6. Link 3's length is determined by the relation for the pseudo-rigid-body link's characteristic radius,

$$r_3 = \gamma l \tag{3.1}$$

where γ is the characteristic radius factor. The length of link 6 is then

$$r_6 = l - r_3 \tag{3.2}$$

The compliance of the flexible segment is represented by a torsional spring at the new pin ("characteristic pivot") joining links 3 and 6. The torsional spring constant k for a cantilever beam with a force at the free end is given by

$$k = \gamma K_\Theta \frac{EI}{l} \tag{3.3}$$

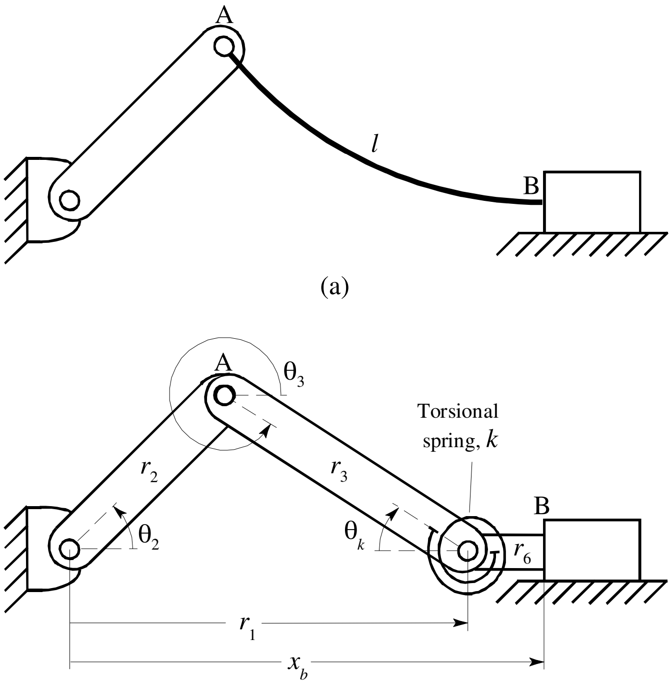

Figure 3.2 (a) Compliant constant-force mechanism, configuration Class 1A-d, and (b) its pseudo-rigid-body model.

where K_Θ is the stiffness coefficient (a nondimensionalized torsional spring constant), E is the modulus of elasticity of the flexible segment, and I is the moment of inertia of the flexible segment.

The average values of γ and K_Θ over a wide range of loading conditions are used:

$$\gamma = 0.85 \qquad K_\Theta = 2.65 \tag{3.4}$$

For a more accurate k that changes with deflection of the flexible segment, γ and K_Θ can be expressed as functions of end-load angle, but equation (3.4) gives the average values most commonly used in pseudo-rigid-body model calculations.

When the pseudo-rigid-body angle θ_k is zero, the torsional spring is undeflected and stores no strain energy. It is assumed that no plastic deformation occurs as the mechanism cycles and the flexible segment deflects.

As seen in Figure 3.2, application of the pseudo-rigid-body model to the mechanism does not result in a significant redistribution of its mass. Accordingly, dynamic inertial forces on the mechanism should be reasonably consistent between the compliant mechanism and its pseudo-rigid-body model, as discussed in Section 1.3 *Motivation for the Research.*

3.3 Formulating the Lagrangian

Of particular interest in a dynamic analysis of the constant-force mechanism is its output force. Given an input slider displacement $x_b(t)$, the dynamic model should indicate the reaction force $F_b(t)$ at the slider, as shown in Figure 3.3. The independent coordinate $x_b(t)$ could be chosen as the generalized coordinate for Lagrange's equation and would result in a generalized force corresponding to $F_b(t)$. Instead $\theta_2(t)$ will be chosen as the generalized coordinate, corresponding to a generalized force $Q_{\theta_2}(t)$. Choosing θ_2 as the generalized coordinate simplifies much of the derivation. Note that because θ_2 is an angle, the generalized force Q_{θ_2} has units of moment; a relation to transform between Q_{θ_2} and F_b will be given at the end of the chapter.

The Lagrangian $\mathcal{L}$ is formed by taking the difference of the scalar quantities of kinetic energy T and potential energy V of the system,

$$\mathcal{L} = T - V \tag{3.5}$$

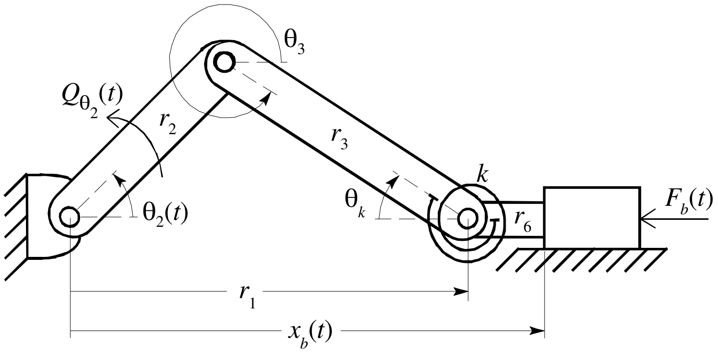

Figure 3.3 Reaction force $F_b(t)$ at the slider (output port); independent generalized coordinate $\theta_2(t)$ and generalized force $Q_{\theta_2}(t)$.

One way to formulate T is to separate the motion of the mechanism inertias into both translation and rotation, as illustrated in Figure 3.4. The center of mass of each link translates along a predefined path as the mechanism moves, and each link rotates about its center of mass. The mass of link 6 can be lumped together with the mass of the slider since both travel along a linear path and neither rotates:

$$m_s = m_6 + m_{slider} \tag{3.6}$$

The first three terms of the kinetic energy expression represent the translational energy of the system, and the last two represent the rotational energy:

$$T = \frac{1}{2}m_2 v_{c2}^{\ 2} + \frac{1}{2}m_3 v_{c3}^{\ 2} + \frac{1}{2}m_s \dot{r}_1^{\ 2} + \frac{1}{2}J_{c2}\dot{\theta}_2^{\ 2} + \frac{1}{2}J_{c3}\dot{\theta}_3^{\ 2} \tag{3.7}$$

where m_i is the mass, v_{ci} is the velocity of the center of mass, J_{ci} is the mass moment of inertia, and $\dot{\theta}_i$ is the angular velocity of links 2 and 3; $\dot{r}_1$ is the velocity of the slider.

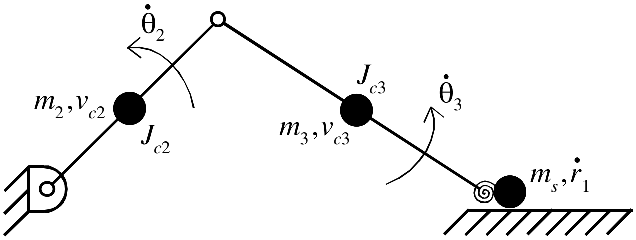

Figure 3.4 Translational and rotational motion of the mechanism links.

The mass moments of inertia of links 2 and 3 are

$$J_{ci} = \frac{1}{12} m_i r_i^2 \tag{3.8}$$

Assuming the mechanism lies in a plane perpendicular to gravity, the potential energy of the system is simply the torsional spring energy

$$V = \frac{1}{2} k \theta_k^2 \tag{3.9}$$

The Lagrangian $\mathscr{L} = T - V$ must be expressed in terms of the generalized coordinate θ_2 and its time derivative $\dot{\theta}_2$ before forming Lagrange's equation. The following equations recast the variables in T and V in terms of θ_2 and $\dot{\theta}_2$:

$$v_{c2}^2 = \frac{1}{4} r_2^2 \dot{\theta}_2^2 \tag{3.10}$$

$$v_{c3}^2 = r_2^2 \dot{\theta}_2^2 + \frac{1}{4} r_3^2 \dot{\theta}_3^2 + r_2 r_3 \cos(\theta_2 - \theta_3) \dot{\theta}_2 \dot{\theta}_3 \tag{3.11}$$

$$\dot{r}_1^2 = [r_2 \sin\theta_2 \dot{\theta}_2 + r_3 \sin\theta_3 \dot{\theta}_3]^2 \tag{3.12}$$

$$\theta_k = \operatorname{asin}\left(\frac{r_2}{r_3} \sin\theta_2\right) \tag{3.13}$$

$$\theta_3 = \operatorname{asin}\left(-\frac{r_2}{r_3}\sin\theta_2\right) \tag{3.14}$$

$$\dot{\theta}_3 = -\frac{r_2\cos\theta_2}{\sqrt{r_3^2 - r_2^2\sin^2\theta_2}}\dot{\theta}_2 \tag{3.15}$$

It is also useful to give x_b as a function of θ_2:

$$x_b = r_1 + r_6 \tag{3.16}$$

where

$$r_1 = r_2\cos\theta_2 + \sqrt{r_3^2 - r_2^2\sin^2\theta_2} \tag{3.17}$$

3.4 Lagrange’s Equation

Using Lagrange’s formulation, the equation of motion for the system is expressed as

$$\frac{d}{dt}\left(\frac{\partial\mathcal{L}}{\partial\dot{\theta}_2}\right) - \frac{\partial\mathcal{L}}{\partial\theta_2} = Q_{\theta_2} \tag{3.18}$$

The left side of the equation is a statement of the principle of conservation of energy, and the right side represents the non-conservative generalized force (Thomson and Dahleh, 1998).

When the derivatives of the Lagrangian are expanded out, the equation of motion for the system becomes

$$\begin{aligned}
&\left[m_3\left(\frac{1}{2}\frac{r_2^{\,5}\sin^3\theta_2\cos^2\theta_2}{\xi^{3/2}}+\frac{1}{3}\frac{r_2^{\,4}r_3^{\,2}\sin\theta_2\cos^3\theta_2}{\xi^2}-\frac{1}{2}\frac{r_2^{\,3}\sin^3\theta_2}{\sqrt{\xi}}\right.\right.\\
&\left.+\frac{r_2^{\,3}\sin\theta_2\cos^2\theta_2}{\sqrt{\xi}}-\frac{1}{3}\frac{r_2^{\,2}r_3^{\,2}\sin\theta_2\cos\theta_2}{\xi}+r_2^{\,2}\sin\theta_2\cos\theta_2\right)\\
&+m_s\left(\frac{r_2^{\,6}\sin^3\theta_2\cos^3\theta_2}{\xi^2}+\frac{r_2^{\,5}\sin^3\theta_2\cos^2\theta_2}{\xi^{3/2}}-\frac{r_2^{\,4}\sin^3\theta_2\cos\theta_2}{\xi}\right.\\
&\left.\left.+\frac{r_2^{\,4}\sin\theta_2\cos^3\theta_2}{\xi}+2\frac{r_2^{\,3}\sin\theta_2\cos^2\theta_2}{\sqrt{\xi}}-\frac{r_2^{\,3}\sin^3\theta_2}{\sqrt{\xi}}+r_2^{\,2}\sin\theta_2\cos\theta_2\right)\right]\dot{\theta}_2^{\,2} \qquad \textbf{(3.19)}\\
&+\left[m_2\left(\frac{1}{3}r_2^{\,2}\right)+m_3\left(\frac{r_2^{\,3}\sin^2\theta_2\cos\theta_2}{\sqrt{\xi}}+\frac{1}{3}\frac{r_2^{\,2}r_3^{\,2}\cos^2\theta_2}{\xi}+r_2^{\,2}-r_2^{\,2}\cos^2\theta_2\right)\right.\\
&\left.+m_s\left(\frac{r_2^{\,4}\sin^2\theta_2\cos^2\theta_2}{\xi}+2\frac{r_2^{\,3}\sin^2\theta_2\cos\theta_2}{\sqrt{\xi}}+r_2^{\,2}\sin^2\theta_2\right)\right]\ddot{\theta}_2\\
&+\frac{k\,\mathrm{asin}\left(\frac{r_2}{r_3}\sin\theta_2\right)r_2\cos\theta_2}{\sqrt{\xi}} = Q_{\theta_2}
\end{aligned}$$

where

$$\xi = r_3^{\,2}-r_2^{\,2}\sin^2\theta_2 \qquad \textbf{(3.20)}$$

The generalized force Q_{θ_2} consists of a moment due directly to the force F_b acting on the slider τ_{F_b}, a torque due to Coulomb pin friction τ_C, and a term to compensate for unmodeled torque in the mechanism τ_{um}:

$$Q_{\theta_2} = \tau_{F_b}+\tau_C+\tau_{um} \qquad \textbf{(3.21)}$$

Addition of the static terms τ_C and τ_{um} to the dynamic model is discussed at length in Section 3.6 *More on Coulomb Friction and Unmodeled Torque* on page 27.

Though more elaborate expressions for the Coulomb friction term τ_C are possible, the following simple relation gives sound results:

$$\tau_C = C\theta_2 \operatorname{sgn}(\dot{\theta}_2) \tag{3.22}$$

Multiplying by θ_2 is a departure from classical Coulomb friction formulation, but it gives better results, and is based on the idea that the classical Coulomb friction coefficient is likely to be proportional to the angle θ_2.

The values of the Coulomb friction coefficient C and the unmodeled torque τ_{um} are chosen using experimental data from static tests, as described in the next section.

Finally, to transform from the torque τ_{F_b} to the mechanism's output force F_b, use the expression

$$F_b = \tau_{F_b} \Big/ \frac{\partial x_b}{\partial \theta_2} \tag{3.23}$$

where

$$\frac{\partial x_b}{\partial \theta_2} = -r_2 \sin\theta_2 - \frac{{r_2}^2 \sin\theta_2 \cos\theta_2}{\sqrt{\xi}} \tag{3.24}$$

Equations (3.19) - (3.24) represent the closed-form dynamic model of compliant constant-force mechanism, configuration Class 1A-d. Note that the equation of motion is derived from the pseudo-rigid-body model of the mechanism, rather than the actual compliant mechanism.

3.5 Determining Coulomb Friction and Unmodeled Torque

The Coulomb friction coefficient C and the unmodeled torque τ_{um} for the dynamic model must be chosen using empirical data from a static test of an actual constant-force mechanism. Values for C and τ_{um} are now determined for the constant-force mechanism described in the next chapter. For more detail concerning the test mechanism and how static data was gathered, see Section 4.1 *Constant-Force Test Mechanism* on page 33 and Section 4.3 *Dynamic and Static Testing* on page 39.

Figure 3.5 shows the results of a static test. The modeled force with $\tau_C = \tau_{um} = 0$ is calculated directly from the input position x_b, a gradual ramp first in compression then expansion. The dynamic model equations (3.19) - (3.24) are used to calculate the predicted force, with mechanism parameters as defined in Chapter 4.

Clearly, without consideration for the static terms τ_C and τ_{um}, the modeled force does not correlate well with the measured force. To correct this, values for C and τ_{um} which draw the predicted force into better agreement with the measured force can be chosen empirically by performing a least-squares fit. Figure 3.6 illustrates this, with $C = 0.045\ N \cdot m\ (0.40\ in \cdot lb_f)$ and $\tau_{um} = -0.228\ N \cdot m\ (-2.01\ in \cdot lb_f)$, resulting in a nice match between modeled and measured force.

3.6 More on Coulomb Friction and Unmodeled Torque

The underlying assumption made by including Coulomb pin friction τ_C and unmodeled torque τ_{um} terms in the model is that most of the mechanism's

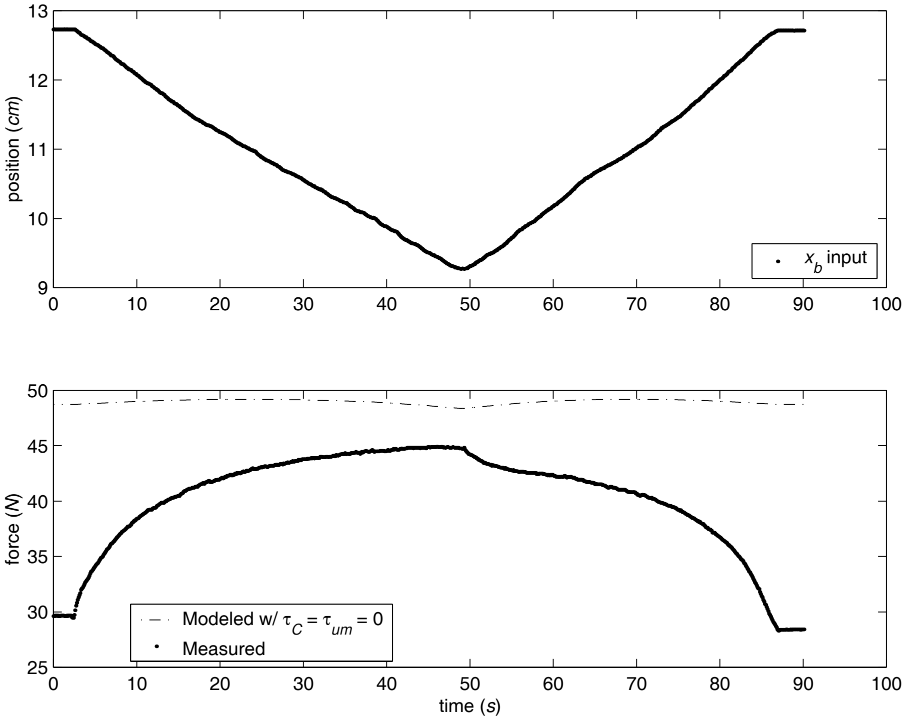

Figure 3.5 Modeled and measured force for static test input x_b; modeled force calculated with $\tau_C = \tau_{um} = 0$.

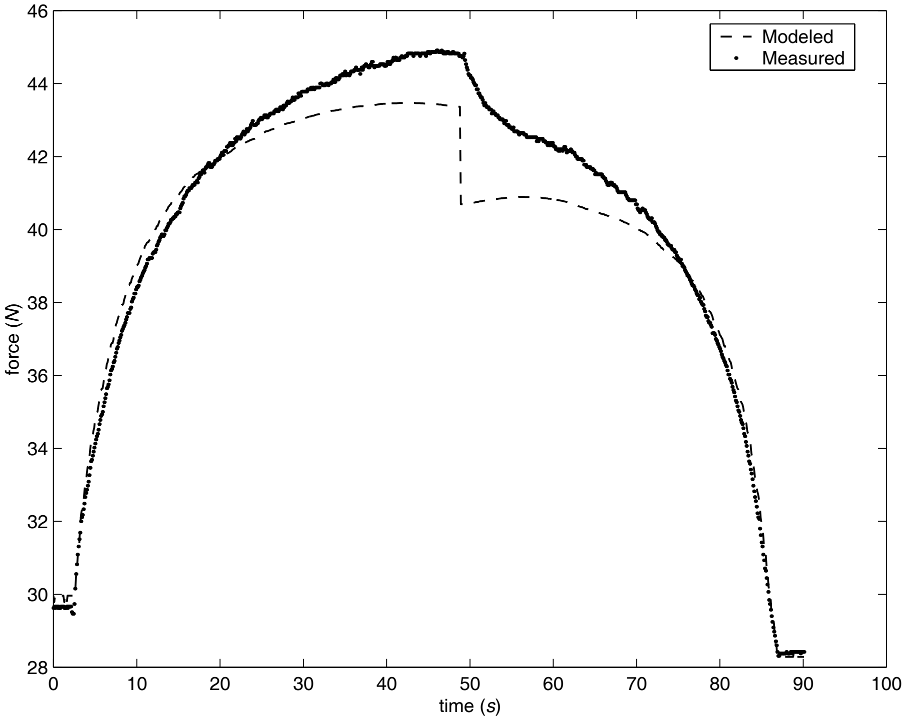

Figure 3.6 Modeled and measured force for static test input x_b; modeled force calculated with $C = 0.045\ N \cdot m$ and $\tau_{um} = -0.228\ N \cdot m$.

difficult-to-model characteristics can be represented by one or the other. Note that both τ_C and τ_{um} do not relate to the dynamic terms of the model directly – they are static terms whose effects have already been observed (refer again to Figure 2.2).

The physical mechanism built to validate the model possesses these somewhat elusive properties in basically two locations: (1) the mechanism's pin joints, and (2) the mechanism's links/segments. Associated with the pin joints are Coulomb friction in the pins, possible binding of the pins due to misalignment, unmodeled tolerances in the pin joints, and the effect of heating of the pins as they rotate (i.e. perhaps the steady-state assumed when acquiring data at each frequency isn't actually steady-state when one considers thermal effects). Associated with the mechanism's links/segments is possible flexing of the rigid link (it's only twice as thick as the flexible segment), and the fact that the compliant segment cannot flex where the hinge rivets to it, as assumed by the pseudo-rigid-body model rule for a cantilever beam with a force at the free end. Friction and perhaps binding are taken care of by the τ_C term; the other effects are taken up by the τ_{um} term.

Viscous damping in the system is assumed to be negligible. Also, no signs of stress relaxation or plastic deformation of the flexible segment (made of spring steel) could be detected.

The fact that τ_C and τ_{um} have such a large effect on the model, at least at the static end of the frequency spectrum, should be addressed. Three suggestions are offered: (1) it is not unreasonable to expect that each of the effects listed in the proceeding paragraph, taken as a whole, could have a sizable impact, (2) the formulation of τ_C and τ_{um}, and where they are placed in the model holds true to the physical system; their inclusion is substantiated by the fact that empirically altering only two coefficients enhances rather than detracts from the model, and (3) two other static models predict ranges of force similar to that predicted by the dynamic model of this chapter taken at zero frequency, with $\tau_C = \tau_{um} = 0$; this supports the dynamic model since both static models neglect friction and unmodeled torque effects.

To elaborate more on point (3), both existing constant-force mechanism theory and a finite-element model of the compliant constant-force mechanism are frictionless, ideal static models which, given an input displacement, return the force expected at the mechanism's output port. Compared with predictions from these two sources, the dynamic model with $\tau_C = \tau_{um} = 0$ predicts close to the same range of forces over a given mechanism displacement.

Figure 3.7 shows the force predicted by the static portion of the dynamic model (i.e., with velocities and accelerations set to zero), with $\tau_C = \tau_{um} = 0$. The x-axis is divided into equally spaced positions across the mechanism's full range of deflection. Next on the plot is the force predicted by existing constant-force mechanism theory, essentially an application of the principle of virtual work on the pseudo-rigid-body model of the mechanism:

$$F_{vw} = \frac{K\cos\theta_2(2\pi - \theta_3)}{r_3\sin(\theta_2 - \theta_3)} \tag{3.25}$$

Both plots match perfectly, as they should; both are mathematical models of the same rigid-body mechanism with discretized compliance. A comparison of the two is shown here as confirmation that the static portion of the dynamic model is correct.

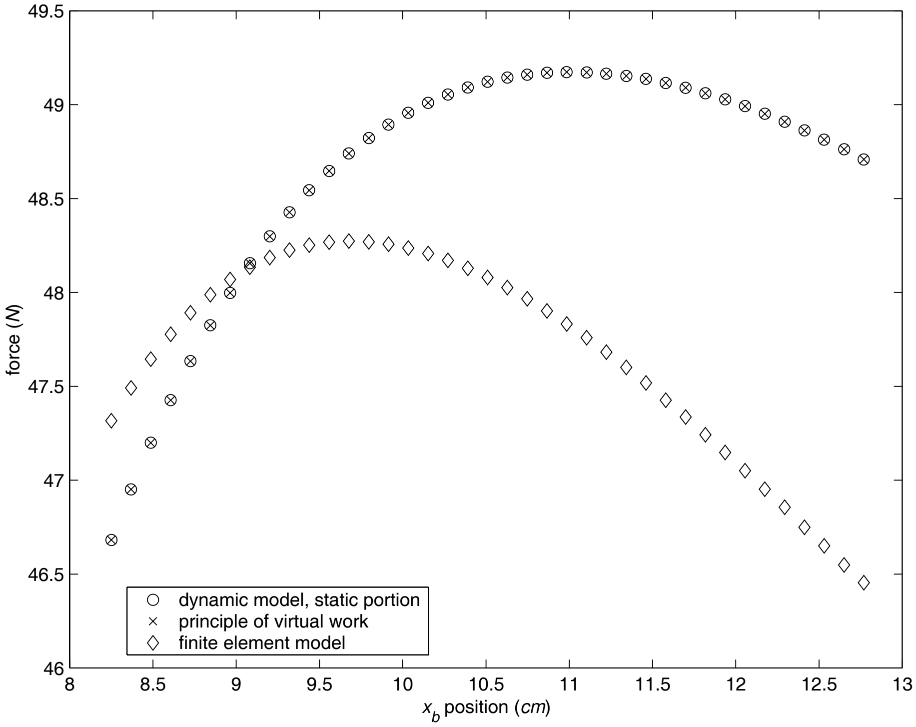

Figure 3.7 Force predicted by the static terms of the dynamic model, by the principle of virtual work (both based on pseudo-rigid-body model of mechanism), and by a finite-element model of the mechanism (based on the compliant mechanism itself).

The third plot deserves the most attention. It shows the results of a force vs. position simulation of the mechanism using a commercial finite-element code capable of non-linear analysis (ANSYS®). The finite-element model is valuable because it models not the pseudo-rigid-body model of the mechanism, but the mechanism with rigid and flexible segments. The model assumes an ideal mechanism with no friction. (See APPENDIX D for the ANSYS® script.) A comparison of the magnitude of the finite-element model force with the dynamic model prediction (with $\tau_C = \tau_{um} = 0$) shows good agreement, considering the small force scale used for the y-axis of the plot. It is reasonable to conclude that any difference in the finite-element model is due to the fact that the dynamic model and the virtual work model disregard the mechanism's distributed compliance, while the finite-element model does not.

The results of Figure 3.7 argue that the large disagreement between measured and modeled force with $\tau_C = \tau_{um} = 0$ (Figure 3.5) must be attributed to something other than flagrant assumptions made by the pseudo-rigid-body model. The agreement between the three static models not only argues the validity of including τ_C and τ_{um} in the model, but it authenticates the dynamic model at zero frequency.

CHAPTER 4 Experimental Setup

To test the validity of the dynamic model of Chapter 3, a constant-force test mechanism was constructed. Though many constant-force mechanisms had previously been fabricated, this was the first to be tested dynamically. The mechanism design and experimental setup for instrumenting and testing the device is presented here.

4.1 Constant-Force Test Mechanism

Figure 4.1 shows a picture of the constant-force mechanism used to test the dynamic model derived in the previous chapter. It consists of a pair of configuration Class 1A-d constant-force mechanisms mounted to the same ground and sharing the same slider. Mounting two mechanisms opposite each other is useful because each cancels the moment induced by the other, and the issue of friction between slider and ground is eliminated.

To apply the dynamic model to the pair of constant-force springs, simply imagine the device split down its line of symmetry, as in Figure 4.2. The parameters of one of the

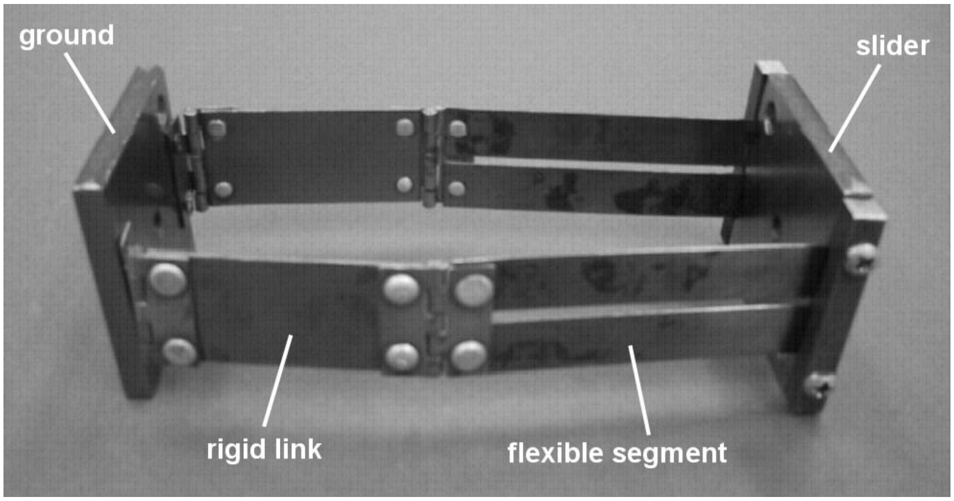

Figure 4.1 Constant-force mechanism for dynamic testing.

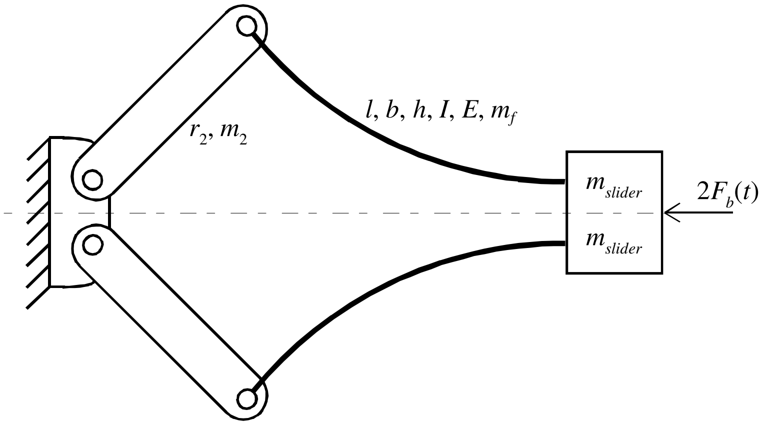

Figure 4.2 Constant-force test mechanism divided along its line of symmetry.

halves (i.e. link lengths, masses, etc.) are used in the dynamic model equations (3.19) - (3.24) to solve for the predicted force $F_b(t)$ of a single mechanism. The force expected at the output port of the constant-force spring pair is then twice $F_b(t)$. Note that the value of m_{slider} is half the mass of the shared slider, not its entire mass.

Each rigid link of the test mechanism is made of 1.19 *mm* (.047 *in*) -thick steel sheet metal, and each flexible segment is made of two strips of 0.64 *mm* (0.025 *in*) -thick steel shim stock. Utility hinges serve as pins between ground and each rigid link, and between each rigid link and flexible segment. Both ground pins mount to a steel ground plate, and both flexible segments clamp to the shared slider, another steel plate.

The relevant dimensions, masses (incorporating the masses of the hinges and clamps), and properties of the test mechanism are listed in Table 4.1. Parameters used directly in the dynamic model equations of Chapter 3 are emphasized. The variables *b*, *h*, and *I* are the width, thickness, and area moment of inertia of the flexible segment's cross section; E and m_f are the modulus of elasticity and mass of the flexible segment. All other variables are as defined in Chapter 3.

The test mechanism was designed to exhibit constant-force for a maximum of 40% deflection, or a deflection of $\Delta x_b = 0.40(r_2 + r_3)$, or 4.757 *cm* (1.873 *in*). The mechanism's total extended length is $r_2 + l$, or 13.007 *cm* (5.112 *in*).

The device's nominal constant-force F_{nom} (doubled for the mechanism pair), as derived in Howell (2001) is

$$F_{nom} = 2\frac{k}{r_3}\Phi = 50.19\ N \quad (11.29\ lb_f) \tag{4.1}$$

The average nondimensionalized constant-force Φ for a 40% deflection Class 1A constant-force mechanism, tabulated in Millar et al. (1996), is $\Phi = 0.4773$.

4.2 Experimental Setup

Figure 4.3 (a) shows a photograph of the experimental setup used to validate the constant-force mechanism dynamic model. The setup was designed to allow testing of the mechanism by sinusoidally cycling it (through compression and expansion) at different

TABLE 4.1 Test mechanism dimensions, material properties, and masses (parameters used directly in dynamic model equations of Chapter 3 are emphasized).

Parameter	**Value**
$\boxed{r_2}$	$5.490\ cm\ \ (2.162\ in)$
l	$7.517\ cm\ \ (2.960\ in)$
$\boxed{r_3 = \gamma l}$	$6.390\ cm\ \ (2.516\ in)$
$r_6 = l - r_3$	$1.128\ cm\ \ (0.444\ in)$
b	$2.540\ cm\ \ (1.000\ in)$
h	$0.064\ cm\ \ (0.025\ in)$
$I = \frac{1}{12}bh^3$	$5.420 \times 10^{-13}\ m^4\ \ (1.302 \times 10^{-6}\ in^4)$
E	$206.8\ GPa\ \ (30 \times 10^6\ psi)$
$\boxed{m_2}$	$13.8\ g\ \ (0.0304\ lb_m)$
m_f	$10.7\ g\ \ (0.0235\ lb_m)$
$\boxed{m_3 = \gamma m_f}$	$9.1\ g\ \ (0.0200\ lb_m)$
$m_6 = m_f - m_3$	$1.6\ g\ \ (0.0035\ lb_m)$
m_{slider}	$84.7\ g\ \ (0.1868\ lb_m)$
$\boxed{m_s = m_{slider} + m_6}$	$86.3\ g\ \ (0.1903\ lb_m)$
$\boxed{k}$	$3.359\ N \cdot m\ \ (29.73\ in \cdot lb_f)$
$\boxed{C}$	$0.055\ N \cdot m\ \ (0.49\ in \cdot lb_f)$
$\boxed{\tau_{um}}$	$-0.235\ N \cdot m\ \ (-2.08\ in \cdot lb_f)$

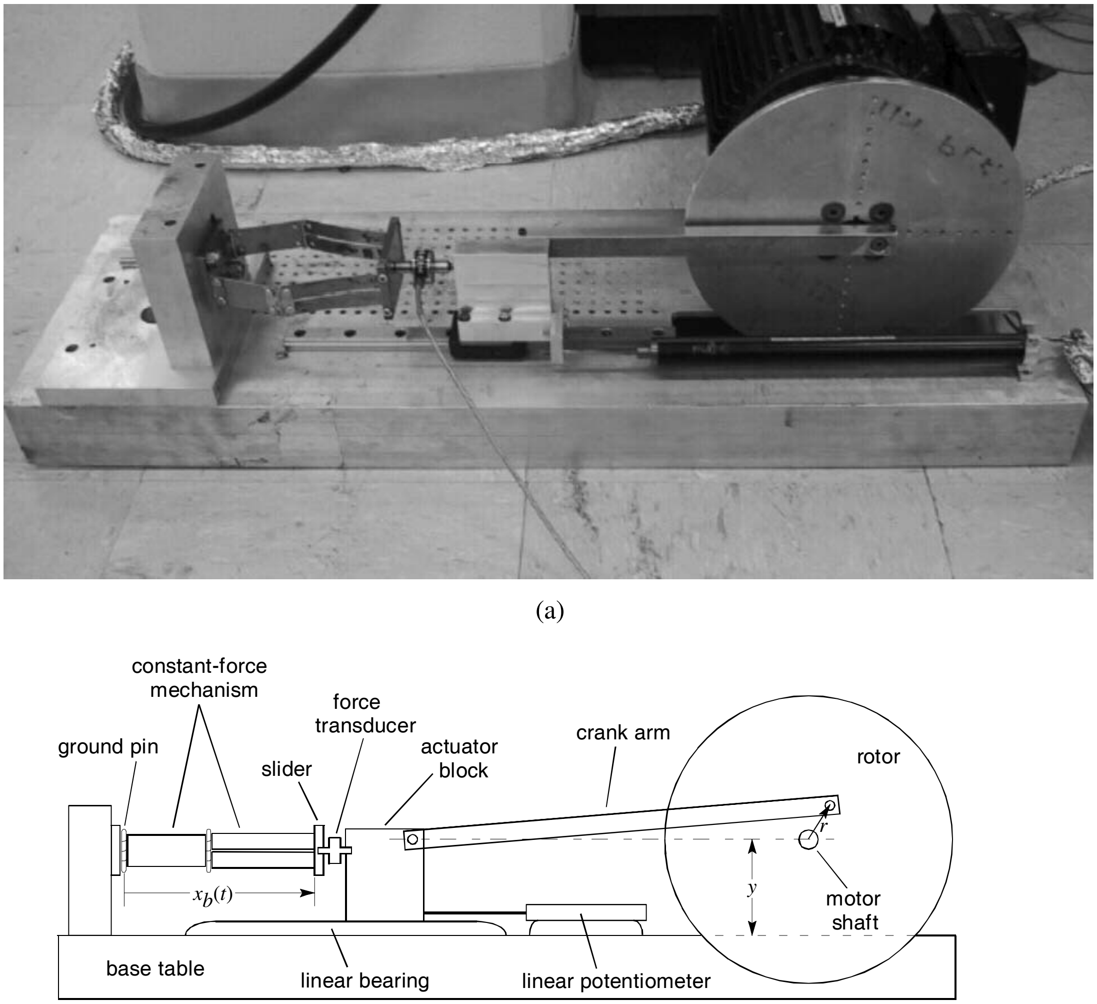

(a)

(b)

Figure 4.3 (a) Photograph of experimental setup for dynamic testing of constant-force mechanisms, and (b) schematic of experimental setup.

frequencies. Comparing the force data obtained from these tests with the force predicted by the dynamic model will authenticate or invalidate the model. The experimental setup is described here.

The constant-force test mechanism detailed in the proceeding section bolts to a thick aluminum ground, mounted perpendicular to a large aluminum table. In this manner both ground pins of the test mechanism are fixed with respect to the table.

The test mechanism slider is actuated by a small aluminum block free to move across a linear bearing. Driving the actuator block is a velocity-controlled 2-hp motor with a rotor and crank-arm. The center of the motor shaft and the point of attachment of the crank-arm to the actuator block share the same height *y* from base table, as depicted in Figure 4.3 (b). As such, assuming constant angular velocity of the motor and a small crank radius *r*, the actuator block drives the mechanism with an approximately sinusoidal velocity.

The rotor is drilled with a series of tapped holes, each located at a different radius, for variable positioning of the crank arm. This allows for larger or smaller total linear displacements of the mechanism as the rotor cycles.

Bolted in-line between the actuator block and test mechanism, a load cell measures force exerted on the slider. Half of the mass of the load cell is lumped with the test mechanism's slider. The instrument used is an A. L. Design 50-*lb*-capacity strain-gauge force transducer model ALD-MINI-UTC-F, with a nonlinearity of $\pm 0.14\,\%$ of full-scale, or resolution error of $\pm 0.311\ N\ (\pm 0.07\ lb_f)$. Force measurement errors due to unwanted torque from the load cell's placement between the actuator block and slider were found to be less than $0.311\ N$, and so deemed to be negligible.

A linear potentiometer measures mechanism deflection. The potentiometer housing is mounted to the base table, with its positioning rod attached to the actuator block. Since the actuator block, load cell, and slider are bolted together, the potentiometer measures the position $x_b(t)$, a measurement of the point where mechanism meets the slider, located with respect to where the mechanism attaches to ground. This is the same definition of x_b given in the previous chapter. The potentiometer used is a 10 kΩ Midori Precisions LP-250 GreenPot. Measurement error of the position instrumentation was found to be $\pm 0.071\ cm\ (\pm 0.028\ in)$.

Both force and position data were acquired through a computer equipped with a National Instruments PCI E Series DAQ.

This setup allows for the testing of the constant-force mechanism prototype over a range of frequencies, up to about 85 *rad/s* (13.5 *Hz*), above which there is danger of harming the setup equipment and/or the mechanism.

4.3 Dynamic and Static Testing

Both dynamic and static tests can be performed using the experimental setup described above. Dynamic tests are performed by setting the motor controller to run at a constant velocity, waiting for the system to reach steady-state, then collecting data at a sampling rate well above the input sinusoid frequency. The position of the mechanism mount is adjusted so that at maximum expansion the mechanism has a preload.

Static tests are performed by removing the crank arm from the setup and again preloading the mechanism, this time using a long bar clamp. The clamp is slowly screwed tight compressing the mechanism, and then unscrewed allowing it to expand back to its initial position.

Depending on whether the test is dynamic or static, the data is processed differently.

4.3.1 DYNAMIC DATA PROCESSING

Unlike a static test, a dynamic test must be performed with the motor running, which introduces a sizable amount of electrical interference. To eliminate electrical noise from the data, both position and force signals are low-pass filtered through an 8th-order Butterworth filter with a cutoff frequency of 314 *rad/s* (50 *Hz*).

As previously explained, for every dynamic test the input position $x_b(t)$ is always constrained to be a sinusoid. Of interest is the mechanism's force output during one cycle, from its expanded state through compression and back to expansion, at any frequency. To cancel measurement errors from cycle to cycle in a given data set and to condense the data for ease of viewing, 30 force cycles are averaged together.

4.3.2 STATIC DATA PROCESSING

Since a static test does not require the motor to be on, no filtering of electrical noise is necessary. Also, because a static test consists of only one cycle, no averaging is required. Position and force signals for static tests were both found to be clean, reliable, and free of noise, so the data was used as collected.

In every plot that displays measured force data (whether dynamic or static), spacing between plotted points is the time interval between samples.

For exact detail on force and position data processing, refer to the Matlab® source code held by the Utah Center of Excellence for Compliant Mechanisms at Brigham Young University.

CHAPTER 5 Empirical and Theoretical Findings

Given a position input $x_b(t)$, and all physical parameters correctly defined, the dynamic model of Chapter 3 predicts the force expected at the constant-force mechanism's output port. A side-by-side comparison of modeled vs. measured force from an actual mechanism shows that the model predicts the dynamic response of the test mechanism quite satisfactorily.

The following three sections present comparisons of the dynamic model and experimental results, and a more detailed look at the model. Section 5.1 lays out comparisons of the modeled and measured force of the mechanism, tested at different frequencies. Section 5.2 presents an unexpected dynamic effect, a range of frequencies over which the mechanism manifests better constant-force behavior than it does statically. And Section 5.3 evaluates the dynamic model as an abstraction of the physical system.

5.1 Modeled vs. Measured Force

Figures 5.1 to 5.3 show position and force plots of three dynamic tests of increasing frequency, ω. For each figure, the predicted force cycle is calculated directly from the

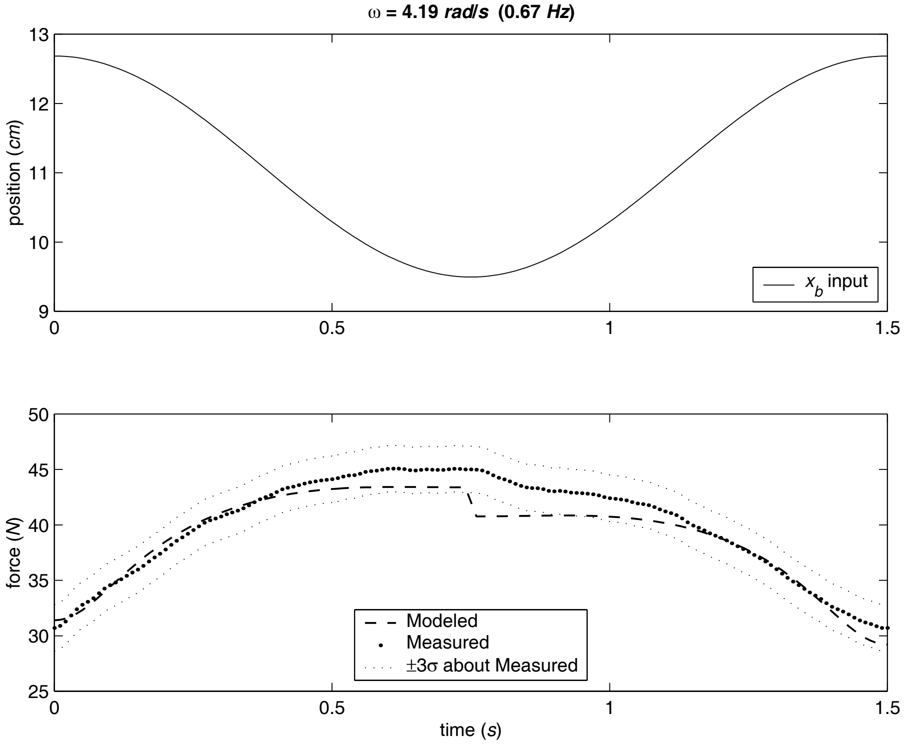

Figure 5.1 Predicted and measured force for sinusoidal input x_b of $\omega = 4$ *rad/s*.

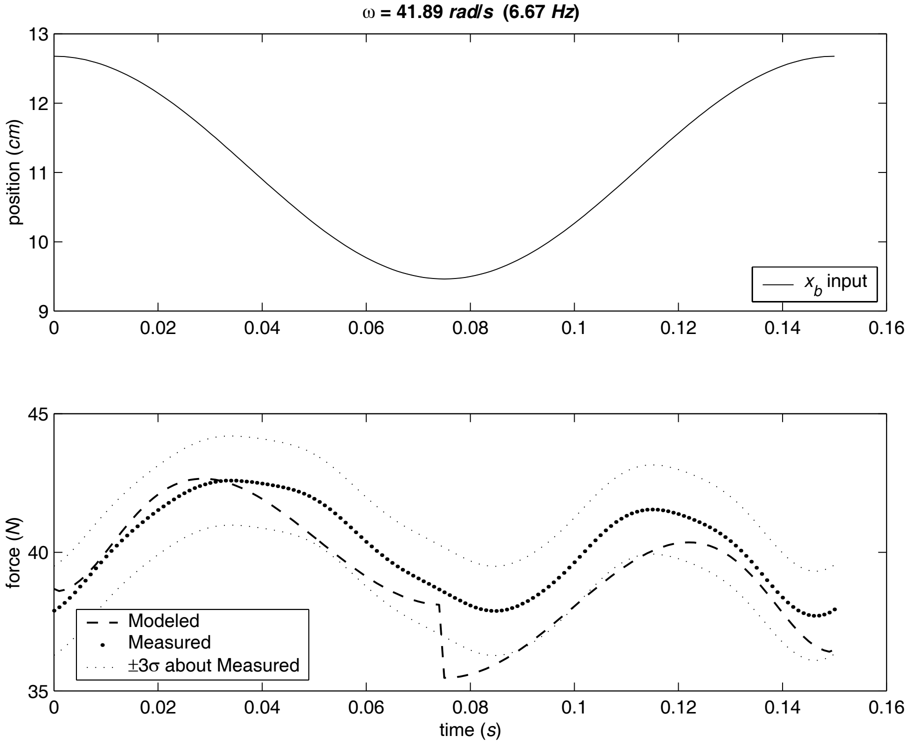

Figure 5.2 Predicted and measured force for sinusoidal input x_b of $\omega = 42$ *rad/s*.

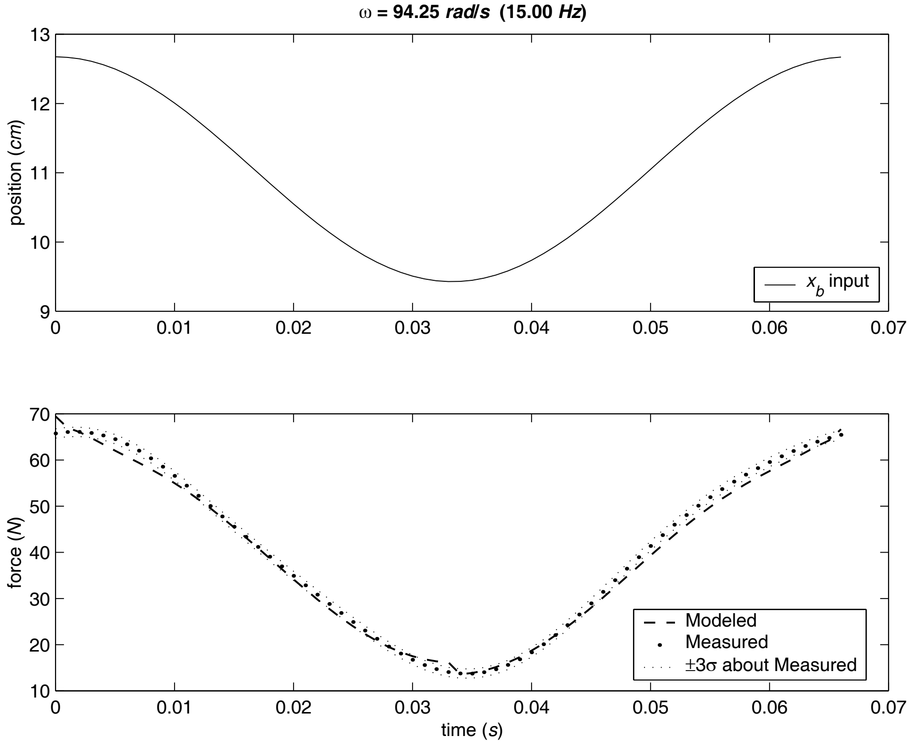

Figure 5.3 Predicted and measured force for sinusoidal input x_b of $\omega = 94$ *rad/s*.

input sinusoid cycle x_b shown in the position plot, using the dynamic model equations (3.19) - (3.24). The measured force cycle in each figure is the result of force data processed as described in Section 4.3.1 *Dynamic Data Processing* on page 40. The measured data is banded by ±3 pooled sample standard deviations, or $\pm 3\,\sigma$, representing the 99.74% confidence interval of the measurement.

While the modeled force does not match the measured force point for point, it does predict the average force, the peak-to-peak force difference, and the general shape of the force profile at any given frequency. These are important and useful elements to gather from a dynamic analysis of the system.

5.2 Dynamic Characterization of the Model

Although nonlinearities make it impossible to express an exact algebraic transfer function for the system, and no simple magnitude and phase plot can be shown, two useful plots can be analyzed. The median force and peak-to-peak force magnitude difference of the dynamic model as functions of frequency are shown in Figure 5.4. Each frequency assumes a sinusoidal position input with amplitude equal to the full 40% designed mechanism deflection (with a slight "pre-displacement" to give a preload at full expansion). For good plot resolution, the dynamic model response is calculated at 400 separate and equally spaced frequencies.

The heavy solid line represents the force predicted by the dynamic model with all parameters as defined in Table 4.1. The next two lines are purely theoretical; what happens when the mass of the slider is set to zero, or the mechanism has no inertia at all (all masses set to zero). Setting all the inertias to zero provides a baseline useful for comparison of the other curves, and setting the end mass to zero shows the dynamic response of the constant-force spring isolated as a separate "module". The fourth and fifth lines in the figure show the effect of multiplying the rigid link mass by four (which represents a possible improvement to the test mechanism, thickening the rigid link to ensure it doesn't flex), and the effect of reducing the end mass by 75%. Lastly, the modeled force with Coulomb friction τ_C and unmodeled torque τ_{um} set to zero is given.

Notice that each curve in the peak-to-peak force plot first curves down, then sustains a linear range before it starts to increase (all except for the third curve and last curve). This dip in magnitude difference is demonstrated nicely by Figures 5.1 to 5.3. Clearly, the

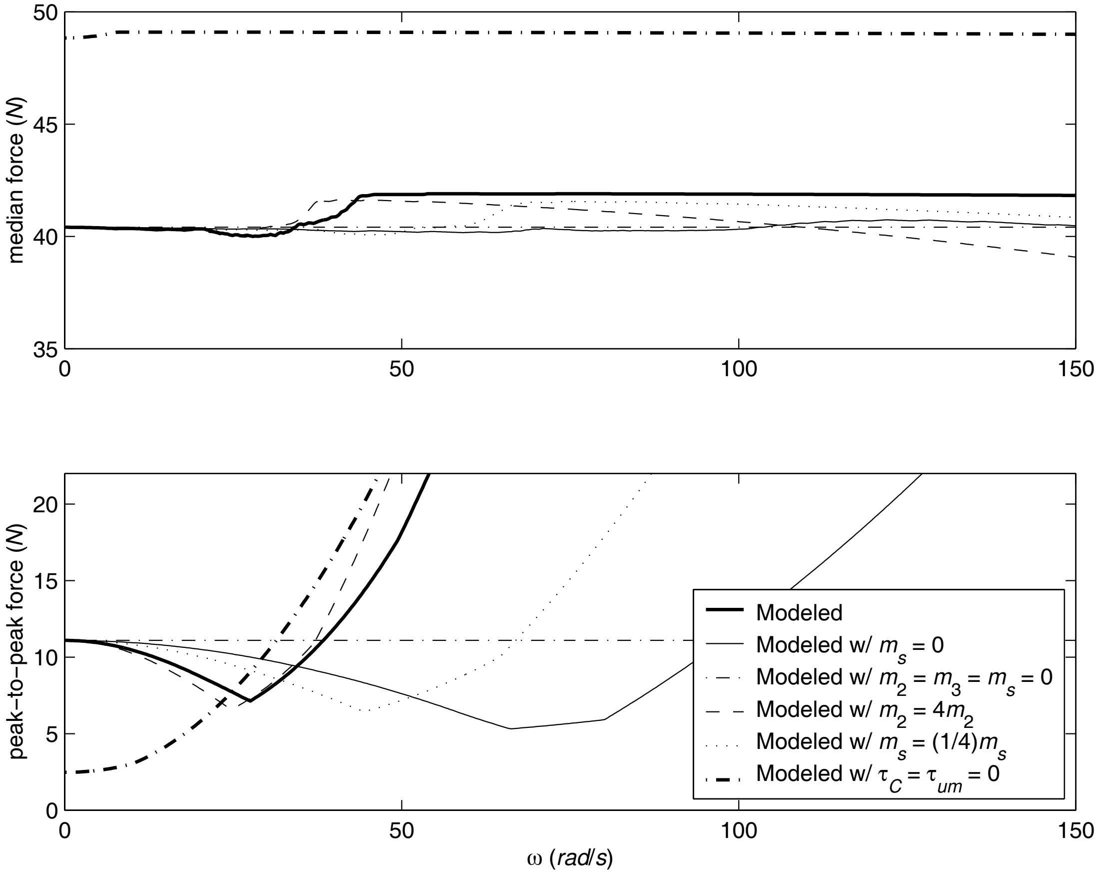

Figure 5.4 Frequency plots depicting the median force and peak-to-peak magnitude difference exhibited by the constant-force mechanism.

force profile of Figure 5.2 at $\omega = 42$ *rad/s* has a lower peak-to-peak force difference than the proceeding and following figures at $\omega = 4$ *rad/s* and $\omega = 94$ *rad/s*.

This very interesting and unexpected discovery of the peak-to-peak force plot is that there exists a range of frequencies over which a constant-force mechanism exhibits better constant-force behavior than at static levels. This range of frequencies coincides with the initial magnitude difference drop and most of the linear portion for each of the cases plotted in Figure 5.4. This unexpected finding significantly improves the likelihood that the compliant constant-force mechanism could be viable in industry.

For instance, if a designer were to use the test mechanism of Chapter 4 in an application and wanted to output as close to constant-force as possible, he or she would run the mechanism at a frequency of 30 *rad/s* (see the heavy solid line of Figure 5.4). This would result in a constant-force mechanism with a median force of 40 N (9.0 lb_f) and a force variance of ±3.5 N (±0.79 lb_f), much better than the ±6 N (±1.35 lb_f) force variance the device demonstrates statically.

Or if a designer wanted to maximize the range of frequencies over which the mechanism exhibits "better-than-static" constant-force, he or she could minimize the slider mass as much as possible. Figure 5.4 shows that the smaller the inertia of the slider, the higher the frequency before the force magnitude difference starts to rise.

Depending on what attributes are most desirable – a wide frequency band with moderately low peak-to-peak force, a single frequency with very low peak-to-peak force, or some other similar effect – the constant-force mechanism parameters can be optimized to achieve the desired results.

It was thought that this better-than-static constant-force phenomenon was caused in part by inclusion of τ_C and τ_{um} in the dynamic model, and the last curve of Figure 5.4 indicates as much. The peak-to-peak force difference of the dynamic model with τ_C and τ_{um} set to zero does not manifest a dip over the initial range of frequencies, as do the other curves. Instead, it curves up sharply. However, the phenomenon is not strictly due to τ_C and τ_{um} only, as evidenced by the third curve of Figure 5.4. This curve, which represents the dynamic model with all of the inertias set to zero, does include τ_C and τ_{um}, and it exhibits no dip in peak-to-peak force. So, the phenomenon is likely due to some combination of inertial effects and the effects modeled by τ_C and τ_{um} (as discussed in Section 3.6 *More on Coulomb Friction and Unmodeled Torque* on page 27). A linearization of the dynamic model about several operating points may hint at the physical reasons for this better-than-static constant-force effect, and may be a fruitful area for further research.

Frequency plots like the one in Figure 5.4 are given for four more compliant constant-force mechanisms tested in Chapter 7.

The peak-to-peak force and median force plots end at 150 *rad/s* for two reasons: (1) most everything of interest in the two plots occurs below this frequency, and (2) there is an upper limit (not necessarily 150 *rad/s*) above which the constant-force mechanism starts to yield a negative force (i.e., will start to pull instead of push). This occurs when the force cycle exceeds a frequency where the peak-to-peak force equals twice the median force. For the test device (heavy solid line), this occurs at about 99 *rad/s*.

In few applications will it be useful to give a constant-force mechanism a displacement input by attaching an actuator or surface directly to the slider; the two will usually be touching, but not rigidly connected. When the force becomes negative, this represents a situation where the slider breaks contact with the actuator or surface, possibly to cause an impact later. Of course these frequencies would be undesirable in most applications and should be avoided.

5.3 Evaluation of the Dynamic Model

How well does the dynamic model represent the constant-force mechanism? And, if the model anticipates the physical system well, can it be simplified, perhaps by omitting insignificant terms?

Both questions can be answered by analyzing how well the modeled force fits the measured force at each frequency tested. The modeled force is first compared to the measured force with the model untouched. Then various model parameters are set to zero to test their relative importance to the model. As a measure of goodness of fit, the error formula

$$E = \frac{\left|F_{modeled} - F_{measured}\right|}{F_{measured}} \tag{5.1}$$

where $F_{measured}$ is the average measured force, is applied to each data point in a force cycle and the average error $\bar{E}$ over the full force cycle is calculated. For better presentation, goodness of fit G_{fit} is cast as a percentage,

$$G_{fit} = 100(1 - \bar{E}) \tag{5.2}$$

Figure 5.5 shows how well the modeled force fits the measured force, for each test frequency. The first plot, represented by small circles, shows the goodness of fit of the dynamic model with all terms intact. The succeeding plots each eliminate one or two model parameters. Even with the complete model, the fit worsens as frequency increases. This is probably due to viscous damping, which was not modeled.

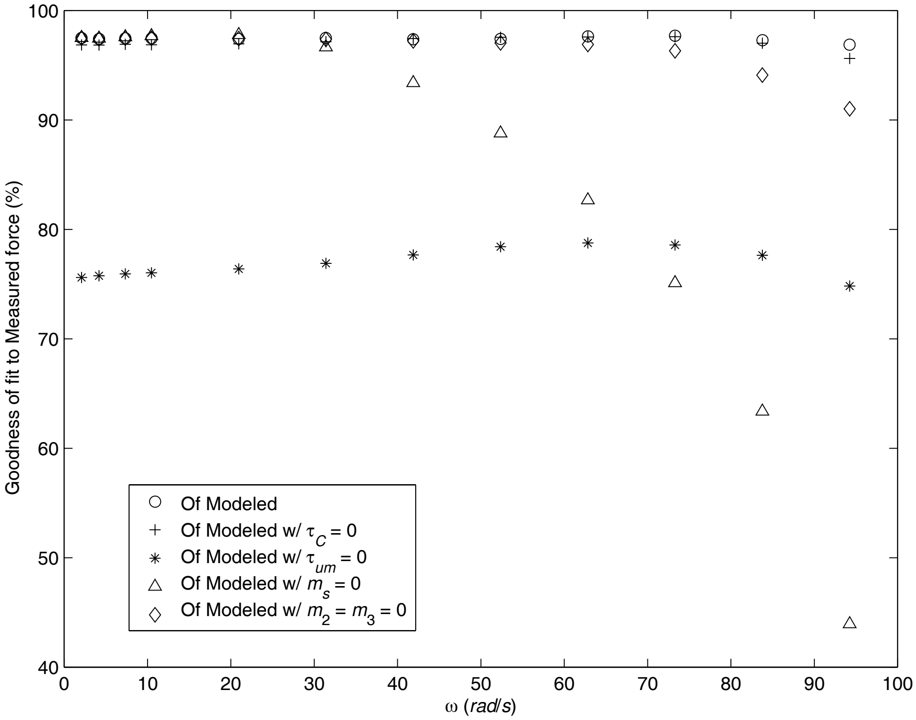

Figure 5.5 Goodness of fit of modeled force to measured force; goodness of fit of modeled force, minus various terms, to measured force.

Observe that the dynamic model represents the constant-force mechanism very well. Over the range of frequencies tested, the modeled force is within about 3% relative error of the measured force.

With the first question answered, the second question remains; can the omission of certain minor terms simplify the model? Not surprising is that the worst of these is the model with the end mass set to zero. The end mass possesses most of the system mass upon which inertial forces act. What is surprising is the result of omitting the unmodeled torque term τ_{um}. This is interesting compared to the effect of ignoring the Coulomb friction term τ_C. The contribution of τ_{um} in comparison to τ_C is more predominate than anticipated. Even so, the arguments put forth in Section 3.6 *More on Coulomb Friction and Unmodeled Torque* on page 27 account for this. Mark that inclusion of τ_{um} is crucial to the dynamic model.

Setting the link masses, m_2 and m_3, to zero represents a fair reduction in the equation of motion for the mechanism, equation (3.19). Doing this only sacrifices accuracy at higher frequencies (see Figure 5.5), so the dynamic model could be simplified by omitting the link inertias, but removing these terms does not point to a simpler model derivation. Figure 5.5 seems to be more useful in illustrating the relative importance of the dynamic model parameters, rather than as a tool to simplify the model.

5.4 Conclusions

The constant-force mechanism dynamic model, based on the pseudo-rigid-body model of the mechanism, proves to be a useful, viable abstraction of the physical system. The dynamic model of Chapter 3 approximates distributed compliance as a point compliance, while converting the device into a rigid-body mechanism; yet, a dynamic model of the simplified mechanism yields very satisfactory results. This further validates the usefulness of the pseudo-rigid-body model as a dynamics modeling tool, in conjunction with the research of Lyon et al. (1997).

Not only does the dynamic model effectively predict the output force of an actual constant-force mechanism, but it illuminates a very useful dynamic property of the mechanism: over certain frequencies it exhibits better constant-force behavior dynamically than statically. The knowledge of such a property makes the constant-force mechanism much more attractive for application in dynamic systems.

CHAPTER 6

Generalized Dynamic Model

The dynamic model for constant-force mechanism configuration Class 1A-d (the configuration selected for Chapter 3's derivation) can be generalized for all configurations of constant-force mechanism delineated in Midha et al. (1995), a subset of which are given in Figure 1.2. All that is required are some small changes to the pseudo-rigid-body model of configuration Class 1A-d. The velocity and acceleration terms of the corresponding dynamic model remain the same across all the configurations; only the static portion of the dynamic model changes.

6.1 Generalized Pseudo-Rigid-Body Model

Every constant-force mechanism presented in Figure 1.2 has essentially the same pseudo-rigid-body model. Using the pseudo-rigid-body model rule for small-length flexural pivots, and the rule for a cantilever beam with a force at the free end, each mechanism becomes a rigid-body slider mechanism. The most straight-forward alteration is every small-length flexural pivot becomes a pin and torsional spring combination, centered at the middle of the flexible segment. Only slightly more complex is every long flexible segment becomes two rigid segments joined by a pin and torsional spring. See APPENDIX A for a more a more precise treatment of these two rules. Forming the pseudo-rigid-body model of each configuration of constant-force mechanism is a straight-forward application of the method. Presented next are a pseudo-rigid-body model representative of all configurations, and three more examples of how to convert from compliant slider mechanism to rigid-body slider mechanism.

Figure 6.1 (b) shows the generalized pseudo-rigid-body model of the compliant constant-force mechanism, taken from Howell (2001). Every compliant constant-force mechanism conforming to the description given in (Midha et al., 1995) can be represented by this model, among them the example configuration of Figure 6.1 (a).

The generalized pseudo-rigid-body model of Figure 6.1 introduces some new variables. The torsional springs at each of the pin joints have spring constants of k_1, k_2, and k_3. Attending these are θ_{k_1}, θ_{k_2}, and θ_{k_3}, representing the angular deflection of each torsional spring. Based on the new notation, the torsional spring constant k and the angular deflection θ_k of Chapter 3 would be replaced by k_3 and θ_{k_3}. Depending on the choice of constant-force mechanism, one or two (not three) torsional springs may have a value of zero. The equivalent torsional spring constant k_i for a long flexible segment (cantilever beam with a force at the free end) is given by equation (3.3), and k_i for a small-length flexural pivot is given in APPENDIX A.

Notice that Figure 6.1 intentionally omits labeling the familiar variable x_b, a measurement of the point where the mechanism attaches to the slider, located with respect to where the mechanism connects to ground. This is done to preserve generality; in the case

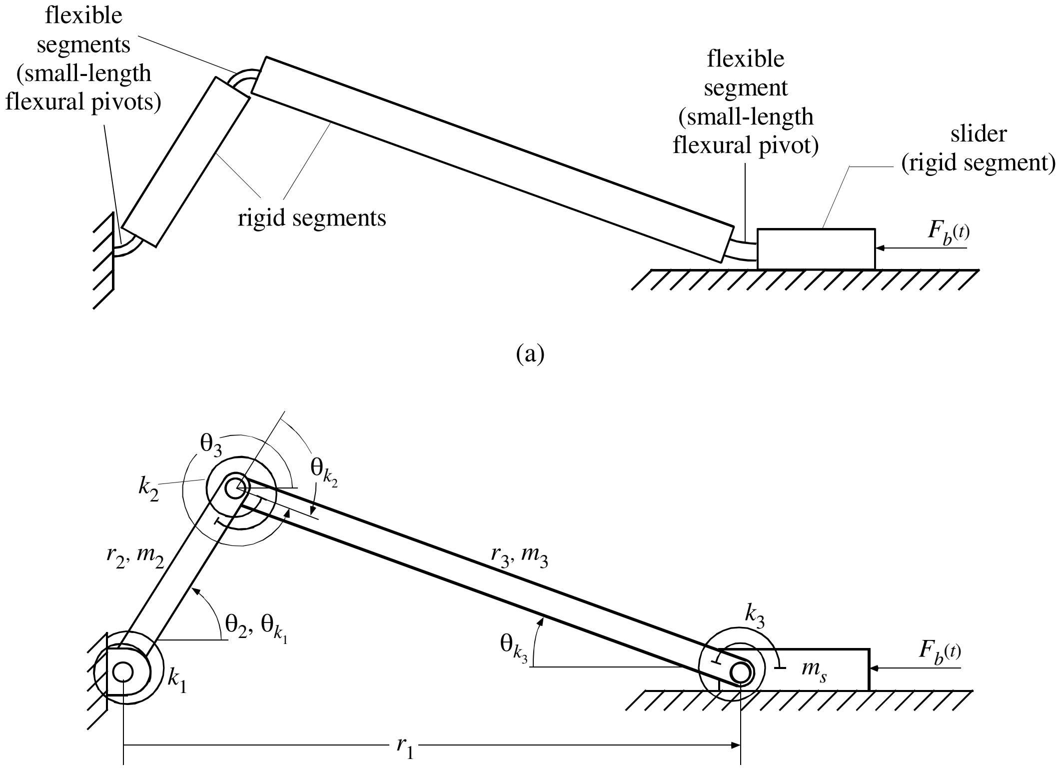

(a)

(b)

Figure 6.1 (a) An example constant-force mechanism (specifically, configuration Class 3A-n, with three small-length flexural pivots), and (b) the generalized pseudo-rigid-body model for the constant-force mechanism.

of Figure 6.1 (a), x_b is identical to r_1, but not all constant-force mechanism configurations have x_b equal to r_1. This small detail is easily dealt with, as illustrated by the derivation of the equation of motion for configuration Class 1A-d (see Chapter 3), and the first of the following three cases.

Figure 6.2 gives more examples of how to form the pseudo-rigid-body model, using three more configurations. Figure 6.2 (a) shows the pseudo-rigid-body model for configuration Class 1A-c, which is the inverse configuration of Class 1A-d, the mecha-

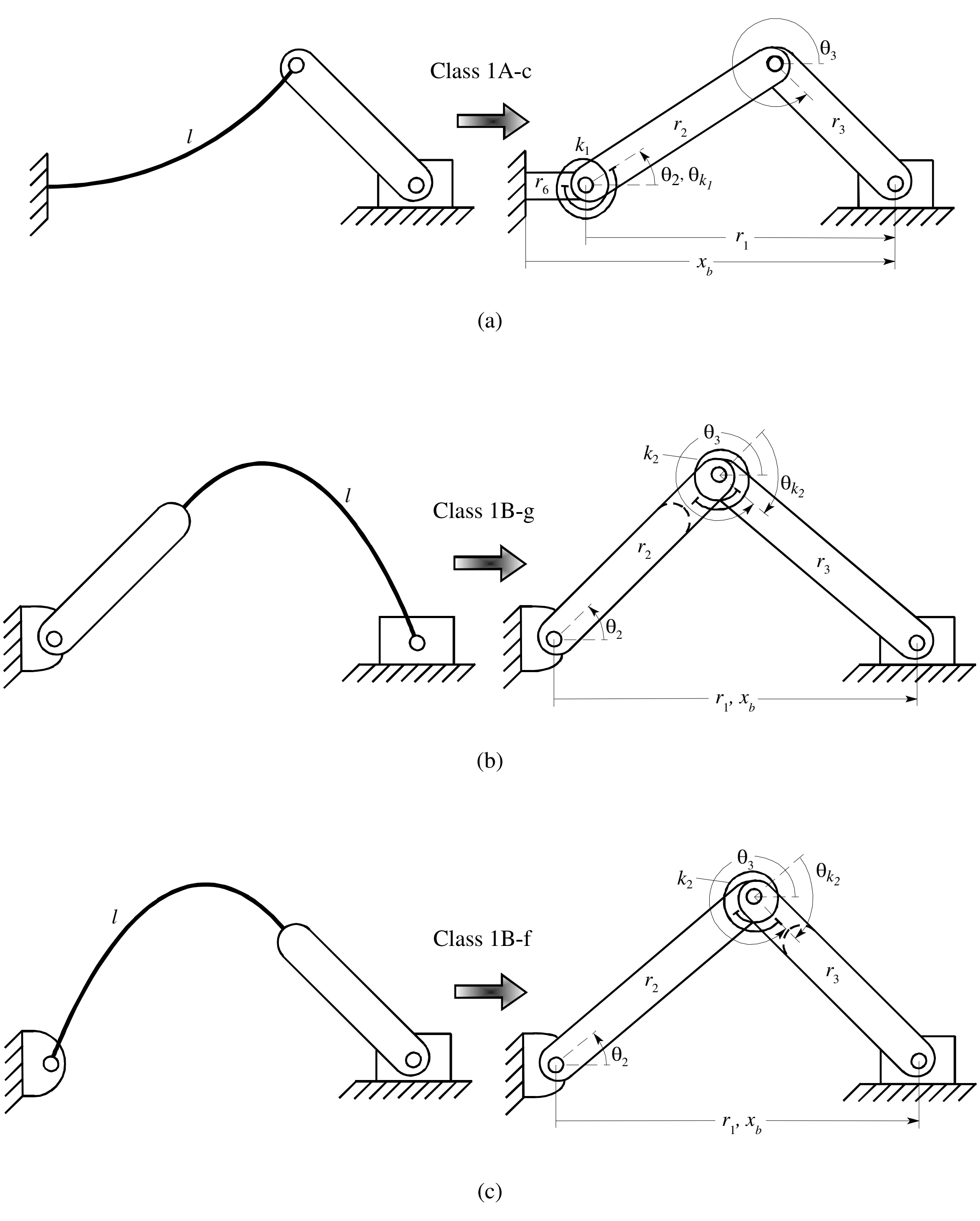

Figure 6.2 Pseudo-rigid-body models of three constant-force mechanism configurations (note that ratios of rigid to flexible segment lengths are not represented exactly).

nism used for the dynamic model derivation of Chapter 3. By inverse configuration is meant that everything between where the mechanism attaches to ground and where it attaches to the slider is flipped horizontally. Figure 6.2 (b) and (c) show configuration Class 1B-g, and its inverse configuration, Class 1B-f.

Each of these three examples show how to account for the “stubby” link generated by application of the pseudo-rigid-body rule for a cantilever beam with a force at the free end. In the first example (Figure 6.2 (a)), the stubby link becomes link 6 with length r_6. When dealing with an actual compliant mechanism, the imaginary pin about which the pseudo-rigid-body link (in this case, r_2) pivots is difficult to locate, compared to where the flexible segment physically begins or ends. Defining x_b as the horizontal vector originating where the constant-force spring begins (where it attaches to ground) and ending where the spring ends (where it attaches to the slider) makes sense when working with the physical compliant mechanism. In this case, as in the case of configuration Class 1A-d (Chapter 3), it makes sense to define

$$x_b = r_1 + r_6 \tag{6.1}$$

For most other compliant constant-force mechanisms, this is a moot point. Even some of the configurations incorporating long flexible segments, such as the examples of Figure 6.2 (b) and (c), swallow up the stubby link as an extension of the original compliant mechanism’s rigid link. The curved dashed line in both diagrams represents the length of the rigid link before addition of the stubby link. Since this occurs at the pseudo-rigid-body model's central pin rather than at the mechanism extremities, the model's length is the same as the mechanism's length, and

$$x_b = r_1 \tag{6.2}$$

6.2 Generalized Dynamic Model

With a generalized pseudo-rigid-body model clearly defined for all configurations, the dynamic model of Chapter 3 can now be generalized for all compliant constant-force mechanisms.

Recall the definition of the Lagrangian $\mathscr{L} = T - V$, equation (3.5). The formulation of the potential energy T of the system, equation (3.7), remains exactly the same for the generalized model. However, the kinetic energy V, equation (3.9), changes to

$$V = \frac{1}{2}k_1\theta_{k_1}{}^2 + \frac{1}{2}k_2\theta_{k_2}{}^2 + \frac{1}{2}k_3\theta_{k_3}{}^2 \tag{6.3}$$

The following equations recast the variables in V in terms of the generalized coordinate θ_2:

$$\theta_{k_1} = \theta_2 \tag{6.4}$$

$$\theta_{k_2} = \theta_2 + \operatorname{asin}\left(\frac{r_2}{r_3}\sin\theta_2\right) \tag{6.5}$$

$$\theta_{k_3} = \operatorname{asin}\left(\frac{r_2}{r_3}\sin\theta_2\right) \tag{6.6}$$

Recollect that Lagrange's formulation requires the partial derivatives of the Lagrangian with respect to the generalized coordinate θ_2 and its time derivative $\dot{\theta}_2$ to form the equation of motion for the system:

$$\frac{d}{dt}\left(\frac{\partial \mathcal{L}}{\partial \dot{\theta}_2}\right) - \frac{\partial \mathcal{L}}{\partial \theta_2} = Q_{\theta_2} \tag{6.7}$$

Since V is the only part of the derivation that is new, all that remains to be done is to calculate the derivatives of the new terms and substitute them into the previously derived equation of motion. The previous potential energy term (let's call it V_o) led directly to the static term of the equation of motion (see equation (3.19)):

$$\frac{d}{dt}\left(\frac{\partial(-V_o)}{\partial \dot{\theta}_2}\right) - \frac{\partial(-V_o)}{\partial \theta_2} = \frac{k \operatorname{asin}\left(\frac{r_2}{r_3}\sin\theta_2\right) r_2 \cos\theta_2}{\sqrt{r_3^2 - r_2^2 \sin^2\theta_2}} \tag{6.8}$$

The newly modified formulation of V results in

$$\begin{aligned}\frac{d}{dt}\left(\frac{\partial(-V)}{\partial \dot{\theta}_2}\right) - \frac{\partial(-V)}{\partial \theta_2} &= k_1\theta_2 + k_2\left(\theta_2 + \operatorname{asin}\left(\frac{r_2}{r_3}\sin\theta_2\right)\right)\left(1 + \frac{r_2\cos\theta_2}{\sqrt{\xi}}\right) \\ &+ \frac{k_3 \operatorname{asin}\left(\frac{r_2}{r_3}\sin\theta_2\right) r_2 \cos\theta_2}{\sqrt{r_3^2 - r_2^2 \sin^2\theta_2}}\end{aligned} \tag{6.9}$$

This completes the necessary changes to make the dynamic model of Chapter 3 applicable to any compliant constant-force mechanism. The generalized dynamic model is given next in its entirety.

6.2.1 EQUATION OF MOTION FOR THE COMPLIANT CONSTANT-FORCE MECHANISM

The following equation of motion represents a closed-form dynamic model for the compliant constant-force mechanism, whose generic pseudo-rigid-body model is represented in Figure 6.1.

$$
\begin{aligned}
&\Bigg[m_3\Bigg(\frac{1}{2}\frac{r_2^{\,5}\sin^3\theta_2\cos^2\theta_2}{\xi^{3/2}}+\frac{1}{3}\frac{r_2^{\,4}r_3^{\,2}\sin\theta_2\cos^3\theta_2}{\xi^2}-\frac{1}{2}\frac{r_2^{\,3}\sin^3\theta_2}{\sqrt{\xi}}\\
&+\frac{r_2^{\,3}\sin\theta_2\cos^2\theta_2}{\sqrt{\xi}}-\frac{1}{3}\frac{r_2^{\,2}r_3^{\,2}\sin\theta_2\cos\theta_2}{\xi}+r_2^{\,2}\sin\theta_2\cos\theta_2\Bigg)\\
&+m_s\Bigg(\frac{r_2^{\,6}\sin^3\theta_2\cos^3\theta_2}{\xi^2}+\frac{r_2^{\,5}\sin^3\theta_2\cos^2\theta_2}{\xi^{3/2}}-\frac{r_2^{\,4}\sin^3\theta_2\cos\theta_2}{\xi}\\
&+\frac{r_2^{\,4}\sin\theta_2\cos^3\theta_2}{\xi}+2\frac{r_2^{\,3}\sin\theta_2\cos^2\theta_2}{\sqrt{\xi}}-\frac{r_2^{\,3}\sin^3\theta_2}{\sqrt{\xi}}+r_2^{\,2}\sin\theta_2\cos\theta_2\Bigg)\Bigg]\dot{\theta}_2^{\,2}\\
&+\Bigg[m_2\left(\frac{1}{3}r_2^{\,2}\right)+m_3\Bigg(\frac{r_2^{\,3}\sin^2\theta_2\cos\theta_2}{\sqrt{\xi}}+\frac{1}{3}\frac{r_2^{\,2}r_3^{\,2}\cos^2\theta_2}{\xi}+r_2^{\,2}-r_2^{\,2}\cos^2\theta_2\Bigg)\\
&+m_s\Bigg(\frac{r_2^{\,4}\sin^2\theta_2\cos^2\theta_2}{\xi}+2\frac{r_2^{\,3}\sin^2\theta_2\cos\theta_2}{\sqrt{\xi}}+r_2^{\,2}\sin^2\theta_2\Bigg)\Bigg]\ddot{\theta}_2\\
&+k_1\theta_2+k_2\left(\theta_2+\operatorname{asin}\left(\frac{r_2}{r_3}\sin\theta_2\right)\right)\left(1+\frac{r_2\cos\theta_2}{\sqrt{\xi}}\right)\\
&+\frac{k_3\operatorname{asin}\left(\frac{r_2}{r_3}\sin\theta_2\right)r_2\cos\theta_2}{\sqrt{\xi}}-\tau_C-\tau_{um}=\tau_{F_b}
\end{aligned}
\tag{6.10}
$$

where

$$\xi = r_3^{\,2}-r_2^{\,2}\sin^2\theta_2 \tag{6.11}$$

$$\tau_C = C\theta_2 \operatorname{sgn}(\dot{\theta}_2) \tag{6.12}$$

$$F_b = \tau_{F_b} \Big/ \frac{\partial x_b}{\partial \theta_2} \tag{6.13}$$

and

$$\frac{\partial x_b}{\partial \theta_2} = -r_2 \sin\theta_2 - \frac{{r_2}^2 \sin\theta_2 \cos\theta_2}{\sqrt{\xi}} \tag{6.14}$$

Equations (6.12) through (6.14) are given in the dynamic model derivation of Chapter 3, but are repeated here for completeness.

CHAPTER 7

Testing of Additional Mechanisms

This chapter should be read in conjunction with Chapter 4, *Experimental Setup*, and Chapter 5, *Empirical and Theoretical Findings*. Here, dynamic tests from four additional compliant constant-force mechanisms are evaluated. The first two are of configuration Class 1A-d, the same configuration as the test mechanism described in Chapter 4, with results given in Chapter 5. The latter two are of configuration Class 1B-g, whose pseudo-rigid-body model is shown in Figure 6.2 (b).

7.1 Mechanism Description

Figure 7.1 shows one of the Class 1B-g mechanisms, (a) fully expanded and (b) fully compressed (a deflection of $\Delta x_b = 0.40(r_2 + r_3)$). Notice the large deflection of the flexible segments.

Figure 7.2 shows all of the mechanisms tested in this thesis (only half of each symmetric mechanism is pictured). The mechanism names in Figure 7.2 correspond to the headings above the mechanism parameters listed in Table 7.1 (parameters for mechanism

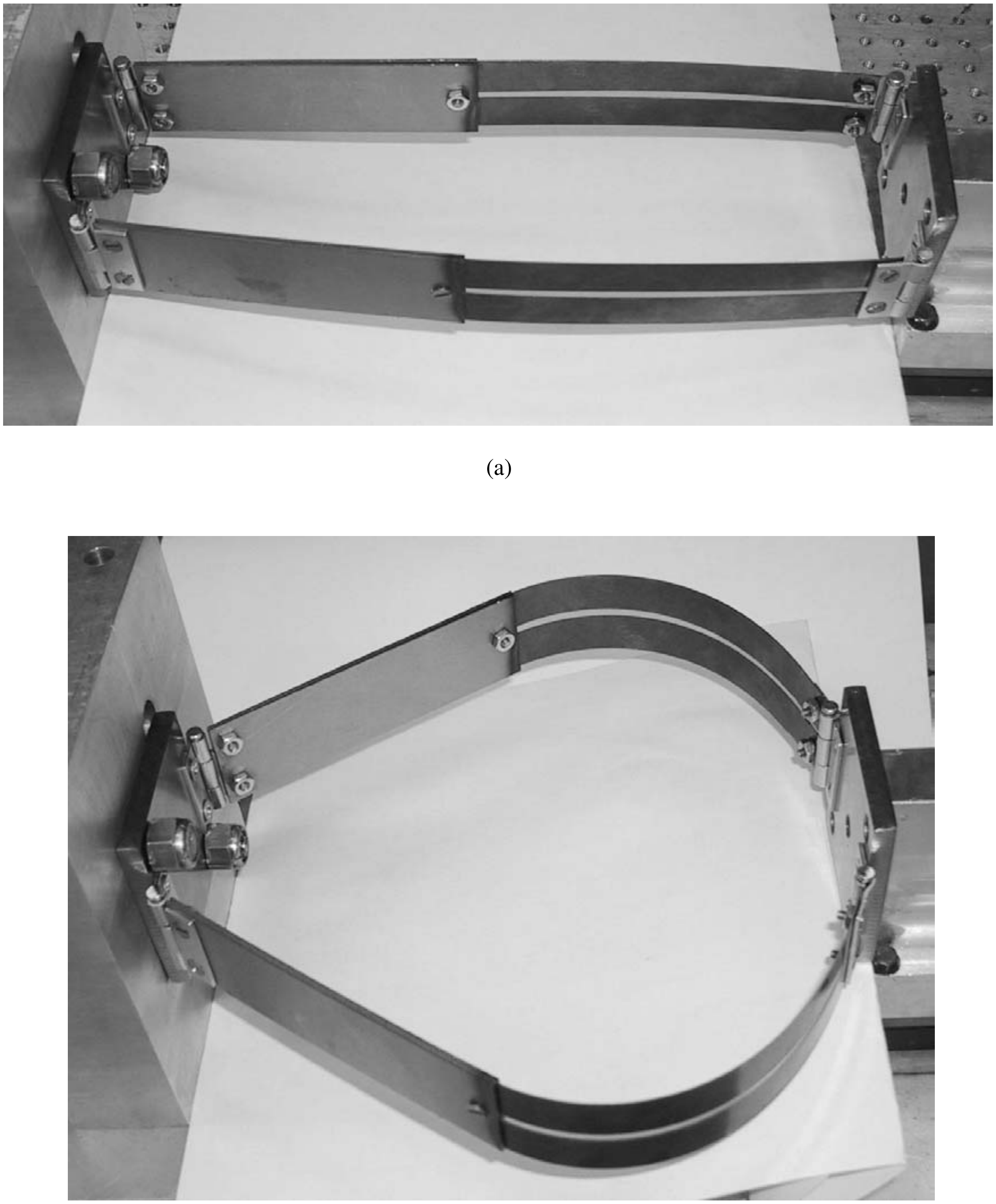
(a)

(b)

Figure 7.1 Mechanism Class 1B-g I, one of two Class 1B-g mechanisms tested; (a) fully expanded and (b) fully compressed.

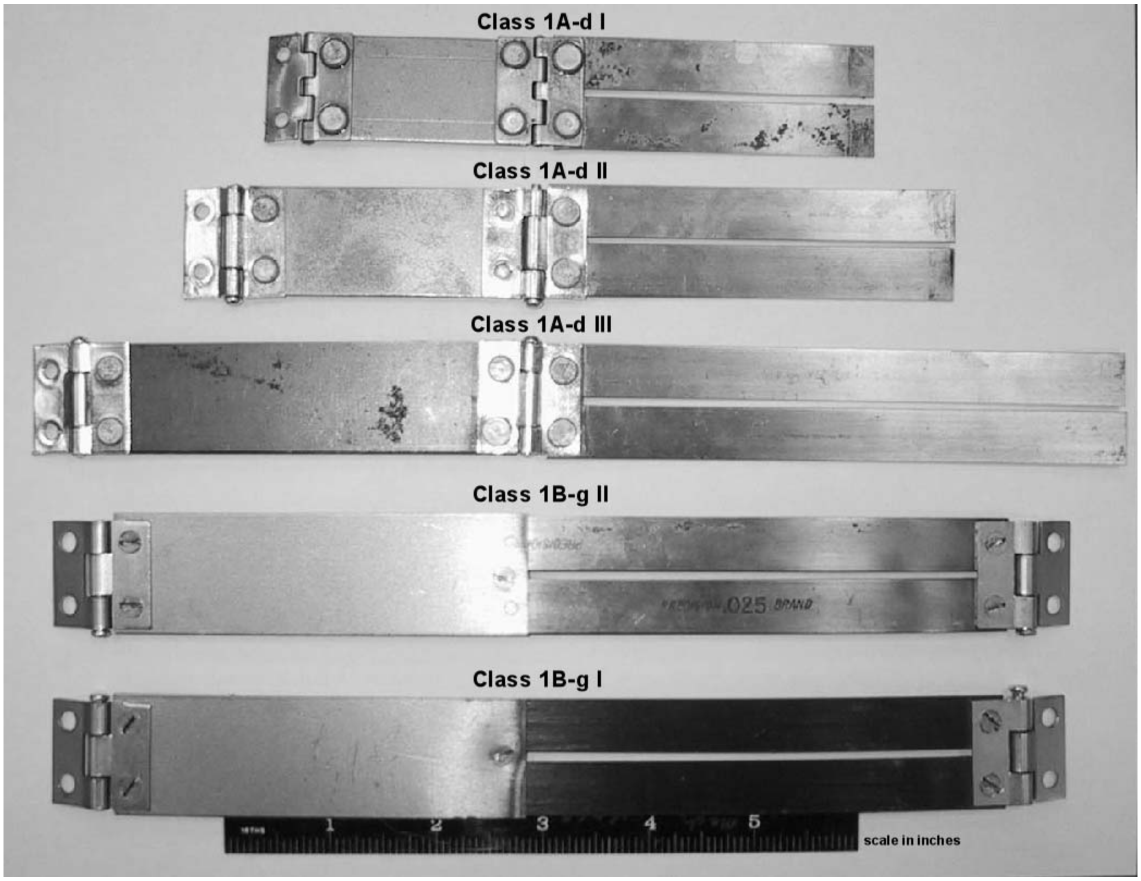

Figure 7.2 The five constant-force mechanisms tested in this thesis.

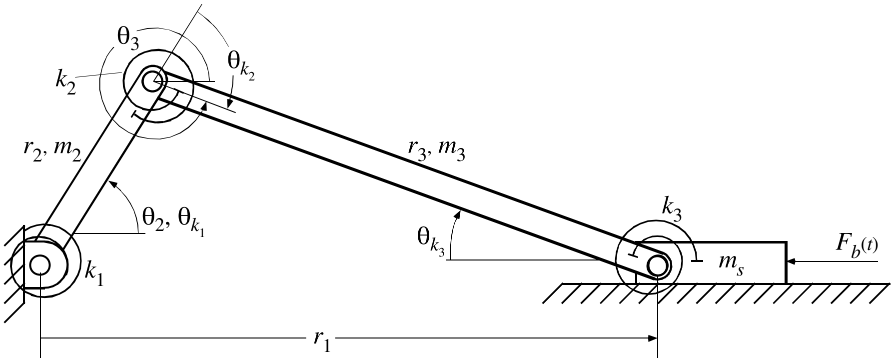

Figure 7.3 The generalized pseudo-rigid-body model for the compliant constant-force mechanism.

TABLE 7.1 Mechanism parameters (parameters used directly in dynamic model are emphasized).

Parameter	Mechanism Class 1A-d II	Mechanism Class 1A-d III
r_2	7.176 cm (2.825 in)	10.706 cm (4.215 in)
r_3	8.105 cm (3.191 in)	12.093 cm (4.761 in)
r_6	1.430 cm (0.563 in)	2.134 cm (0.840 in)
b	2.540 cm (1.000 in)	2.540 cm (1.000 in)
h	0.064 cm (0.025 in)	0.064 cm (0.025 in)
I	$5.420 \times 10^{-13}\ m^4\ (1.302 \times 10^{-6}\ in^4)$	$5.420 \times 10^{-13}\ m^4\ (1.302 \times 10^{-6}\ in^4)$
E	$206.8\ GPa\ (30 \times 10^6\ psi)$	$206.8\ GPa\ (30 \times 10^6\ psi)$
m_2	24.4 g (0.0537 lb_m)	35.8 g (0.0789 lb_m)
m_3	11.7 g (0.0259 lb_m)	16.8 g (0.0369 lb_m)
m_s	86.5 g (0.1908 lb_m)	87.0 g (0.1918 lb_m)
k_3	2.648 N·m (23.44 in·lb_f)	1.775 N·m (15.71 in·lb_f)
C	0.121 N·m (1.070 in·lb_f)	0.029 N·m (0.258 in·lb_f)
τ_{um}	–0.321 N·m (–2.84 in·lb_f)	–0.158 N·m (–1.40 in·lb_f)

Parameter	Mechanism Class 1B-g I	Mechanism Class 1B-g II
r_2	11.908 cm (4.688 in)	11.908 cm (4.668 in)
r_3	10.121 cm (3.985 in)	10.121 cm (3.985 in)
r_6		
b	2.540 cm (1.000 in)	2.540 cm (1.000 in)
h	0.038 cm (0.015 in)	0.064 cm (0.025 in)
I	$1.171 \times 10^{-13}\ m^4\ (2.813 \times 10^{-7}\ in^4)$	$5.420 \times 10^{-13}\ m^4\ (1.302 \times 10^{-6}\ in^4)$
E	$206.8\ GPa\ (30 \times 10^6\ psi)$	$206.8\ GPa\ (30 \times 10^6\ psi)$
m_2	45.0 g (0.0993 lb_m)	50.1 g (0.1105 lb_m)
m_3	9.2 g (0.0202 lb_m)	14.3 g (0.0315 lb_m)
m_s	85.5 g (0.1885 lb_m)	85.5 g (0.1885 lb_m)
k_2	0.4581 N·m (4.054 in·lb_f)	2.121 N·m (18.77 in·lb_f)
C	0.018 N·m (0.16 in·lb_f)	0.144 N·m (1.27 in·lb_f)
τ_{um}	–0.159 N·m (–1.41 in·lb_f)	–1.018 N·m (–9.01 in·lb_f)

Class 1A-d I already appear in Table 4.1). Repeated in Figure 7.3 for quick reference with the table is the generalized pseudo-rigid-body model for the constant-force mechanism. Recall that the variables *b*, *h*, and *I* are the width, thickness, and area moment of inertia of the flexible segment's cross section; *E* is the modulus of elasticity of the flexible segment; and r_6 is the length of the pseudo-rigid-body stubby link, when located at either of the mechanism's extremities (see discussion on page 55). As in the case of the first test mechanism (see Section 4.1), the parameters tabulated in Table 7.1 are taken from half of each symmetric mechanism.

Refer to Sections 3.5 and 3.6 starting on page 27 for treatment of *C* and τ_{um}. Static data from which *C* and τ_{um} were empirically determined can be found in APPENDIX C. No clear pattern emerges in the determination of values for *C* and τ_{um}, other than the mechanisms designed for the highest force output (see Table 7.2) appear to have larger values for τ_{um}.

The two Class 1A-d mechanisms are constructed just as the first test mechanism (Class 1A-d I). The two Class 1B-g mechanisms are constructed with two long strips of steel shim stock (the first with thickness 0.38 *mm* (0.015 *in*), and the second with thickness 0.64 *mm* (0.025 *in*)). To constrain the rigid segment of each Class 1B-g mechanism so as to be rigid, two pieces of sheet metal (each 1.19 *mm* (0.047 *in*) thick) are bolted together, confining the flexible shim stock between them. Utility hinges and steel plates of the same dimensions and masses as mechanism Class 1A-d I serve as pins, ground plate, and shared slider (see Section 4.1).

Every mechanism tested in this thesis was designed to exhibit constant-force for a maximum of 40% deflection, or a deflection of $\Delta x_b = 0.40(r_2 + r_3)$. Table 7.2 lists each mechanism's extended length $x_{b\ \max}$ and fully compressed length $x_{b\ \min}$. It also gives each device's nominal constant-force F_{nom} (doubled for the mechanism pairs), as derived in Howell (2001):

$$F_{nom} = 2\frac{k_3}{r_3}\Phi \qquad (7.1)$$

for the Class 1A mechanisms, and

$$F_{nom} = 2\frac{k_2}{r_3}\Phi \qquad (7.2)$$

for the Class 1B mechanisms. The values for average nondimensionalized constant-force Φ for 40% deflection Class 1A and Class 1B constant-force mechanisms, tabulated in Millar et al. (1996), are 0.4773 and 2.1513, respectively.

7.2 Experimental Setup Modification

For the testing of mechanisms Class 1A-d II, Class 1A-d III, Class 1B-g I, and Class 1B-g II, the force transducer bolted in-line between the actuator block and test

TABLE 7.2 Extended and fully compressed mechanism lengths; nominal force for each mechanism.

Parameter	Mechanism Class 1A-d II	Mechanism Class 1A-d III
$x_{b\ \max}$	16.711 cm (6.579 in)	24.933 cm (9.816 in)
$x_{b\ \min}$	10.598 cm (4.173 in)	15.813 cm (6.226 in)
F_{nom}	31.19 N (7.018 lb_f)	14.01 N (3.153 lb_f)
Parameter	**Mechanism Class 1B-g I**	**Mechanism Class 1B-g II**
$x_{b\ \max}$	22.029 cm (8.673 in)	22.029 cm (8.673 in)
$x_{b\ \min}$	13.218 cm (5.204 in)	13.218 cm (5.204 in)
F_{nom}	19.47 N (4.381 lb_f)	90.15 N (20.284 lb_f)

mechanism in the experimental setup (refer to page 38) was replaced with an Omega 25-*lb*-capacity through-hole load cell, specification LC125-312-25, with a nonlinearity of $\pm 1.0\,\%$ of full-scale, or resolution error of $\pm 1.112\ N\ \ (0.25\ lb_f)$. Force measurement errors due to unwanted torque from the load cell's placement between the actuator block and slider are greatly improved by the modification because the load cell freely orients itself between the surfaces of the actuator block and slider.

7.3 Test Results

Complete test results for all five constant-force mechanisms tested in this thesis are given in APPENDIX B, *Dynamic Data*. Figures 7.4 to 7.7 summarize these results with "goodness of fit" plots like the one in Section 5.3 on page 49 (Figure 5.5). Each figure shows how well the modeled force matches the measured force for each frequency tested. Also shown is the relative error when τ_C and τ_{um} are neglected in the modeled force calculation. All four of the mechanisms tested in this chapter have a goodness of fit of modeled to measured force of 83% or better, as indicated by the figures, and most of the test frequencies for the mechanisms show a much better fit than 83%.

These mechanisms show significantly higher relative error between measured and modeled force than mechanism Class 1A-d I (Figure 5.5). This is likely due to two factors: (1) less care was taken in manufacturing the latter mechanisms than in fabricating mechanism Class 1A-d I, including placement of the hinges to avoid binding, and selection of the hinges themselves – the hinges for the latter four test mechanisms had considerably more tolerance in the pin joints; and (2) the load cell modification mentioned in

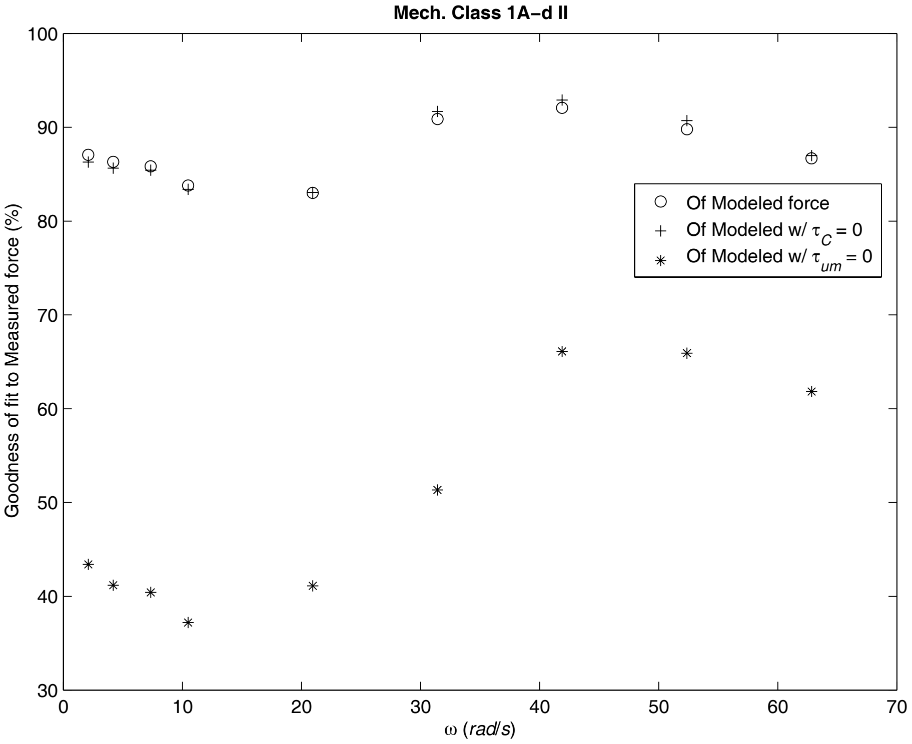

Figure 7.4 Goodness of fit of modeled to measured force; goodness of fit of modeled force, minus τ_C and τ_{um}, for mechanism Class 1A-d II.

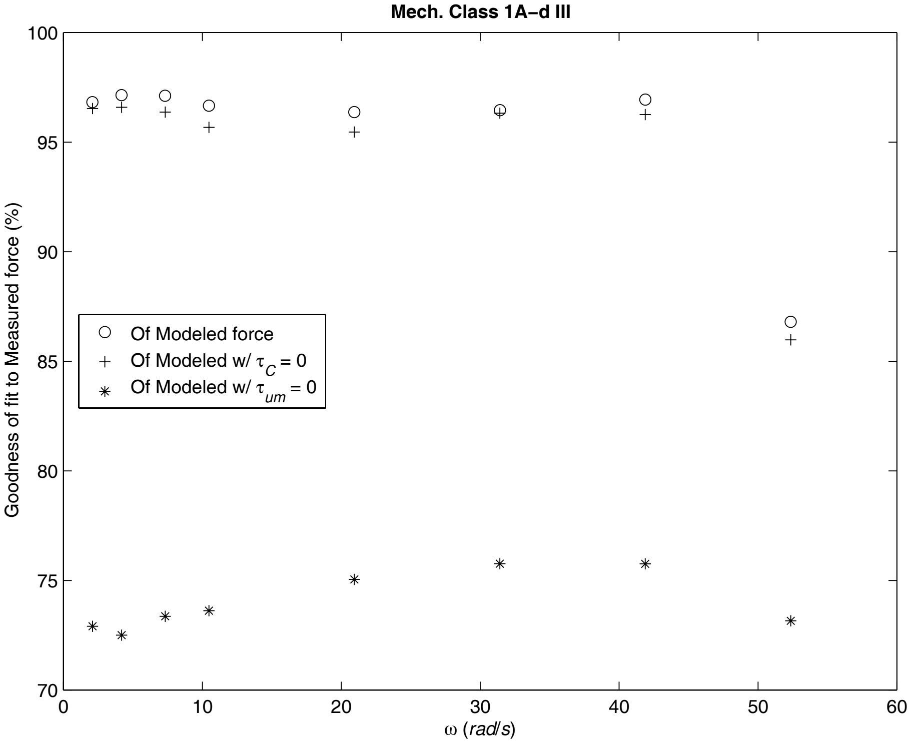

Figure 7.5 Goodness of fit of modeled to measured force; goodness of fit of modeled force, minus τ_C and τ_{um}, for mechanism Class 1A-d III.

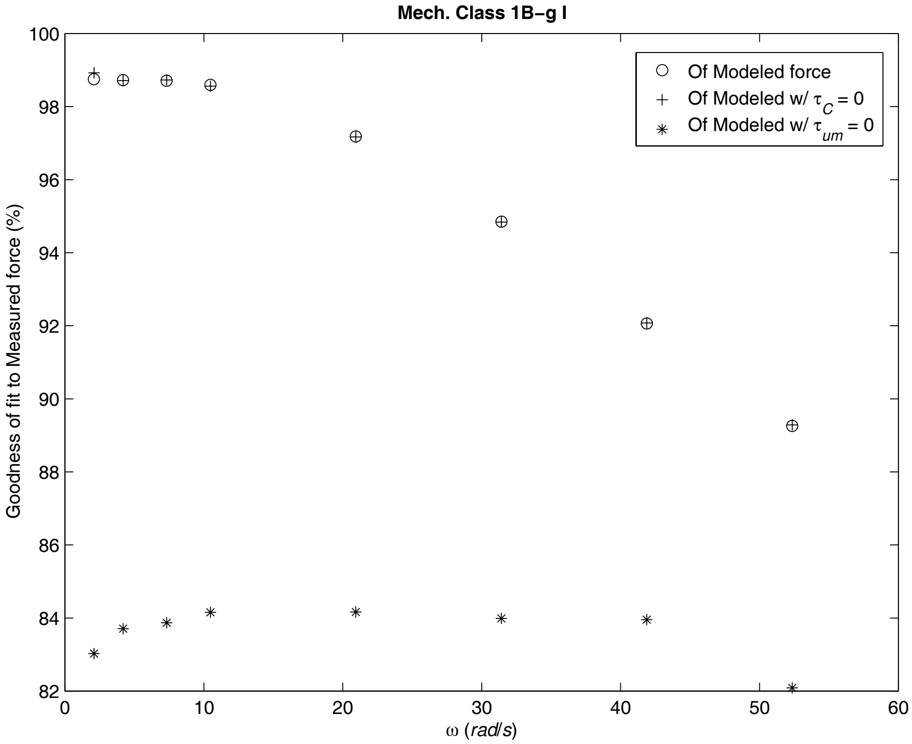

Figure 7.6 Goodness of fit of modeled to measured force; goodness of fit of modeled force, minus τ_C and τ_{um}, for mechanism Class 1B-g I.

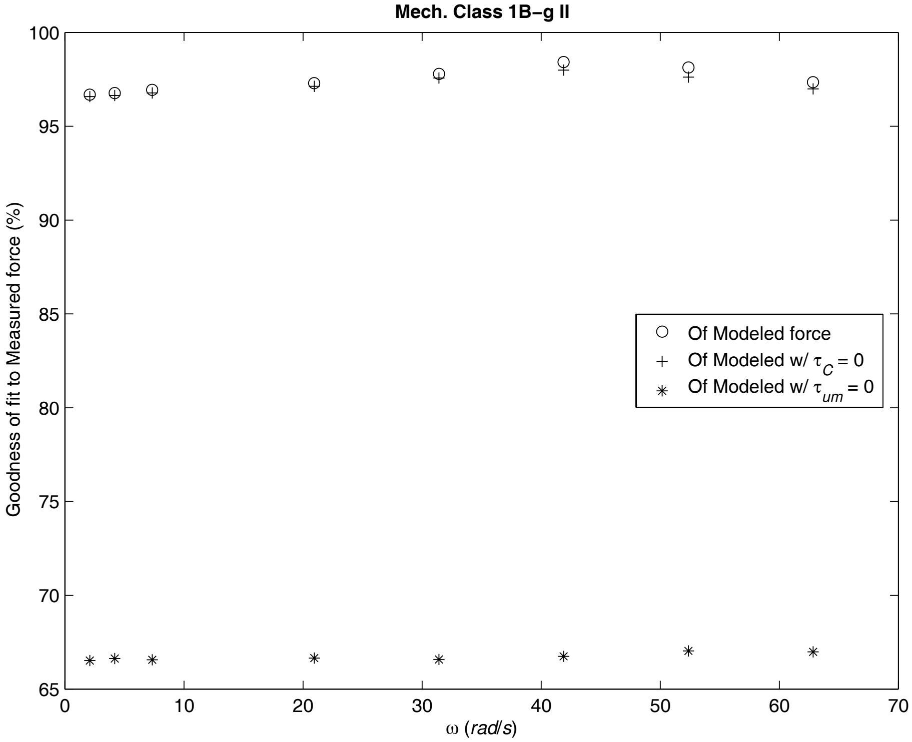

Figure 7.7 Goodness of fit of modeled to measured force; goodness of fit of modeled force, minus τ_C and τ_{um}, for mechanism Class 1B-g II.

Section 7.2 had the unfortunate effect of reducing force measurement resolution by an order of magnitude, resulting in less precise data, particularly for lower force magnitudes.

As discovered in Figure 5.5, the value of τ_{um} is much more important to the dynamic model than is τ_C for the four mechanisms. Also, the mechanisms designed to output a smaller force (F_{nom}) are less dependent on accurate values of τ_{um} to give desirable results, because τ_{um} tends to be smaller for smaller output constant-force mechanisms.

For a better view of how the modeled force compares with the measured force for each test mechanism, see APPENDIX B. A full cycle of modeled vs. measured force, for each frequency tested, is pictured there.

7.4 Dynamic Characterization

Recall from the discussion of Section 5.2 *Dynamic Characterization of the Model* on page 44 that a closer look at the behavior of mechanism Class 1A-d I as a function of frequency reveals something of interest. There exists a range of frequencies shown in Figure 5.4 over which the mechanism exhibits better constant-force behavior than at static levels. To discover if the four additional test mechanisms possess the same dynamic trait, frequency plots of the dynamic models of each of the four mechanisms were generated. These are presented in Figures 7.8 to 7.11.

All four mechanisms do exhibit similar dynamic behavior, as readily seen in the frequency plots. The peak-to-peak force difference of each dynamic model dips below its zero frequency value over the initial range of frequencies, just as in Figure 5.4. But the

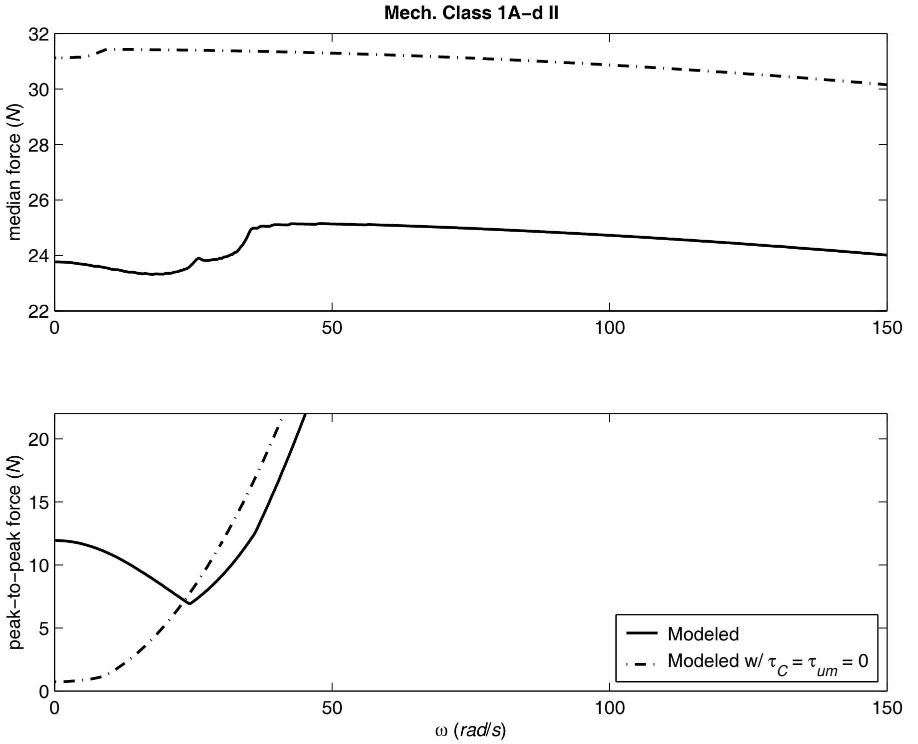

Figure 7.8 The median force and peak-to-peak force difference as a function of frequency for mechanism Class 1A-d II.

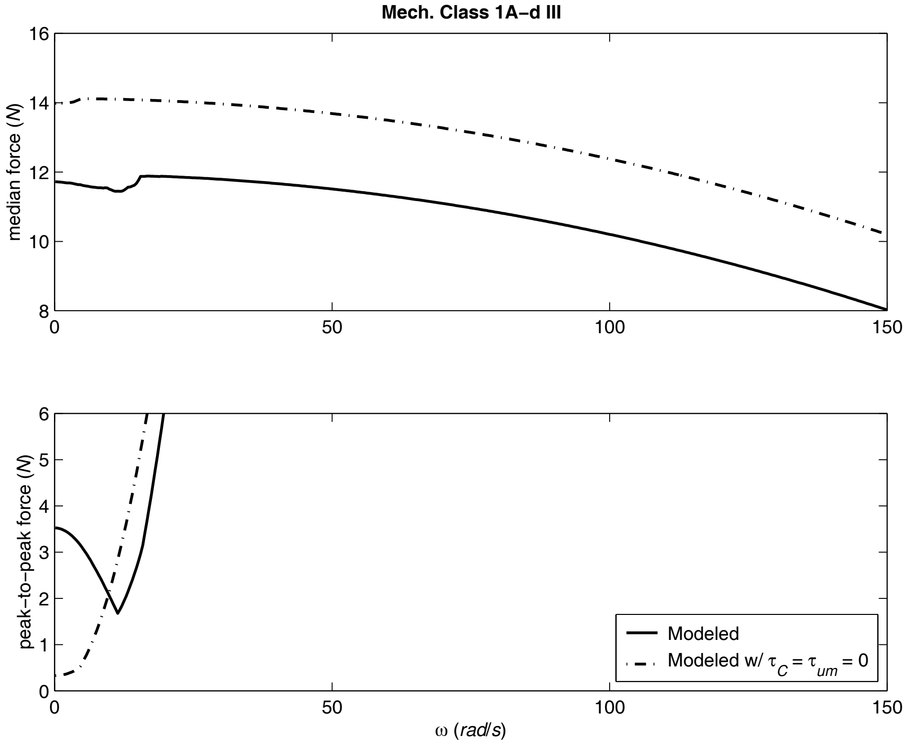

Figure 7.9 The median force and peak-to-peak force difference as a function of frequency for mechanism Class 1A-d III.

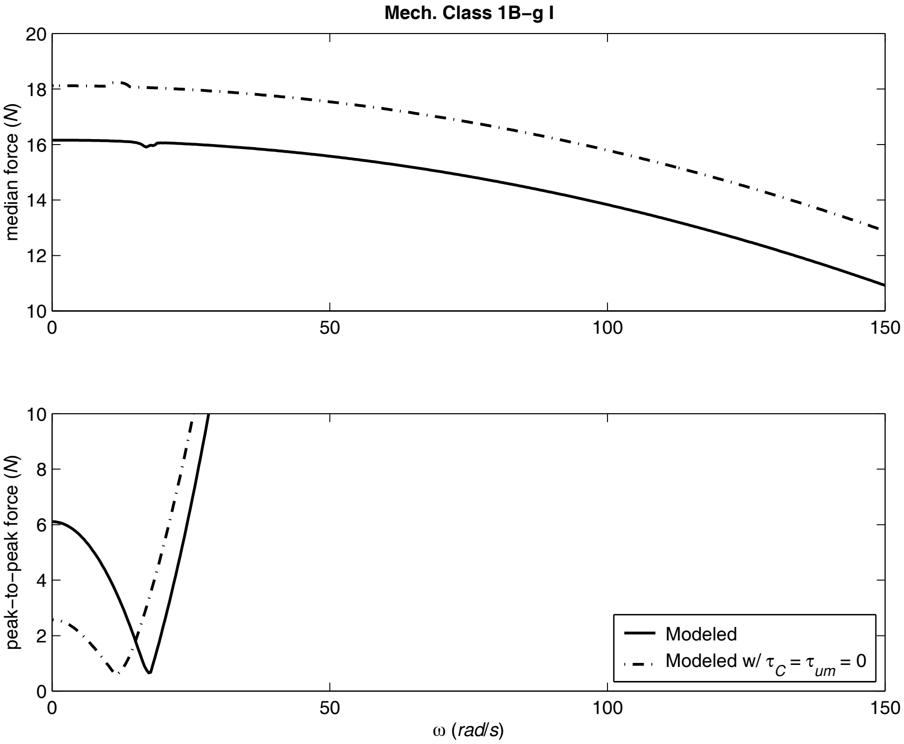

Figure 7.10 The median force and peak-to-peak force difference as a function of frequency for mechanism Class 1B-g I.

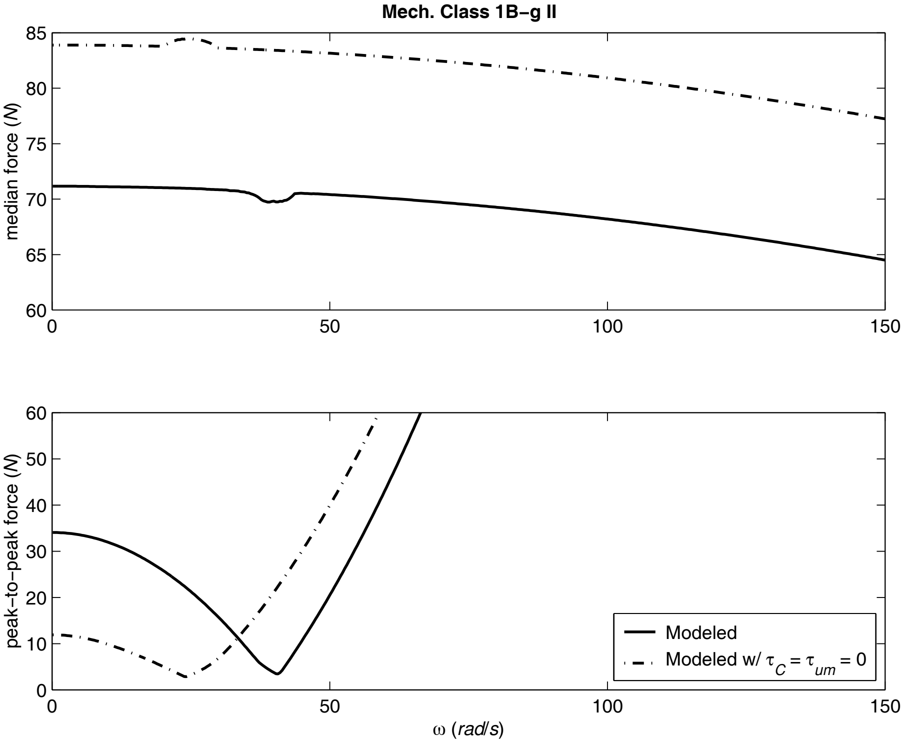

Figure 7.11 The median force and peak-to-peak force difference as a function of frequency for mechanism Class 1B-g II.

dynamic model with τ_C and τ_{um} set to zero doesn't behave quite the same for the Class 1B-g mechanisms as it does for Class 1A-d (see discussion on page 46); Figures 7.10 and 7.11 show a dip in the peak-to-peak force from its initial magnitude. Apparently, there is more to be learned about the differences between configurations. Also, the mechanisms designed with the highest nominal force F_{nom} appear to exhibit improved constant-force behavior over a broader range of frequencies.

7.5 Conclusions

The results presented in this chapter corroborate the findings of Chapter 5. Now, instead of one mechanism and one configuration, five different mechanisms comprising two configurations of the compliant constant-force mechanism show good agreement between dynamic model and physical device. In addition, the validated dynamic model of each of the five mechanisms reveals a shared dynamic characteristic: a range of frequencies where the output force demonstrates constant-force better than when the mechanism cycles statically.

Unfortunately, the dynamic model in its current state of development requires that a mechanism first be constructed to experimentally determine the Coulomb friction and unmodeled torque terms, τ_C and τ_{um}. These terms are necessary for the model to accurately predict the mechanism's dynamic response. Although there is no clear trend delineating how to select these experimentally determined values, more research into this area could simplify compliant constant-force mechanism design and analysis.

In addition, more attention could be directed to the correlation between large designed force output (F_{nom}), high unmodeled torque τ_{um}, and a broader range over which "better-than-static" constant-force is observed, as noted throughout this chapter.

CHAPTER 8

Conclusions and Recommendations

The primary accomplishment of this thesis is to show that the pseudo-rigid-body model can be used to obtain a viable, closed-form dynamic model for the compliant constant-force mechanism. Although dozens of methods for dynamic modeling of compliant mechanisms exist, few of them result in a closed-form mathematical solution. While using the pseudo-rigid-body model for dynamic analysis does not result in a dynamic model precisely true to the compliant mechanism, it has been shown that, at least for two classes of compliant mechanisms (the parallel-guiding mechanism (Lyon et al., 1997) and the constant-force mechanism), it produces very accurate results. In light of the simplicity the pseudo-rigid-body model affords, this is a beneficial discovery, and the findings of this work ensure confidence in using the pseudo-rigid-body model for compliant mechanism dynamic analysis in the future.

An unforeseen outcome of this research is that because every compliant constant-force mechanism shares the same pseudo-rigid-body model (in fact this is how most of the configurations were discovered, by the method of type synthesis performed on a single configuration), a generalized dynamic model can easily be formed, representing not one, but 28 different configurations. For all other dynamic methods researched, a separate treatment would be required to model each of the 28 configurations. Using the pseudo-rigid-body model common to every configuration, a dynamic model can be derived just once.

The dynamic model derived for the constant-force compliant mechanism reveals an advantageous dynamic property exhibited by the device, which is also borne out by empirical data. The constant-force mechanism yields better constant-force behavior for certain driving frequencies than it does statically. Obviously, the ability to manipulate this behavior would be useful to anyone designing compliant constant-force mechanisms. By changing mechanism parameters, a designer can optimize this feature to meet his or her own needs.

A less than satisfactory aspect of the constant-force mechanism dynamic model is having to empirically determine the static terms of Coulomb friction τ_C and unmodeled torque τ_{um}. A better understanding of these two parameters would be useful, particularly any correlation between large values of τ_{um}, a large designed output force, and a broader frequency range of “better-than-static” constant-force behavior (in comparison to constant-force springs designed for smaller forces). Further research into this area could lead to a more complete understanding of the constant-force mechanism, and the force-deflection character of compliant mechanisms in general, both static and dynamic. A good starting point may be to linearize the dynamic model about several operating points to discover the precise cause of the peak-to-peak force difference illustrated by the frequency plots of Figure 5.4 and Figures 7.8 to 7.11. Perhaps another point that should be considered is that if greater care were taken in the construction of the constant-force mechanism (i.e., using bearings instead of utility hinges, exploring more efficient fabrication methods), the necessity of having to compensate for terms like τ_C and τ_{um} might be minimized. Failing this, a treatment like that taken by Bahgat et al. (1981) could be considered, where multiple revolute clearances are incorporated into the dynamic equation using Lagrangian mechanics. Lastly, more investigation is needed in the areas of fatigue and creep for compliant constant-force mechanisms.

References

Ananthasuresh, G.K., and Kota, S., 1995, "Designing Compliant Mechanisms," *Mechanical Engineering*, Vol. 117, No. 11, pp. 93-96.

Atanackovic, T.M., and Cveticanin, L.J., 1996, "Dynamics of Plane Motion of an Elastic Rod," ASME *Journal of Applied Mechanics*, Vol. 63, pp. 392-398.

Bisshopp, K.E., and Drucker, D.C., 1945, "Large Deflection of Cantilever Beams," *Quarterly of Applied Mathematics*, Vol. 3, No. 3, pp. 272-275.

Bahgat, B.M., Osman, M.O.M., and Sankar, T.S., 1981, "An Approach for Dynamic Analysis of Mechanical Systems with Multiple Clearances Using Lagrangian Mechanics," contributed by the Design Engineering Division of the ASME for presentation at the Design Engineering Technical Conference, pp. 1-8.

Burns, R.H., and Crossley, F.R.E, 1968, "Kinetostatic Synthesis of Flexible Link Mechanisms," ASME Paper No. 68-Mech-36.

Darcovich, J., Angeles, J., and Misra, A.K., 1992, "Dynamics of Single-Loop Mechanisms with Flexible Links," *Flexible Mechanisms, Dynamics, and Analysis*, DE, Vol. 47, pp. 453-460.

Derderian, J.M., Howell, L.L., Murphy, M.D., Lyon, S.M., and Pack, S.D., 1996, "Compliant Parallel-Guiding Mechanisms," *Proceedings of the 1996 ASME Mechanisms Conference*, 96-DETC/MECH-1208.

Evans, M.S. and Howell, L.L., 1999, "Constant-Force End-Effector Mechanism," *Proceedings of the IASTED International Conference, Robotics and Applications*, Oct. 28-30, Santa Barbara, CA, USA, pp. 250-256.

Honke, K., Inoue, Y., Hirooka, E., and Sugano, N., 1997, "A Study on the Simulation of Flexible Link Mechanics Based on FEM," *Proceedings of the 1997 ASME Design Engineering Technical Conferences*, DETC97/VIB-4210.

Howell, L.L., Midha, A., and Murphy, M.D, 1994, “Dimensional Synthesis of Compliant Constant-Force Slider Mechanisms,” *Machine Elements and Machine Dynamics*, DE, Vol. 71, pp. 509-515.

Howell, L.L., Midha, A., and Norton, T.W., 1996, “Evaluation of Equivalent Spring Stiffness for Use in a Pseudo-Rigid-Body Model of Large-Deflection Compliant Mechanisms,” *ASME Journal of Mechanical Design*, Vol. 118, pp.126-131.

Howell, L.L., 2001, *Compliant Mechanisms*, John Wiley & Sons, New York.

Jenuwine, J.G., and Midha, A., 1989, “Design of an Exact Constant-Force Generating Mechanism,” *Proceedings of the 1st National Applied Mechanisms & Robotics Conference*, Vol. II, Cincinnati, Ohio, pp. 10B-4-1 - 10B-4-5.

Lyon, S.M., Evans, M.S., Erickson, P.A., and Howell, L.L., 1997, “Dynamic Response of Compliant Mechanisms Using the Pseudo-Rigid-Body Model,” *Proceedings of the 1997 ASME Design Engineering Technical Conferences*, DETC97/VIB-4177.

Megahed, S.M. and Hamza, K.T., 2000, “Modeling of Planar Flexible Link Manipulators: Parameter Identification Using Genetic Algorithm,” *Proceedings of the 2000 ASME Mechanisms Conference*, DETC2000/MECH-14184.

Midha, A., Murphy, M.D., and Howell, L.L., 1995, “Compliant Constant-Force Mechanisms and Devices Formed Therein,” United States Patent No. 5,649,454.

Millar, A.J., Howell, L.L., and Leonard, J.N., 1996, “Design and Evaluation of Compliant Constant-Force Mechanisms,” *Proceedings of the 1996 ASME Mechanisms Conference*, 96-DETC/MECH-1209.

Panza, M.J., 2000, “Mathematical Model for Large Deflection Dynamics of a Compliant Beam Mechanism,” *Proceedings of the 1997 ASME Design Engineering Technical Conferences*, DETC2000/MECH-14146.

Pascal, M. and Gargarina, T., 1999, “Dynamical Simulation of Flexible Multibody System by Using a Rigid Body Model,” *Proceedings of DETC 99 ASME Design Engineering Technical Conferences*, September 12-15, Las Vegas, Nevada, DETC99/VIB-8230.

Petroka, R.P., and Chang, L., 1989, "Experimental Validation of a Dynamic Model (Equivalent Rigid Link System) on a Single-Link Flexible Manipulator," *Journal of Dynamic Systems, Measurement, and Control*, Vol. 111, pp. 667-672.

Sevak, N.M., and McLarnan, C.W., 1974, "Optimal Synthesis of Flexible Link Mechanisms with Large Static Deflections," ASME Paper No. 74-DET-83.

Simo, J.C., and Posbergh, T.A., 1988, "Nonlinear Dynamics of Flexible Structures: Geometrically Exact Formulation and Stability," *Proceeding of the 27th Conference on Decision and Control*, IEEE FA2-12:15, pp. 1732-1737.

Sugano, N., Honke, K., Imanishi, E., and Hashimoto, K., 1999, "A Study on the Dynamic Analysis of Flexible and Rigid Link System," *Proceedings of the 1997 ASME Design Engineering Technical Conferences*, DETC99/VIB-8247.

Thomson, W.T., and Dahleh, M.D., 1998, *Theory of Vibration with Applications*, 5th edition, Prentice Hall, Upper Saddle River, New Jersey.

Vogel, S., 1995, "Better Bent than Broken," *Discover*, May 1995, pp. 62-67.

Wang, Y., 1997, "Dynamics of an Elastic Four Bar Linkage Mechanism with Geometric Nonlinearities," *Nonlinear Dynamics*, Vol. 14, pp. 357-375.

Yen, C. and Masada, G.Y., 1994, "Dynamic Analysis of Flexible Bodies Using Extended Bond Graphs," *Journal of Dynamic Systems, Measurement, and Control*, Vol. 116, No. 1, pp. 66-72.

Zakhariev, E.V., 1999, "Nonlinear Dynamics of Rigid and Flexible Multibody Systems," *Proceedings of the 1999 ASME Design Engineering Technical Conferences*, DETC99/VIB-8248.

APPENDIX A Pseudo-Rigid-Body Model

The pseudo-rigid-body model is a design tool that approximates the force-deflection relationships of compliant mechanisms by assigning a rigid-body, lumped compliance counterpart to every flexible segment comprising the mechanism. Its broad assumptions adhere to the actual kinematics of many compliant mechanisms. What makes it so useful is its ability to transform a compliant mechanism requiring in-depth nonlinear analysis to understand into an “equivalent” rigid-body mechanism, for which well-known rigid-body kinematics techniques are already in place.

Two pseudo-rigid-body model rules are required for the design of compliant constant-force mechanisms: the rule for a small-length flexural pivot, and the rule for a cantilever beam with a force at the free end. Several other rules have been developed for the treatment of mechanisms comprised of flexible segments, but only these two are presented here. Even so, they are presented in their simplest form (the form used in this research). For a more thorough treatment of the pseudo-rigid-body model, refer to Howell (2001).

For the following, assume that each flexible segment has constant cross section, is rigid in shear, has homogeneous material properties, and operates in the elastic range (Howell, 2001).

A.1 Small-Length Flexural Pivot

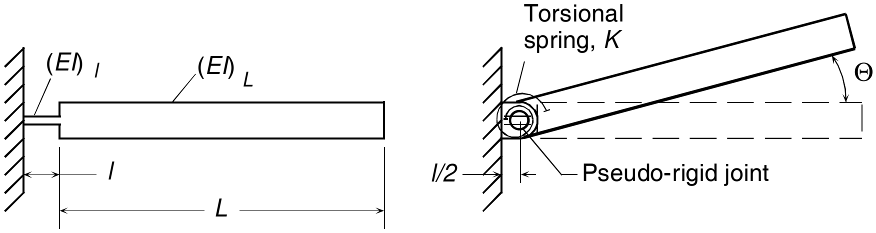

A small-length flexural pivot is defined as a flexible segment that is small in length compared to the rigid segment it is attached to, i.e. $l \ll L$ and $(EI)_l \ll (EI)_L$. The flexible segment is approximated by two rigid segments, each replacing half of the flexible segment. The left rigid segment becomes a rigid extension of ground, and the right rigid segment becomes an extension of the long rigid segment of length L. A "characteristic pivot" positioned at the center of the flexible beam joins the two, and a torsional spring at the pivot represents the flexible segment's compliance. The pseudo-rigid-body angle Θ is equal to the angle of the compliant mechanism's rigid segment. The torsional spring is $K = \frac{EI}{l}$, where I and E are the moment of inertia of the cross section and the modulus of elasticity of the flexible segment.

A.2 Cantilever Beam with a Force at the Free End

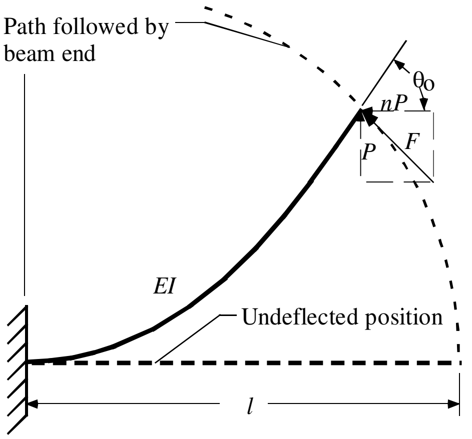

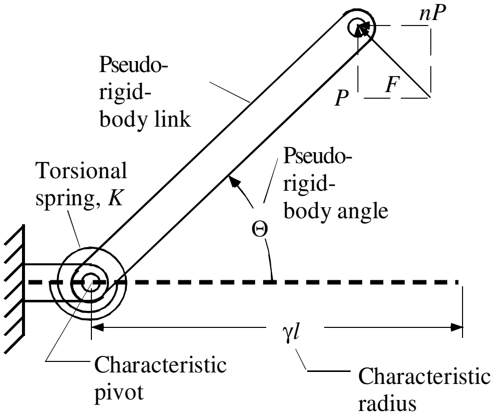

When a cantilever beam undergoes large deflection due to a force *F* at the free end, where the angle of *F* is described by the ratio of horizontal to vertical components (*n*), the tip of the beam traces out a nearly circular arc. The pseudo-rigid-body model for this compliant mechanism places the characteristic pivot approximately at the center of this arc. The value of the characteristic radius is proportional to the characteristic radius factor γ. Though γ can be represented as a function of *n*, for simplicity most pseudo-rigid-body calculations use $\gamma_{avg} = 0.85$. The torsional spring is given by $K = \gamma K_{\Theta}\frac{EI}{l}$, where *I* and *E* are the moment of inertia of the cross section and the modulus of elasticity of the flexible segment. The stiffness coefficient K_{Θ} is also a function of *n*, but again for simplicity the value $K_{\Theta} \cong 2.65$ is usually chosen.

The relationship between the pseudo-rigid-body angle Θ and the actual beam end angle θ_0 is nearly linear, and is approximated by $\theta_0 = c_{\theta}\Theta$, where $c_{\theta} \cong 1.24$.

APPENDIX B Dynamic Data

This appendix contains plots of the measured force and the force predicted by the dynamic model of Chapter 3, *Dynamic Model*, and Chapter 6, *Generalized Dynamic Model*, for all five of the constant-force mechanisms tested in this thesis. Mechanism parameters can be found in Tables 4.1 and 7.1. Data is given in five sets, in the following order: mechanism Class 1A-d I, Class 1A-d II, Class 1A-d III, Class 1B-g I, and Class 1B-g II, according to the naming scheme laid out in Chapter 7.

Proceeding each data set is a position plot representing the sinusoidal input x_b to the mechanism. Immediately following are plots of force output for increasing frequencies. Only the position plot coinciding with the first frequency is given because the position input to each force plot is identical aside from its frequency, which is labeled at the top of each force plot.

For each force plot, the predicted force cycle is calculated directly from the input sinusoid cycle x_b. The measured force cycle in each figure is the result of force data processed as described in Section 4.3.1 *Dynamic Data Processing* on page 40. The measured data is banded by ±3 pooled sample standard deviations, or $\pm 3\,\sigma$, representing the 99.74% confidence interval of the measurement.

Static test data for the mechanisms is given in APPENDIX D.

B.1 Mechanism Class 1A-d I

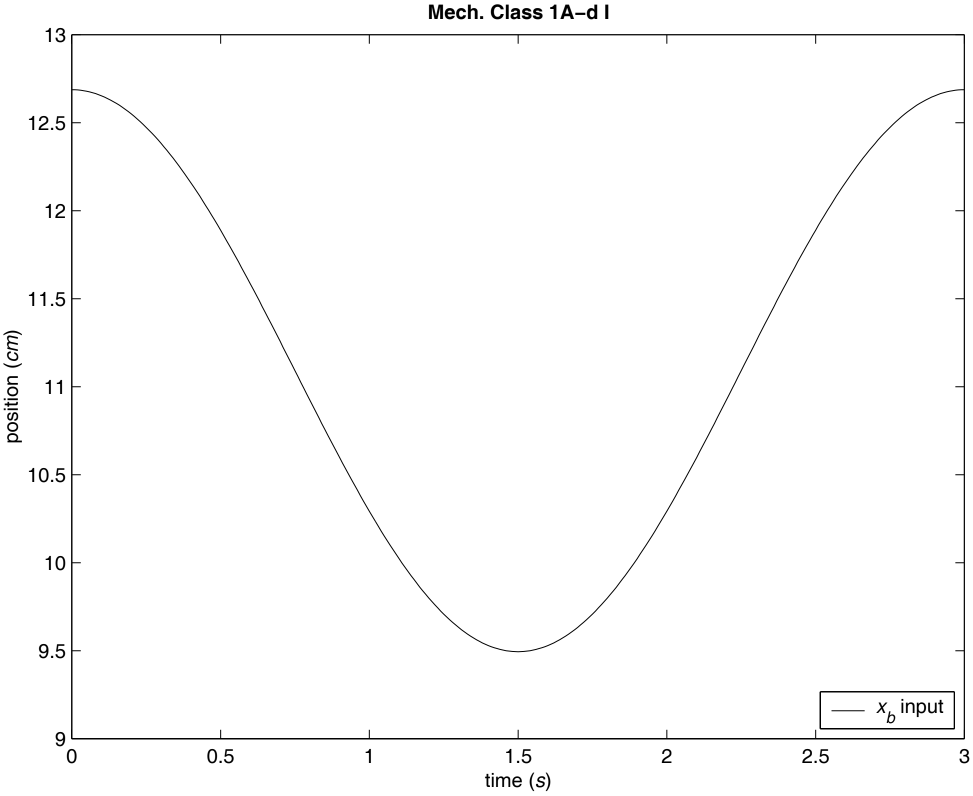
Mech. Class 1A–d I

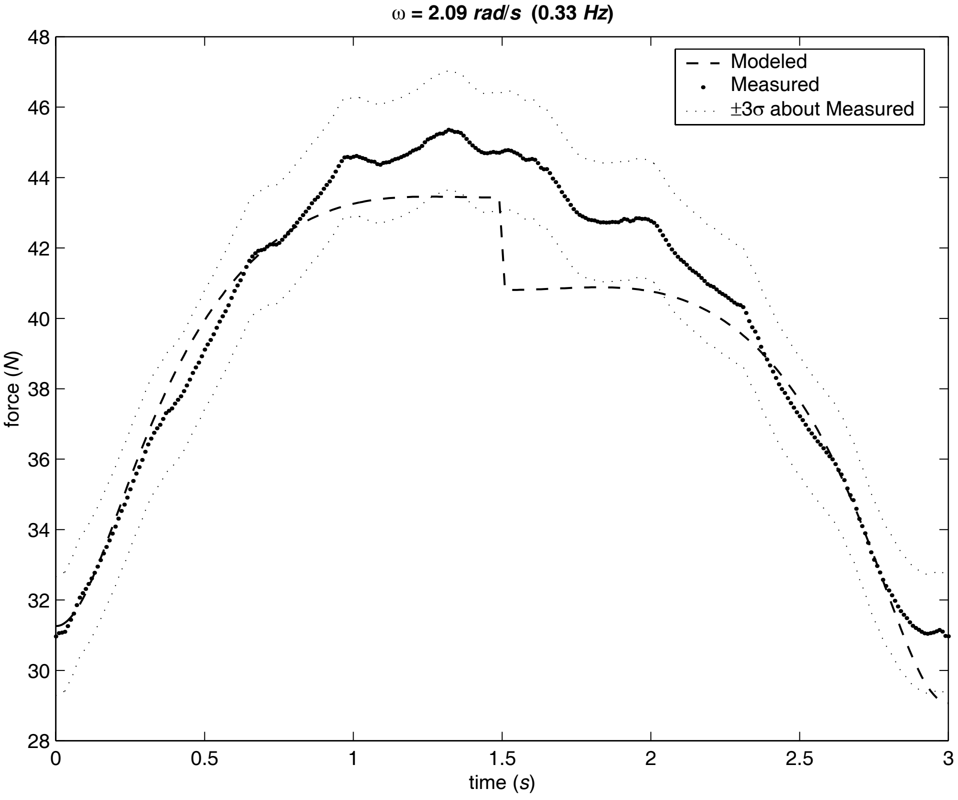
ω = 2.09 rad/s (0.33 Hz)

B.1 MECHANISM CLASS 1A-D I (CONTINUED)

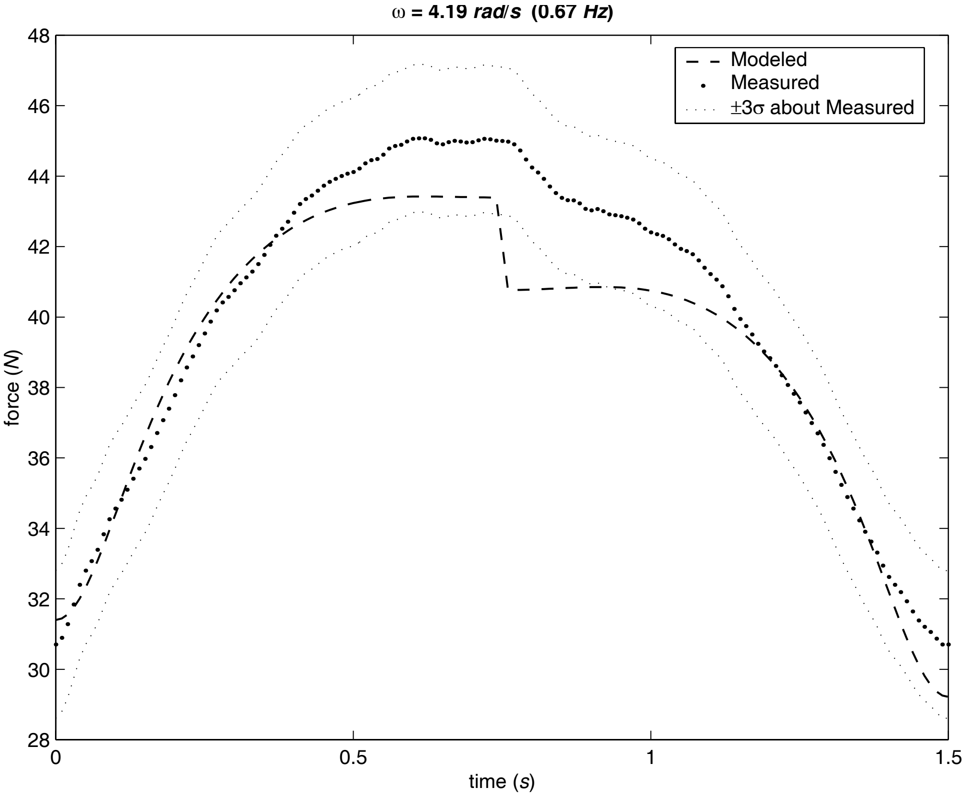

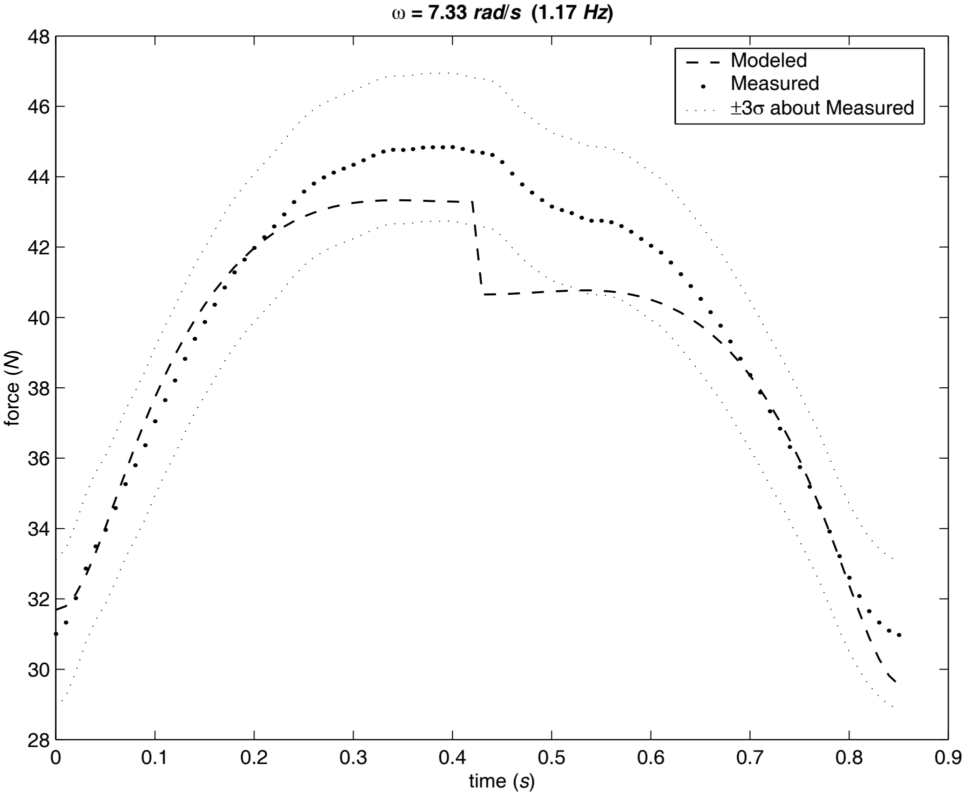

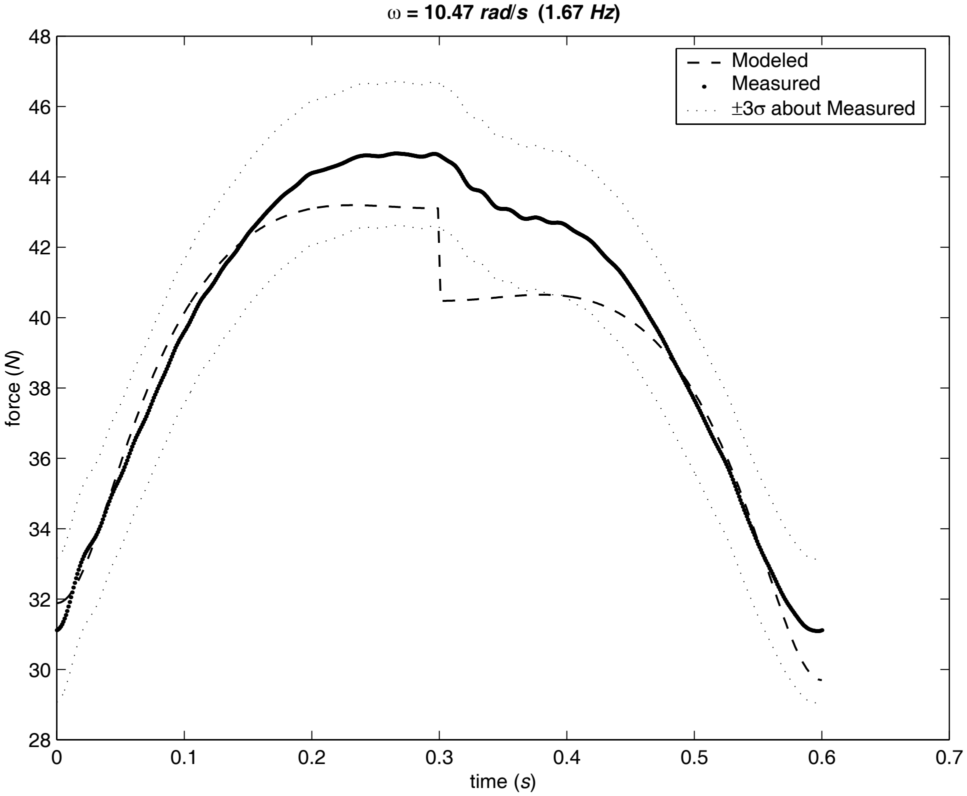
ω = 10.47 rad/s (1.67 Hz)
Modeled
Measured
±3σ about Measured
force (N)
time (s)
48
46
44
42
40
38
36
34
32
30
28
0
0.1
0.2
0.3
0.4
0.5
0.6
0.7

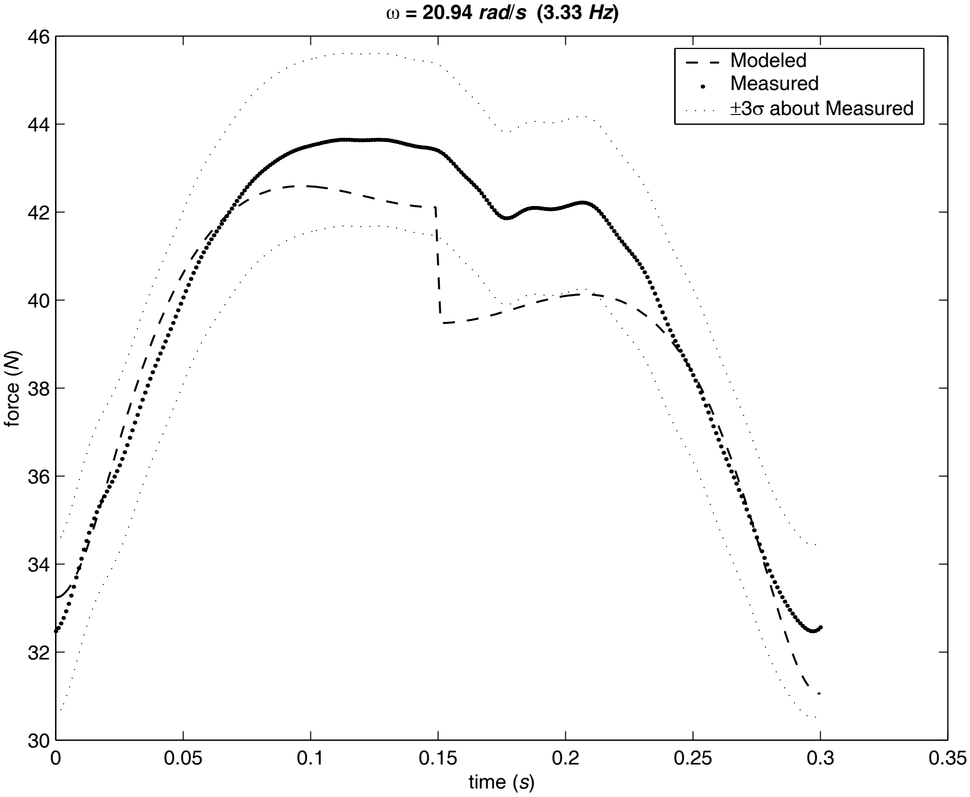
ω = 20.94 rad/s (3.33 Hz)
Modeled
Measured
±3σ about Measured
force (N)
time (s)
46
44
42
40
38
36
34
32
30
0
0.05
0.1
0.15
0.2
0.25
0.3
0.35

ω = 31.42 *rad/s* (5.00 *Hz*)

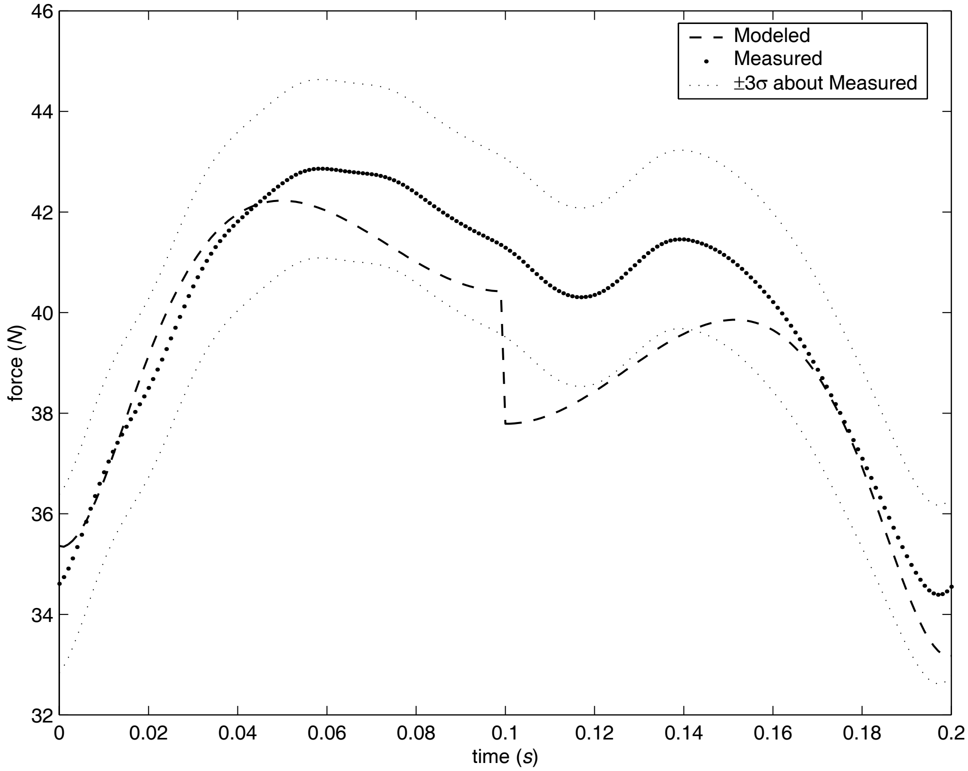

ω = 41.89 *rad/s* (6.67 *Hz*)

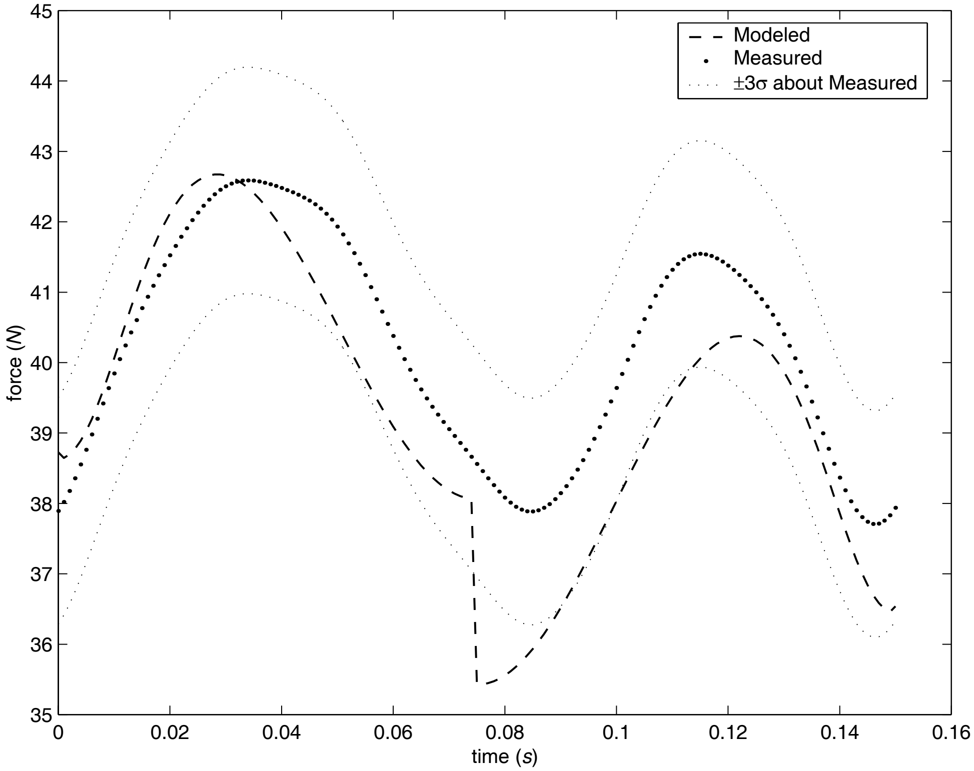

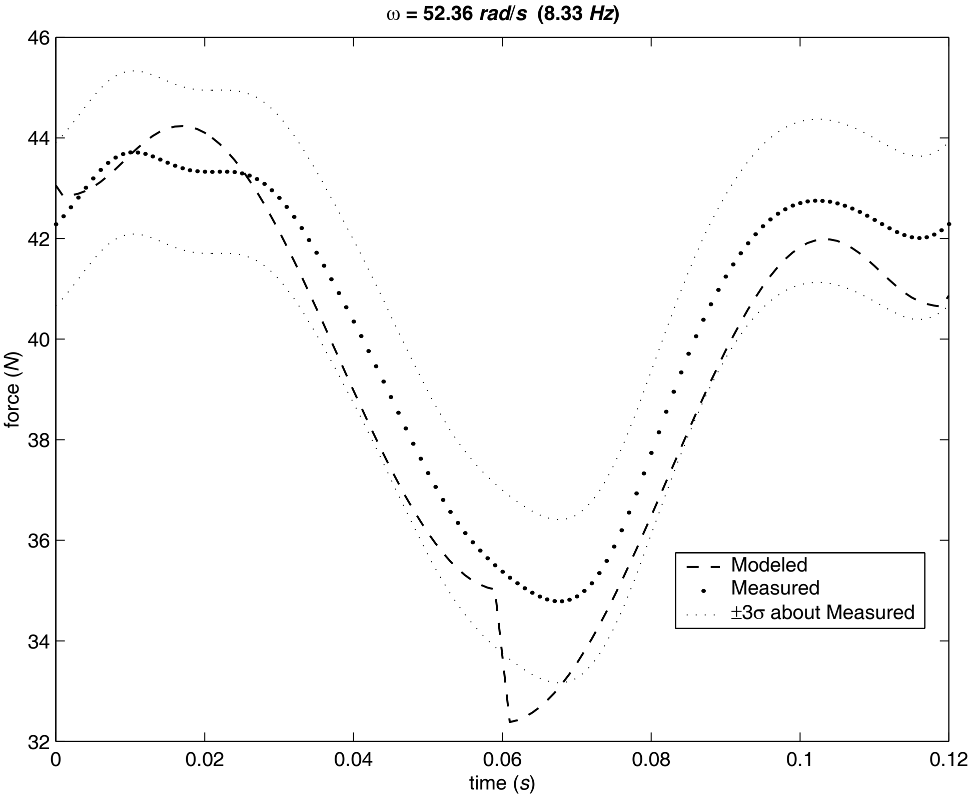
ω = 52.36 *rad/s* (8.33 *Hz*)
force (*N*)
time (*s*)
46
44
42
40
38
36
34
32
0
0.02
0.04
0.06
0.08
0.1
0.12
Modeled
Measured
±3σ about Measured

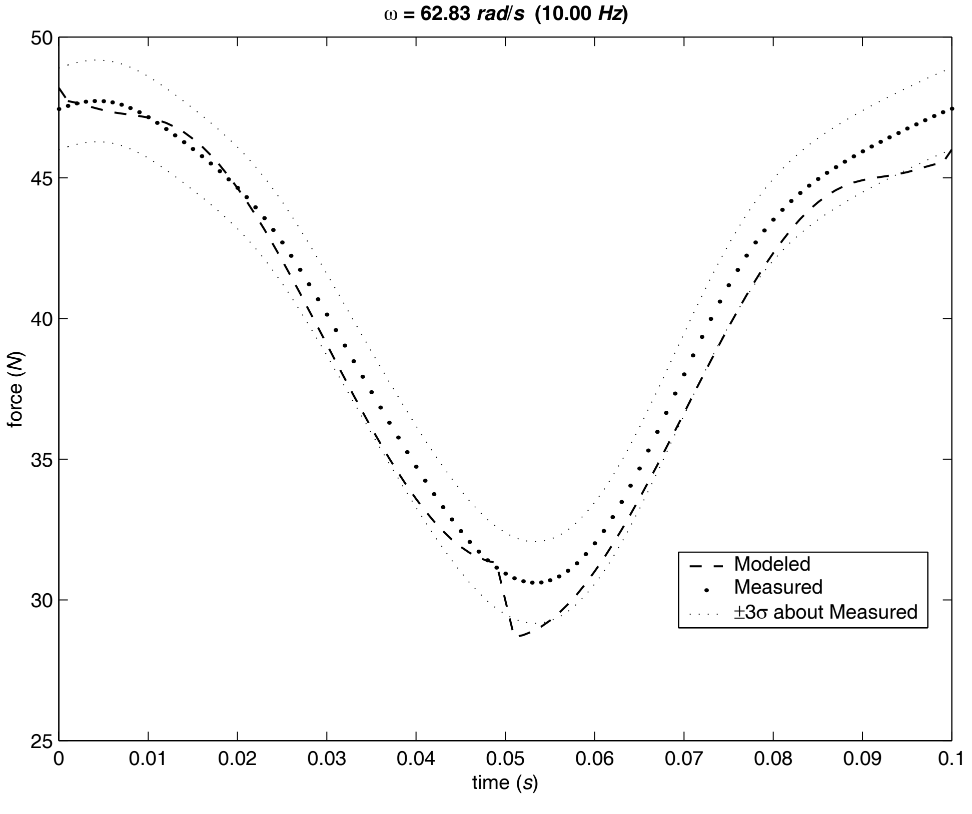
ω = 62.83 *rad/s* (10.00 *Hz*)
force (*N*)
time (*s*)
50
45
40
35
30
25
0
0.01
0.02
0.03
0.04
0.05
0.06
0.07
0.08
0.09
0.1
Modeled
Measured
±3σ about Measured

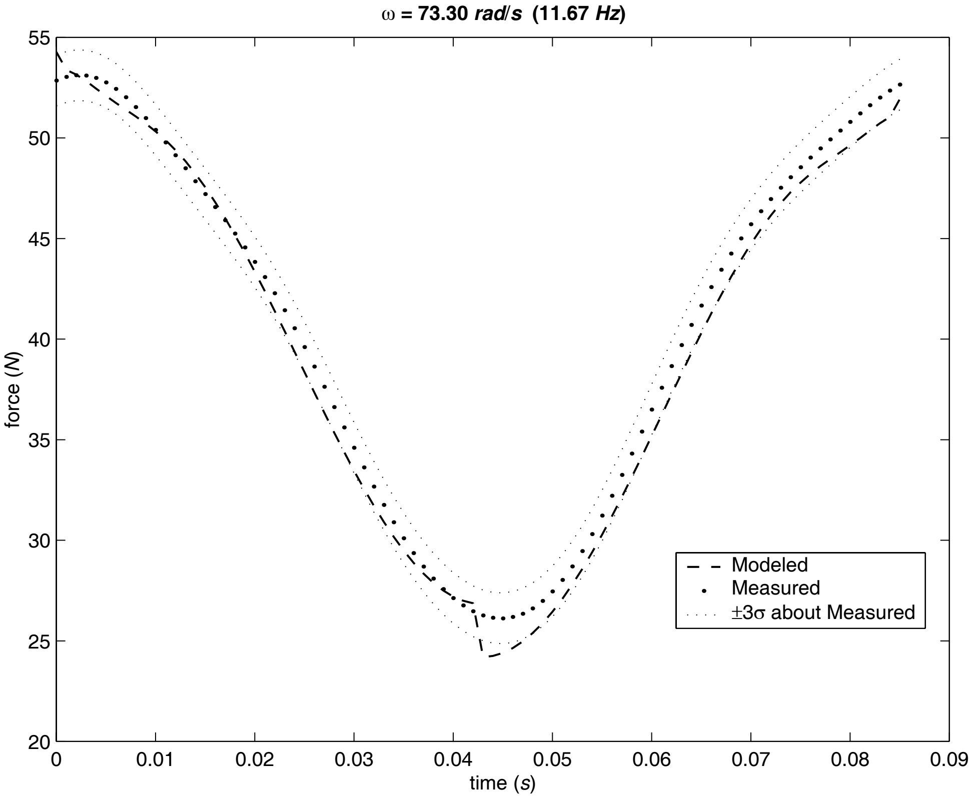
ω = 73.30 rad/s (11.67 Hz)
force (N)
time (s)
55
50
45
40
35
30
25
20
0
0.01
0.02
0.03
0.04
0.05
0.06
0.07
0.08
0.09
Modeled
Measured
±3σ about Measured

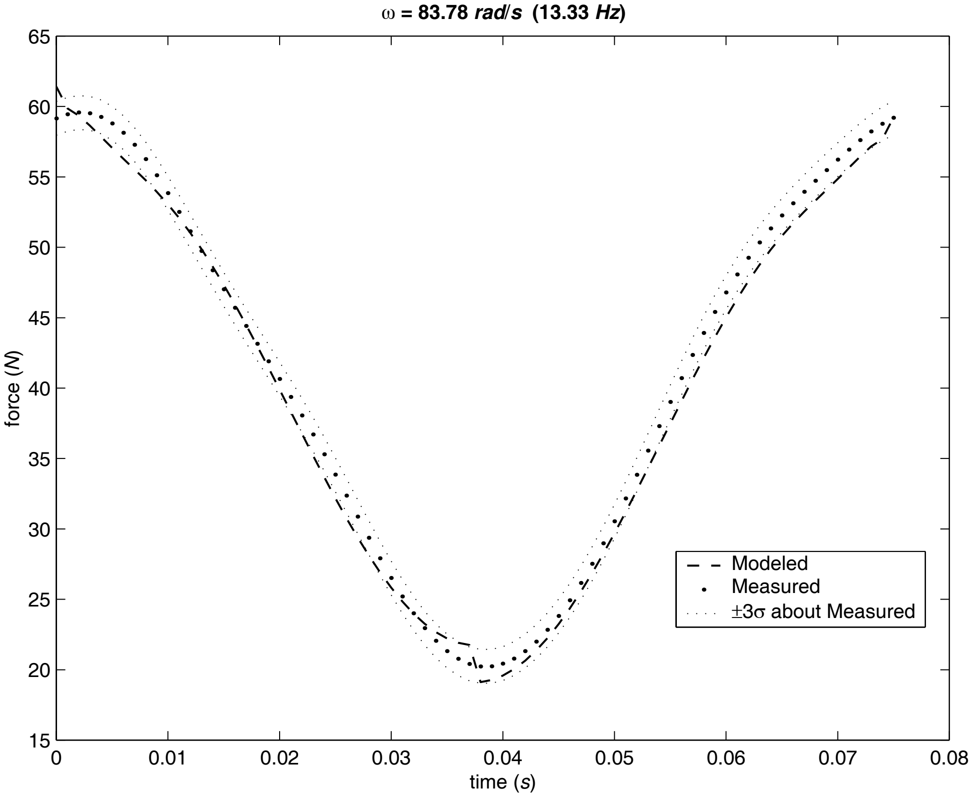
ω = 83.78 rad/s (13.33 Hz)
force (N)
time (s)
65
60
55
50
45
40
35
30
25
20
15
0
0.01
0.02
0.03
0.04
0.05
0.06
0.07
0.08
Modeled
Measured
±3σ about Measured

B.1 MECHANISM CLASS 1A-D I (CONTINUED)

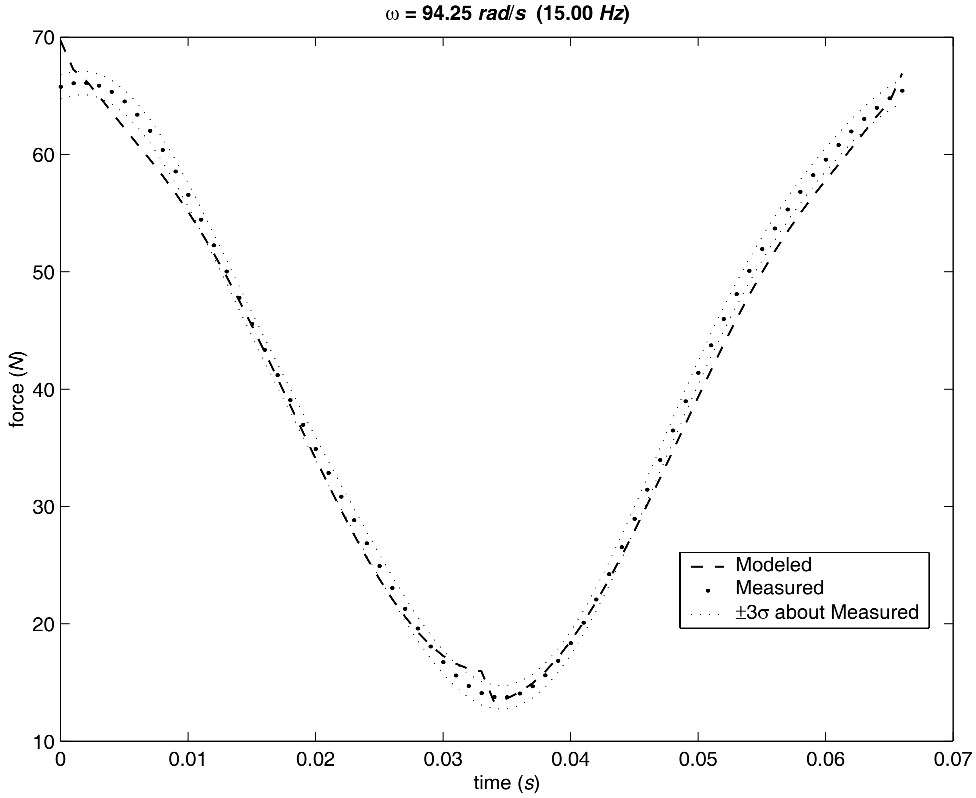

B.2 Mechanism Class 1A-d II

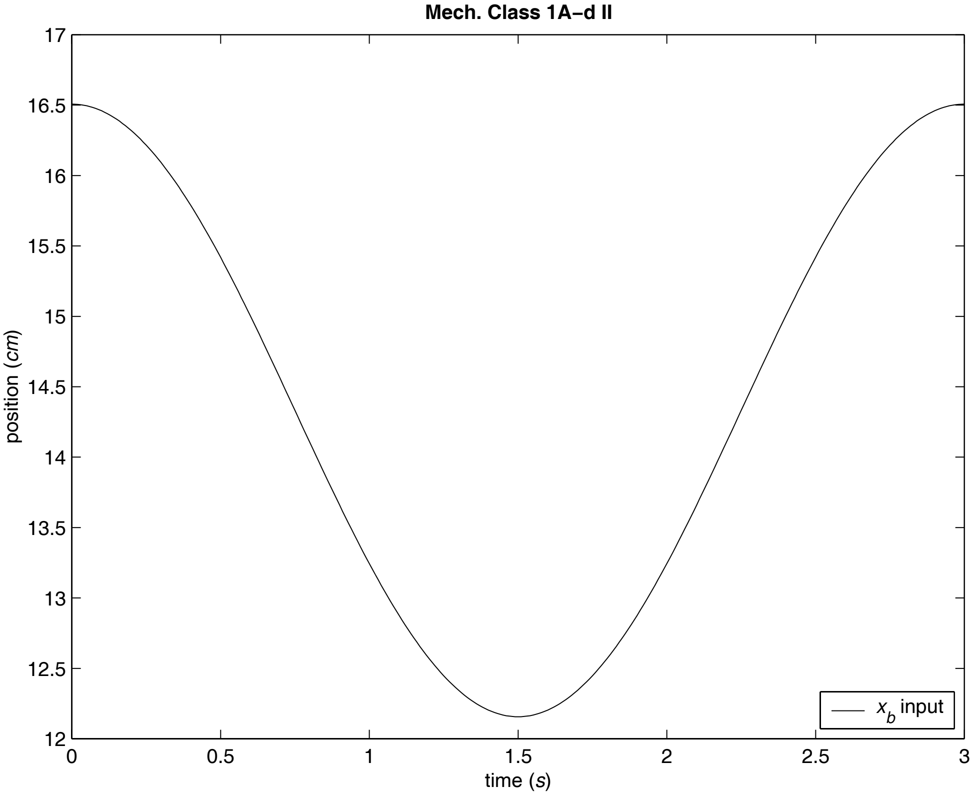

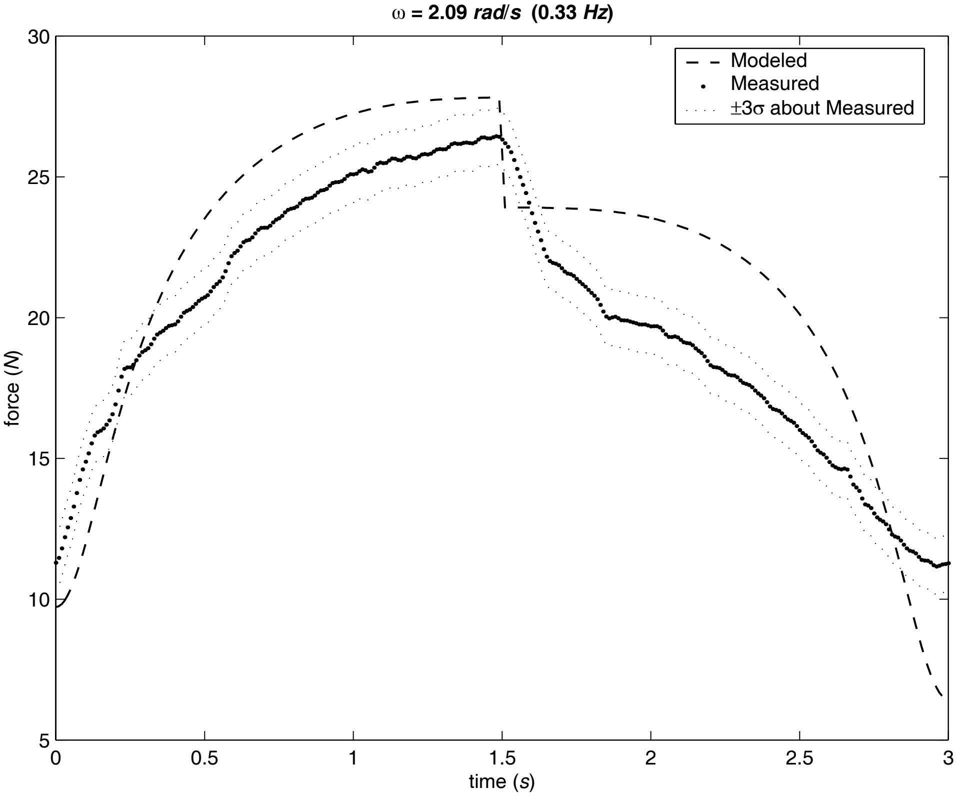

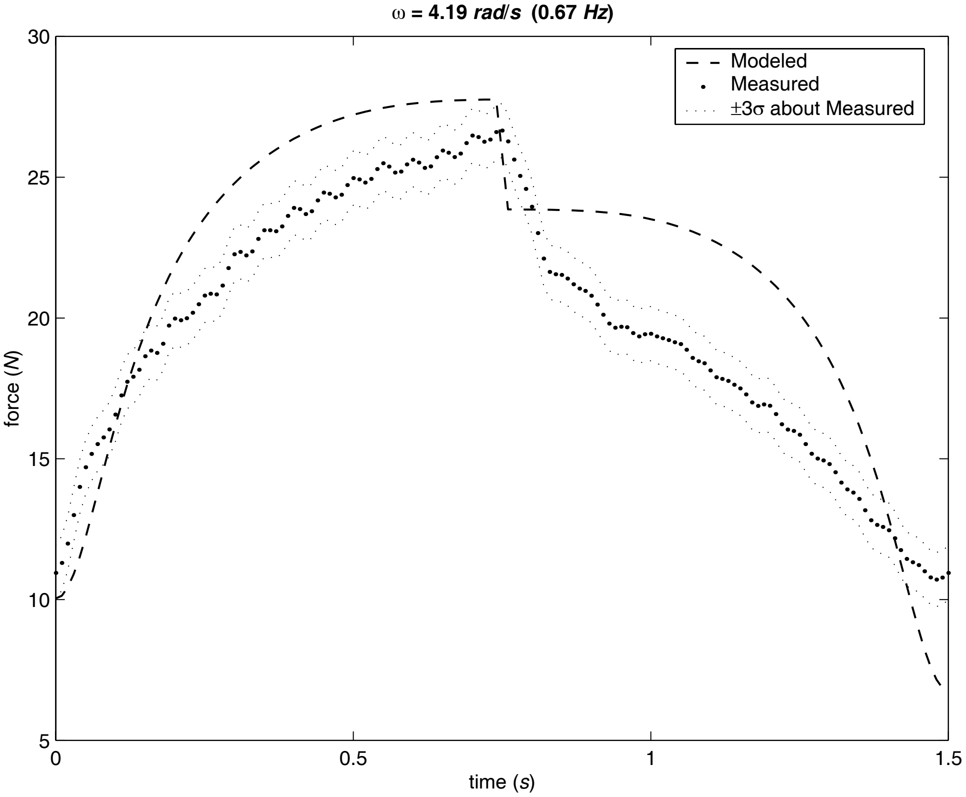
ω = 4.19 *rad/s* (0.67 *Hz*)
Modeled
Measured
±3σ about Measured
force (*N*)
time (*s*)
30
25
20
15
10
5
0
0.5
1
1.5

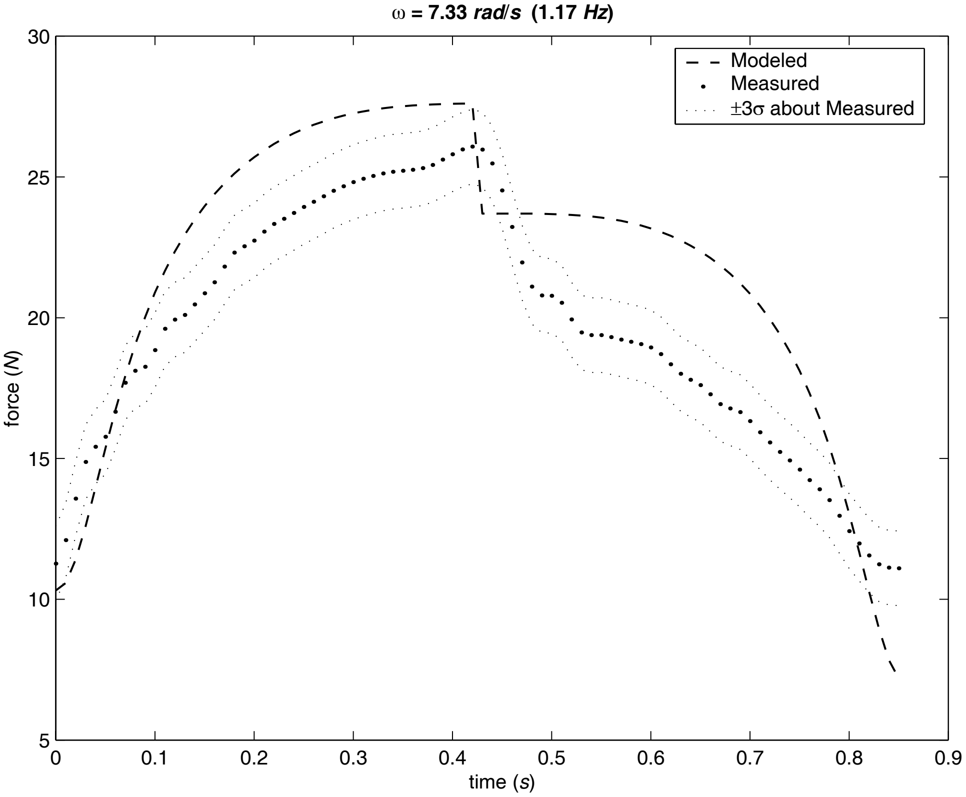
ω = 7.33 *rad/s* (1.17 *Hz*)
Modeled
Measured
±3σ about Measured
force (*N*)
time (*s*)
30
25
20
15
10
5
0
0.1
0.2
0.3
0.4
0.5
0.6
0.7
0.8
0.9

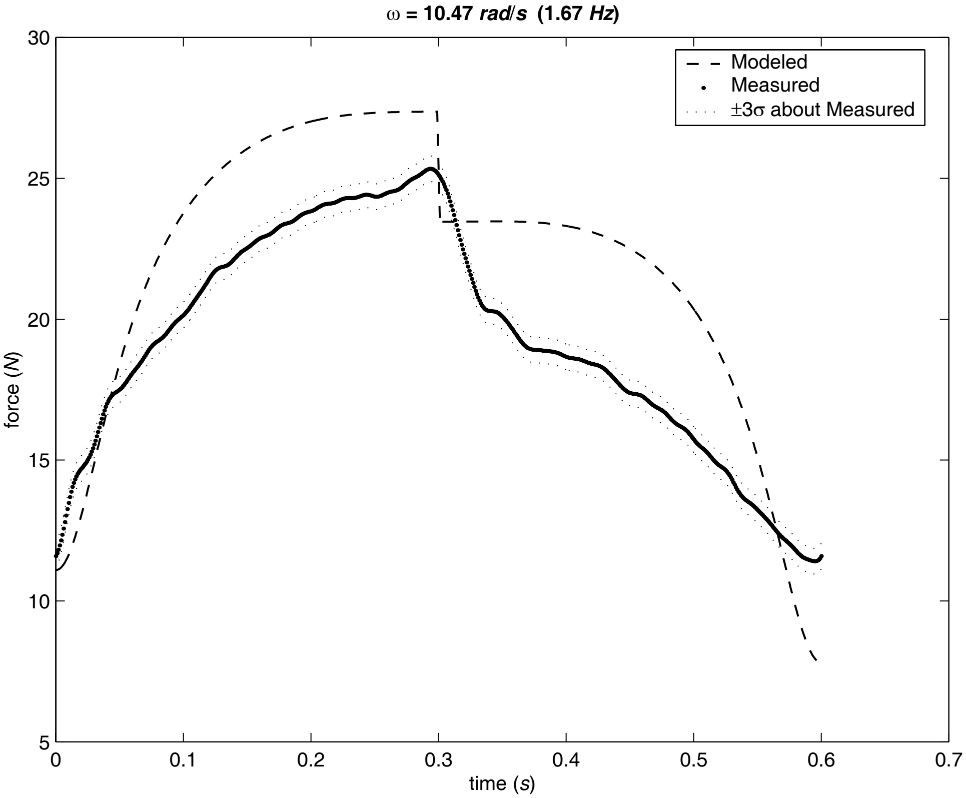
ω = 10.47 *rad/s* (1.67 *Hz*)
Modeled
Measured
±3σ about Measured
force (*N*)
time (*s*)
30
25
20
15
10
5
0
0.1
0.2
0.3
0.4
0.5
0.6
0.7

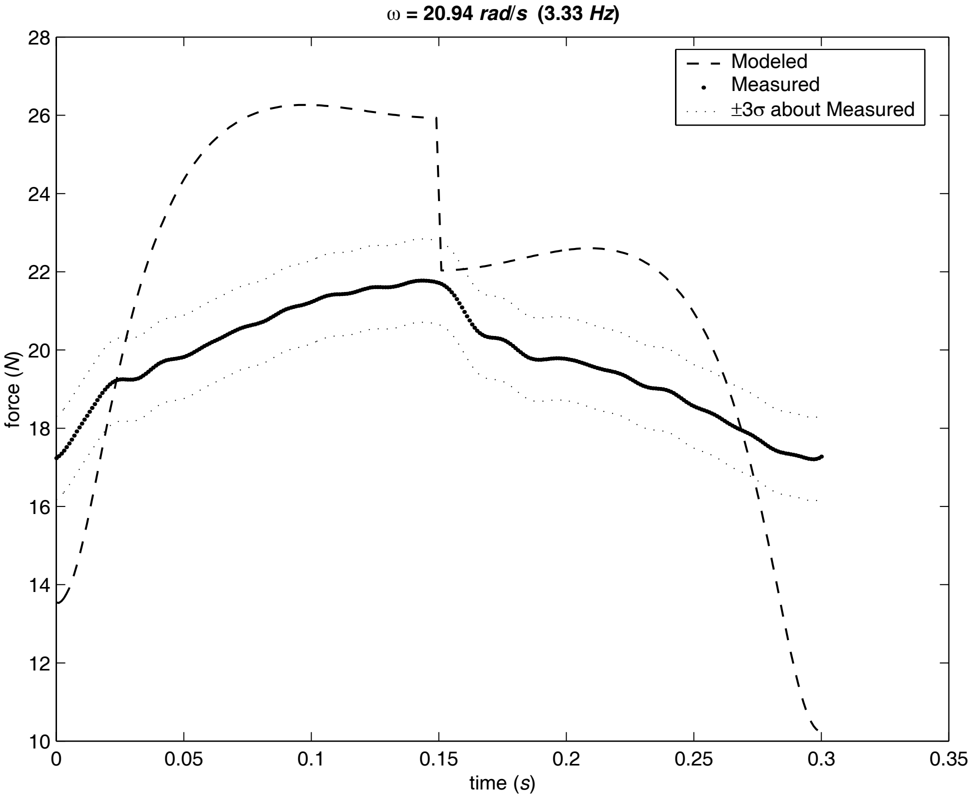
ω = 20.94 *rad/s* (3.33 *Hz*)
Modeled
Measured
±3σ about Measured
force (*N*)
time (*s*)
28
26
24
22
20
18
16
14
12
10
0
0.05
0.1
0.15
0.2
0.25
0.3
0.35

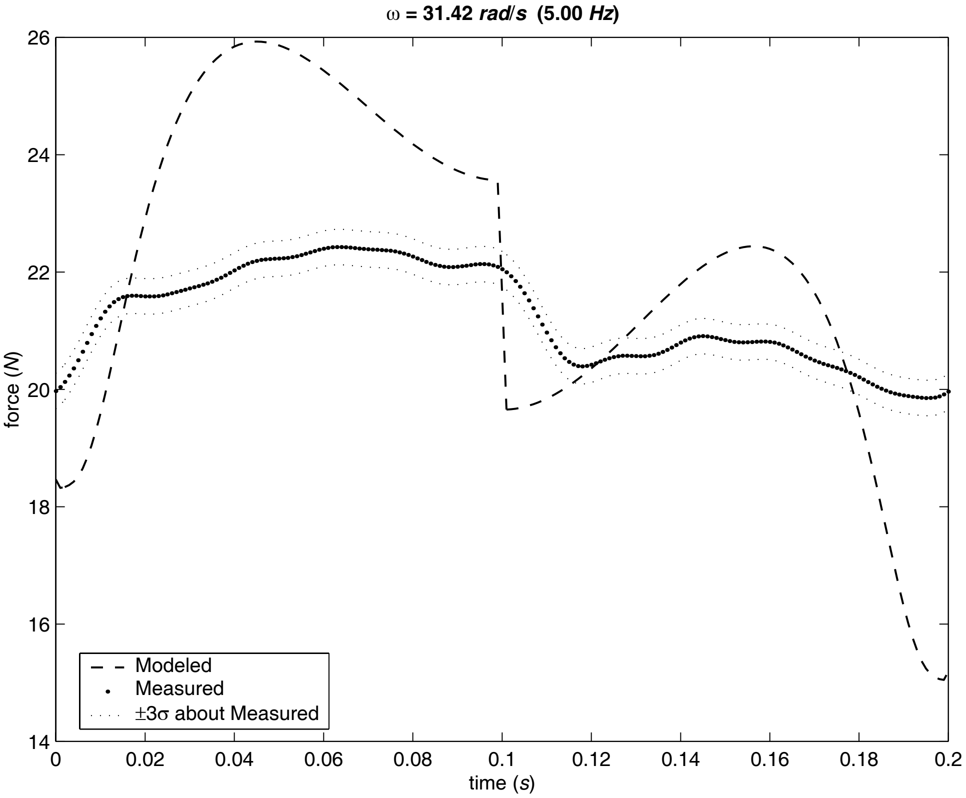
ω = 31.42 rad/s (5.00 Hz)
force (N)
time (s)
Modeled
Measured
±3σ about Measured
26
24
22
20
18
16
14
0
0.02
0.04
0.06
0.08
0.1
0.12
0.14
0.16
0.18
0.2

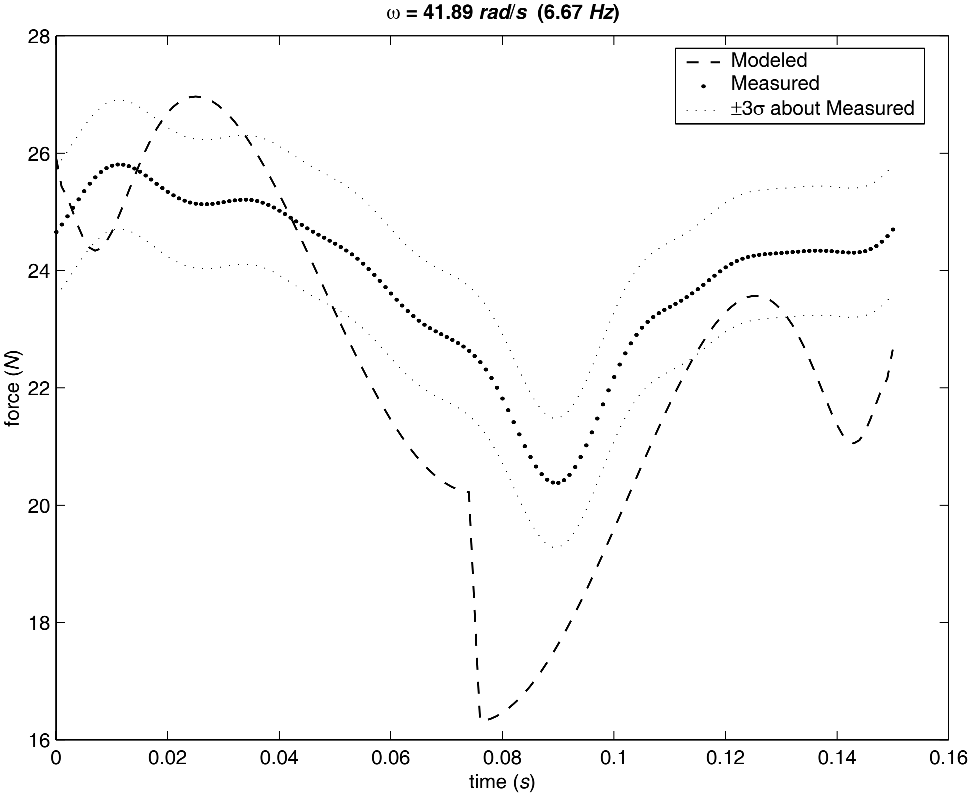
ω = 41.89 rad/s (6.67 Hz)
force (N)
time (s)
Modeled
Measured
±3σ about Measured
28
26
24
22
20
18
16
0
0.02
0.04
0.06
0.08
0.1
0.12
0.14
0.16

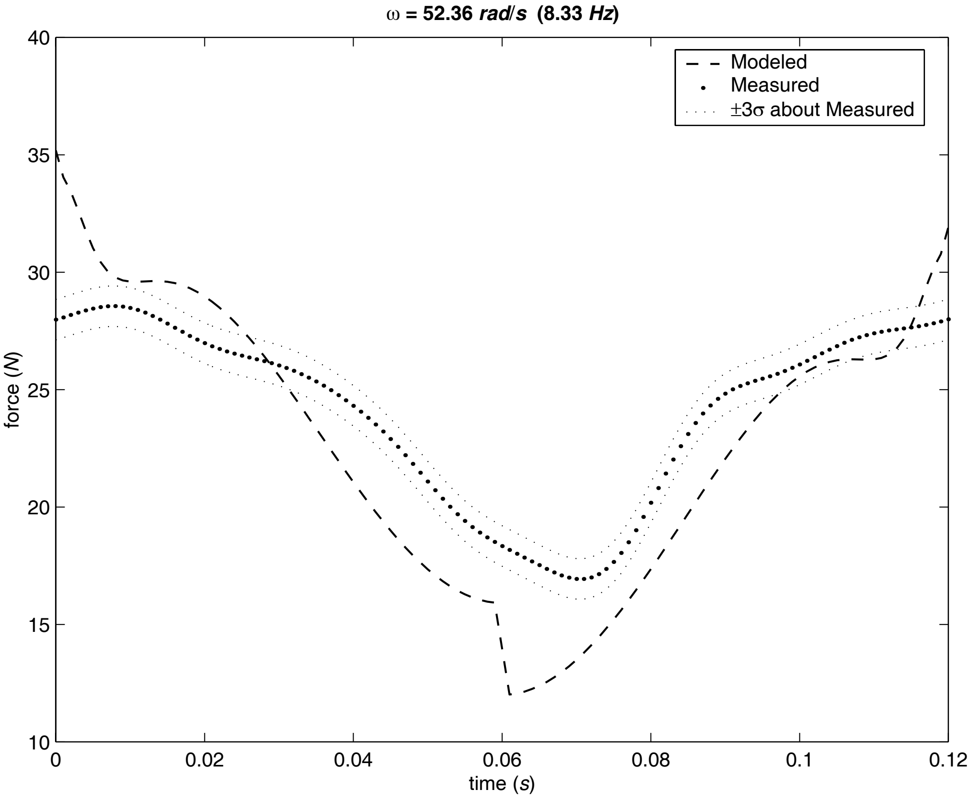
ω = 52.36 *rad/s* (8.33 *Hz*)
Modeled
Measured
±3σ about Measured
force (*N*)
time (*s*)
10
15
20
25
30
35
40
0
0.02
0.04
0.06
0.08
0.1
0.12

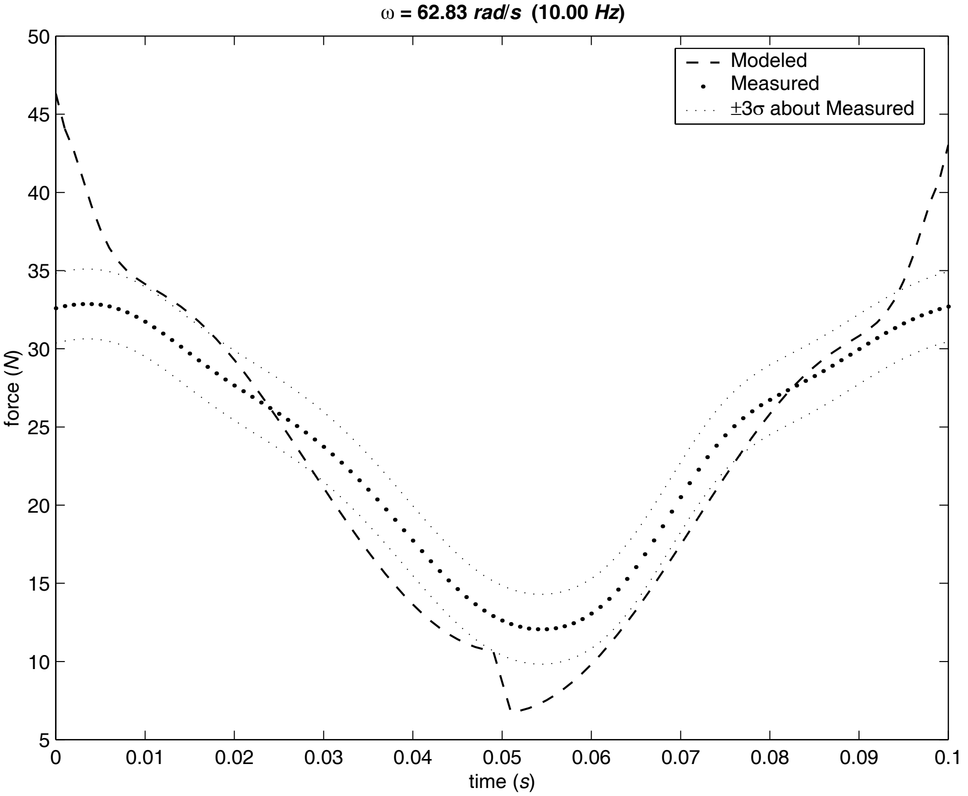
ω = 62.83 *rad/s* (10.00 *Hz*)
Modeled
Measured
±3σ about Measured
force (*N*)
time (*s*)
5
10
15
20
25
30
35
40
45
50
0
0.01
0.02
0.03
0.04
0.05
0.06
0.07
0.08
0.09
0.1

B.3 Mechanism Class 1A-d III

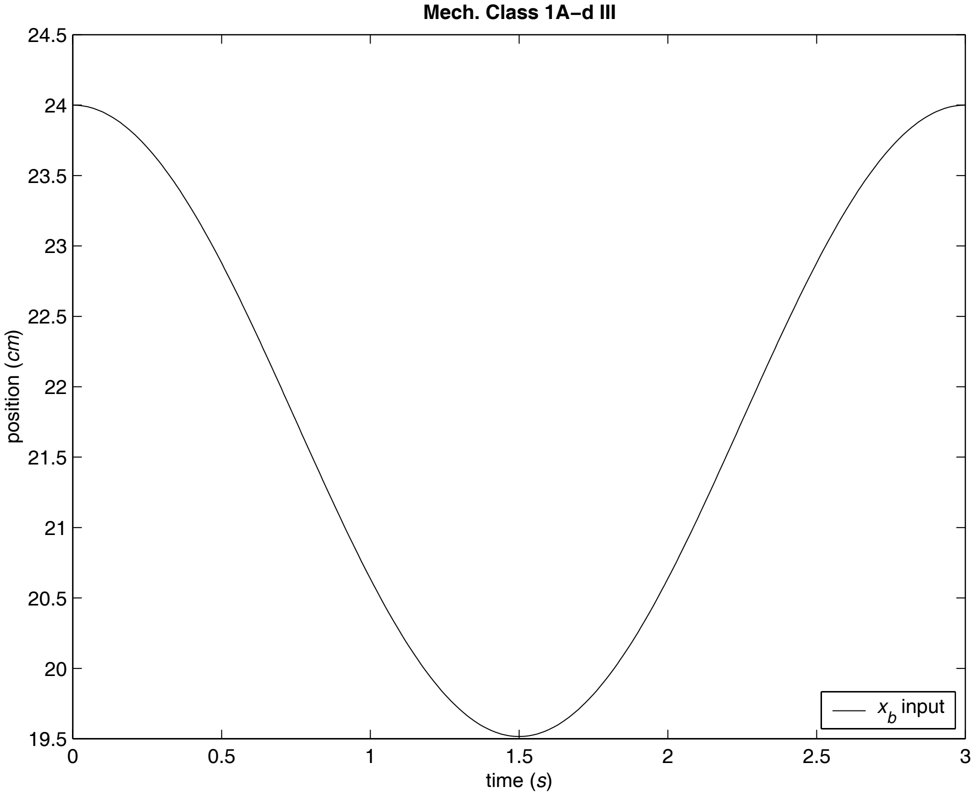

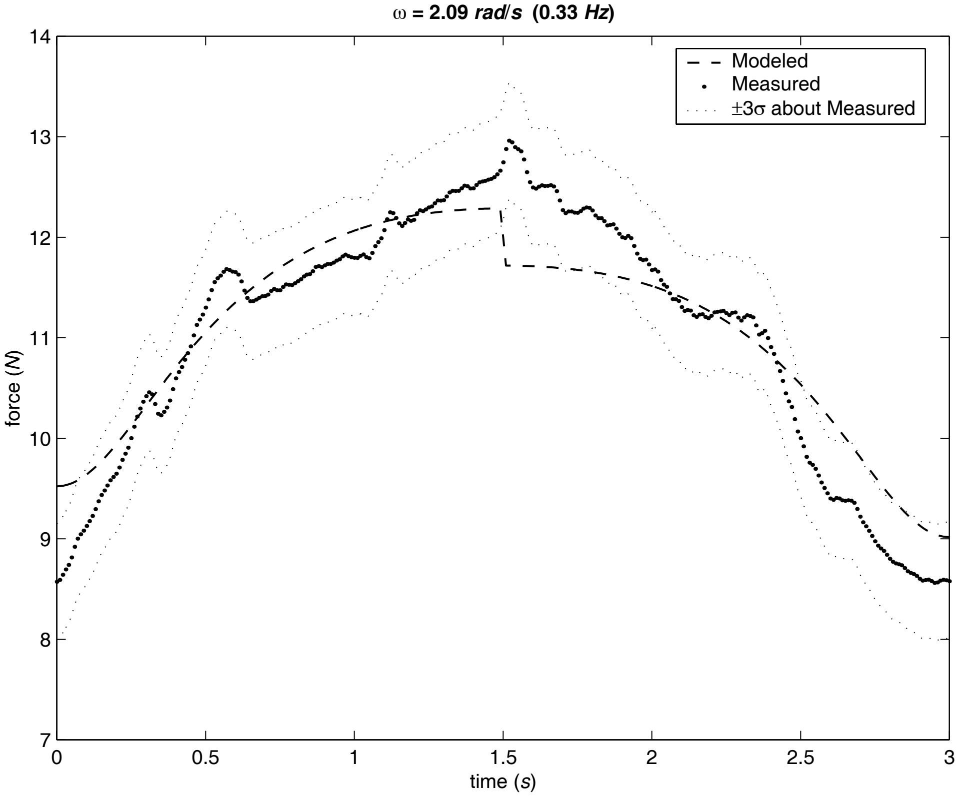

B.3 MECHANISM CLASS 1A-D III (CONTINUED)

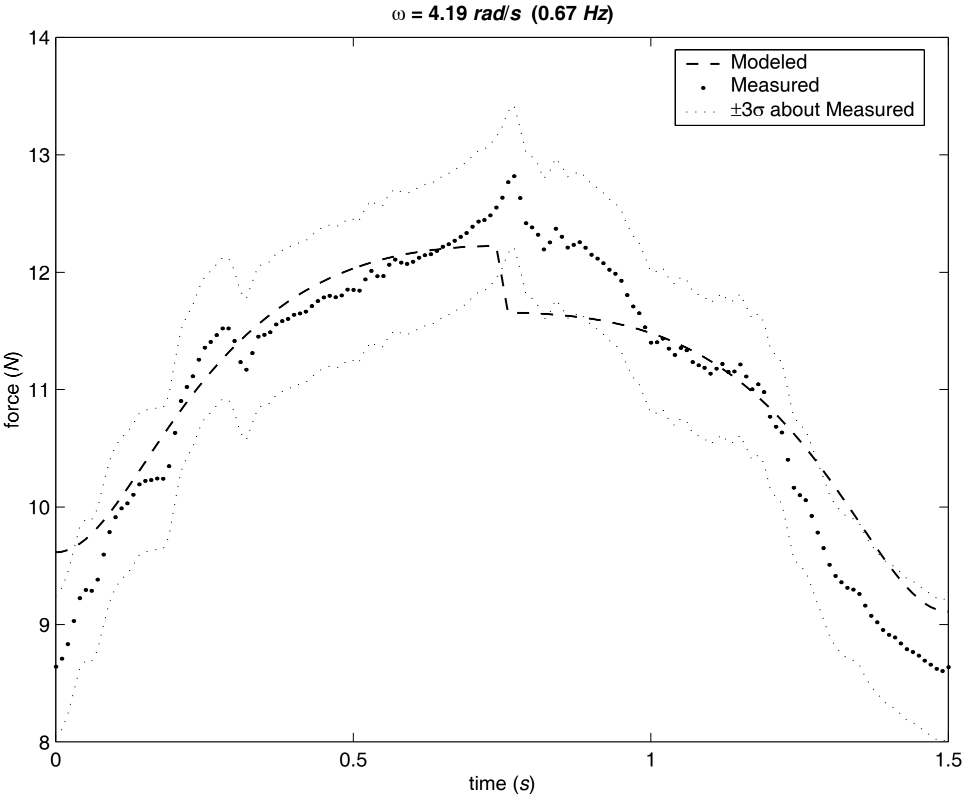
ω = 4.19 *rad/s* (0.67 *Hz*)

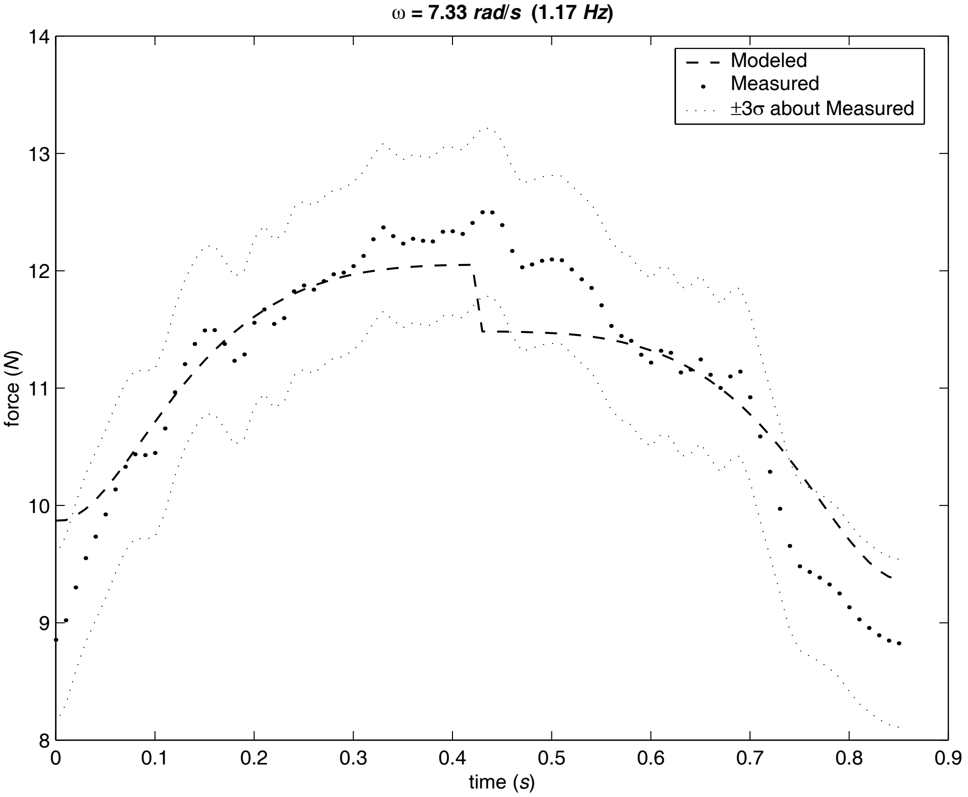
ω = 7.33 *rad/s* (1.17 *Hz*)

B.3 MECHANISM CLASS 1A-D III (CONTINUED)

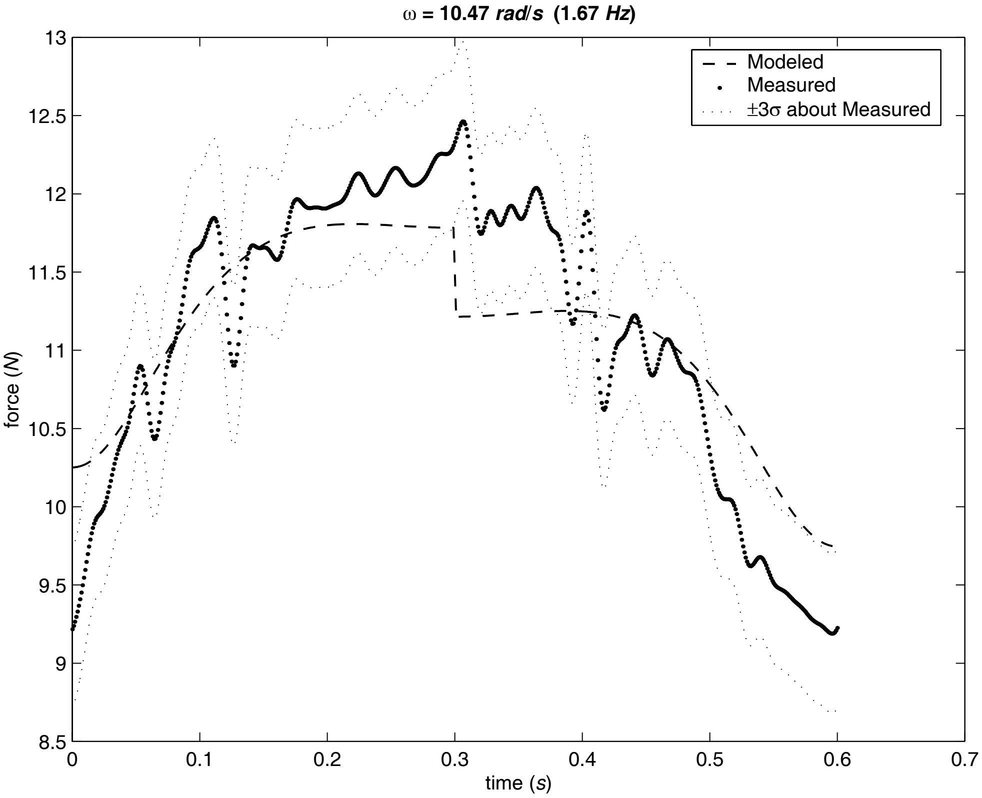

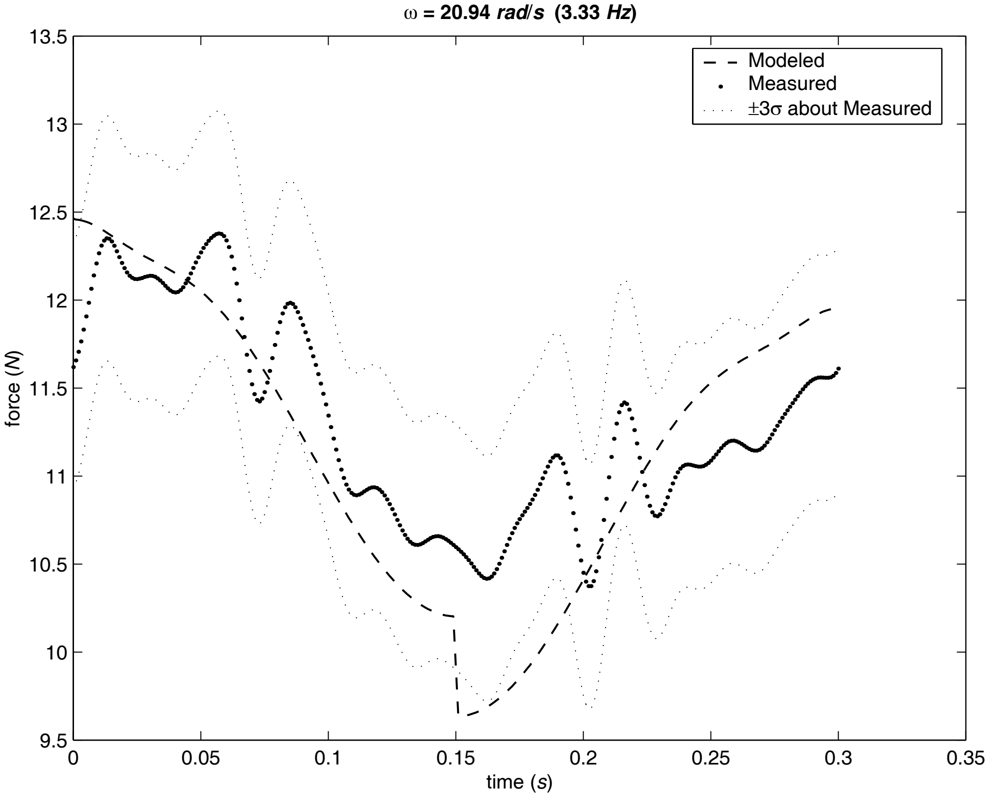

B.3 MECHANISM CLASS 1A-D III (CONTINUED)

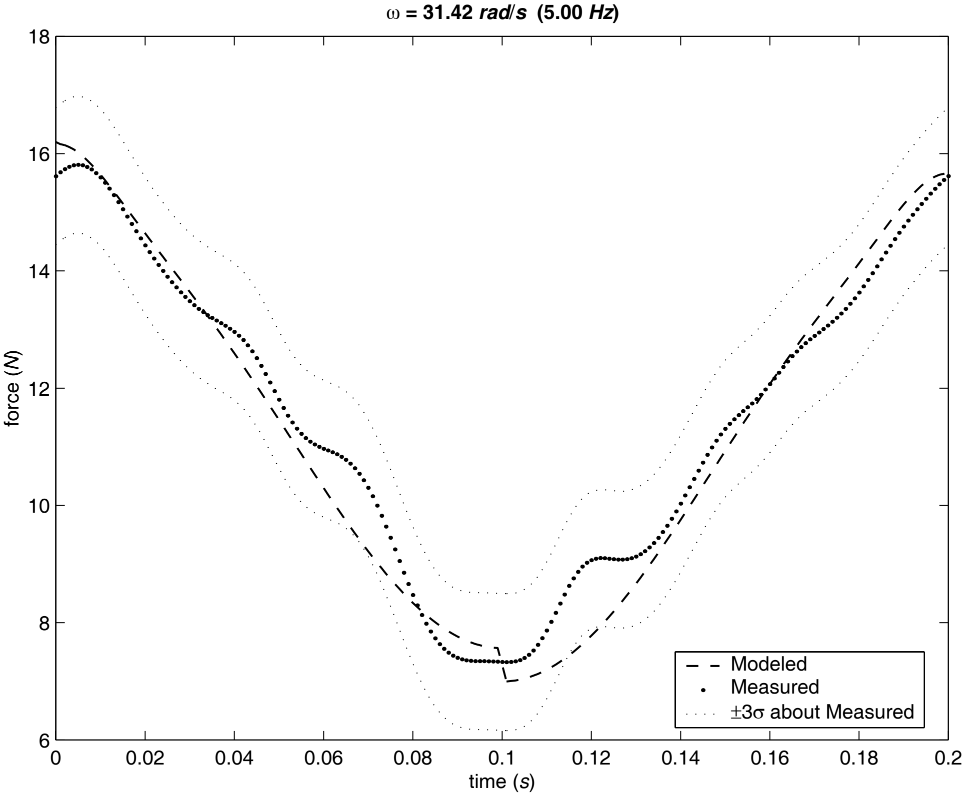

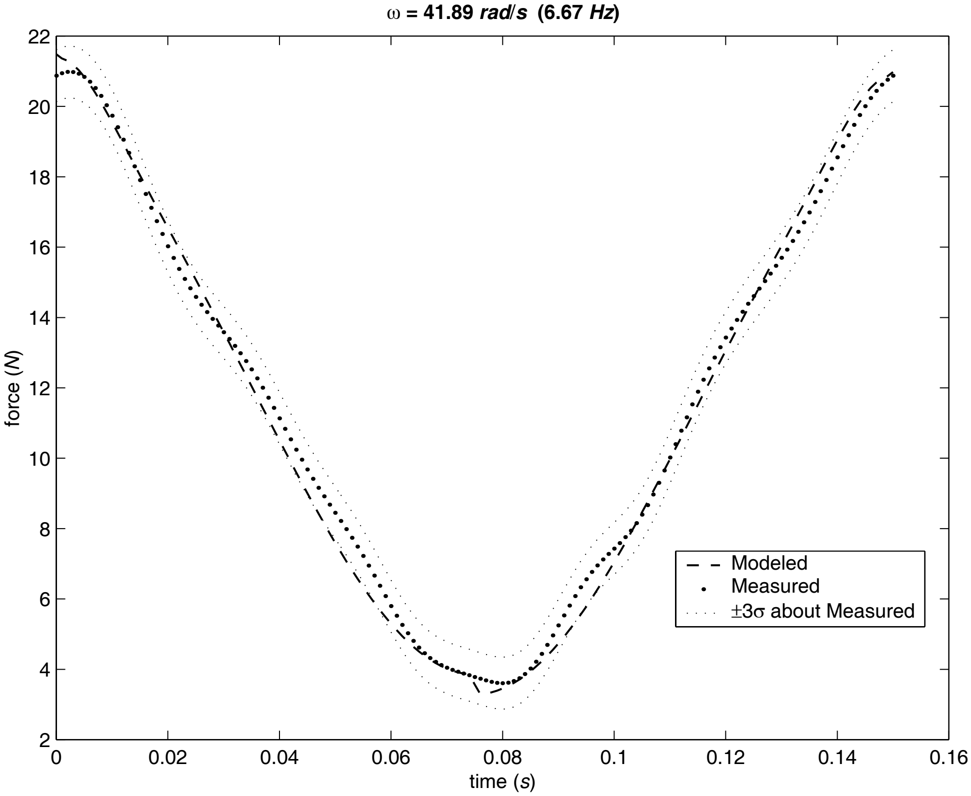

B.3 MECHANISM CLASS 1A-D III (CONTINUED)

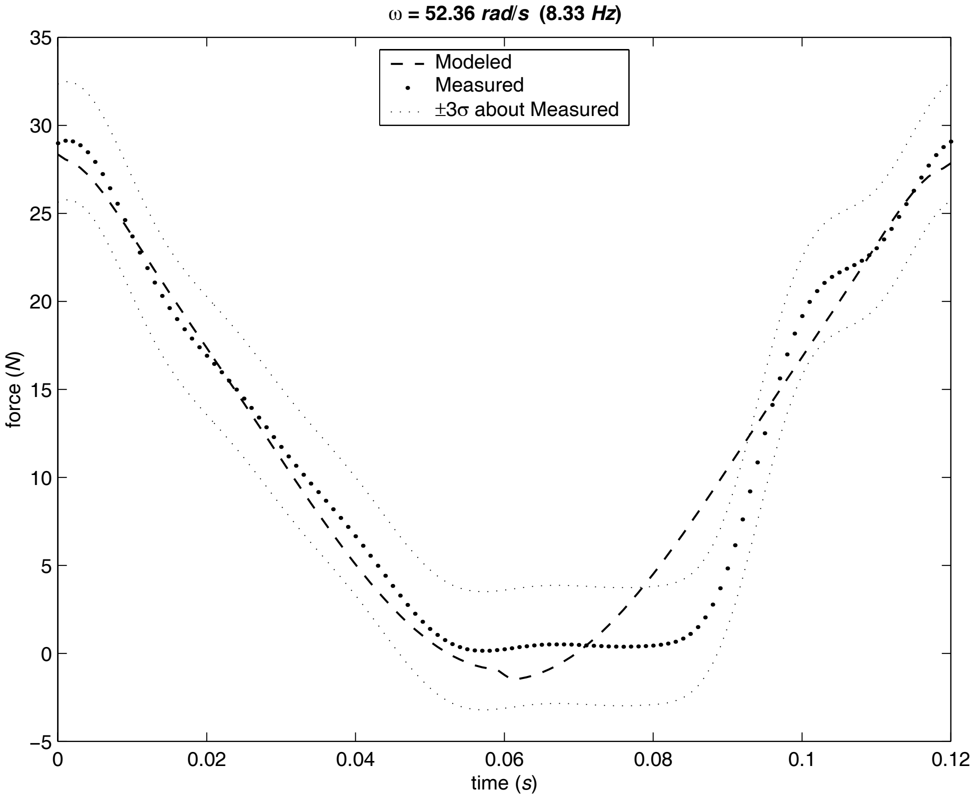

B.4 Mechanism Class 1B-g I

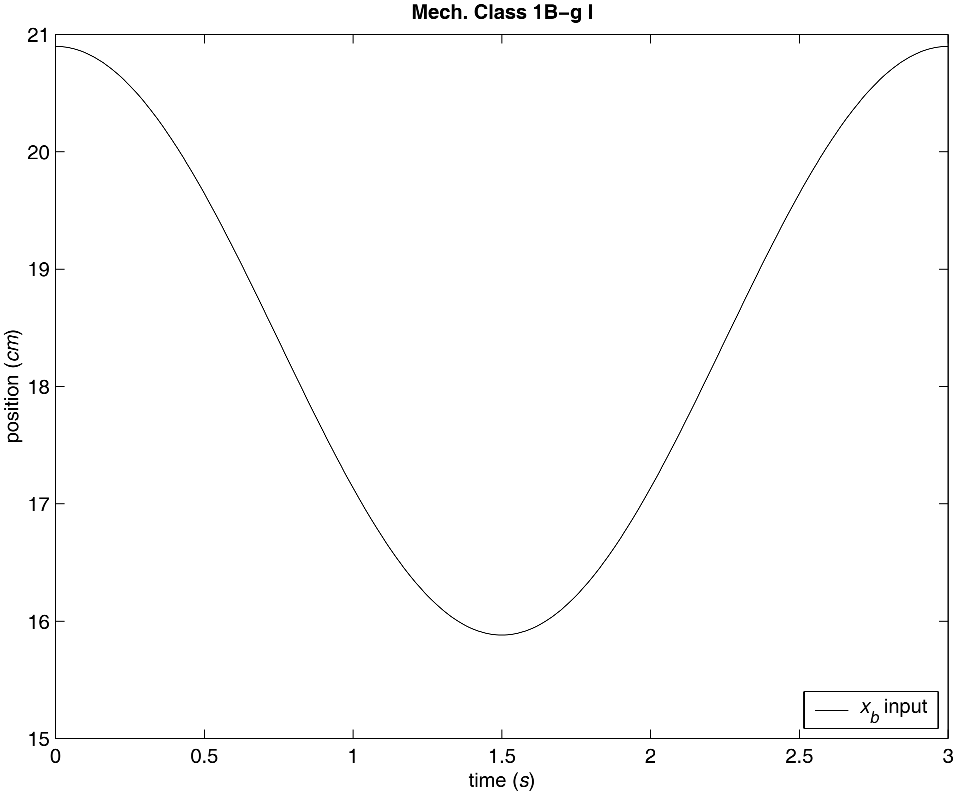

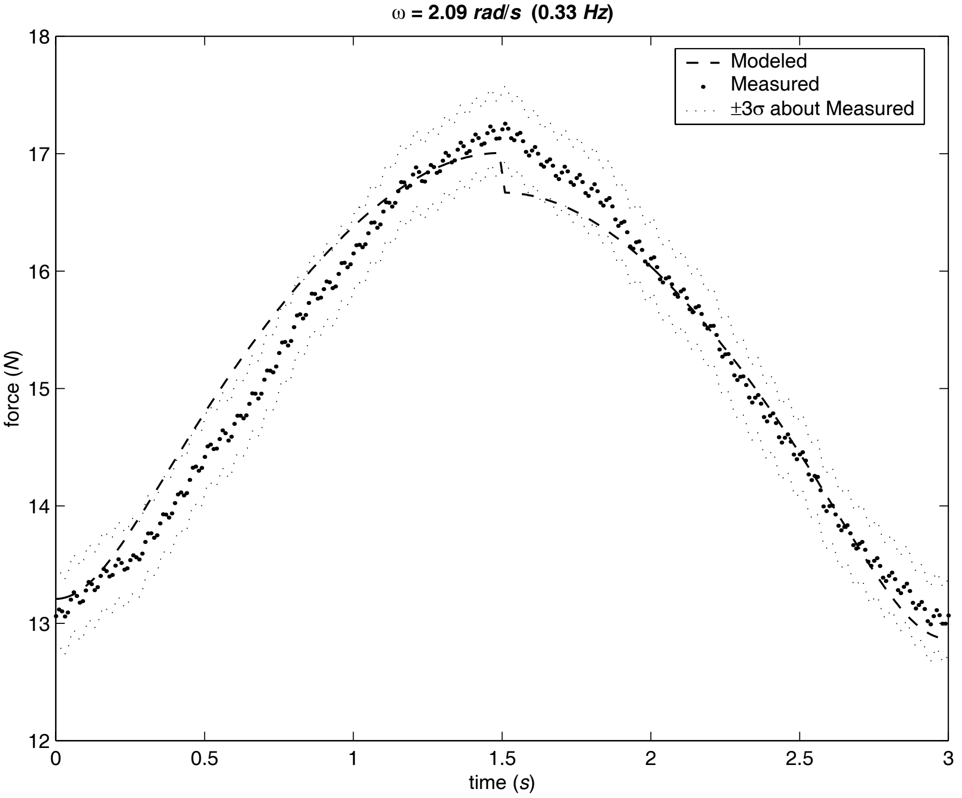

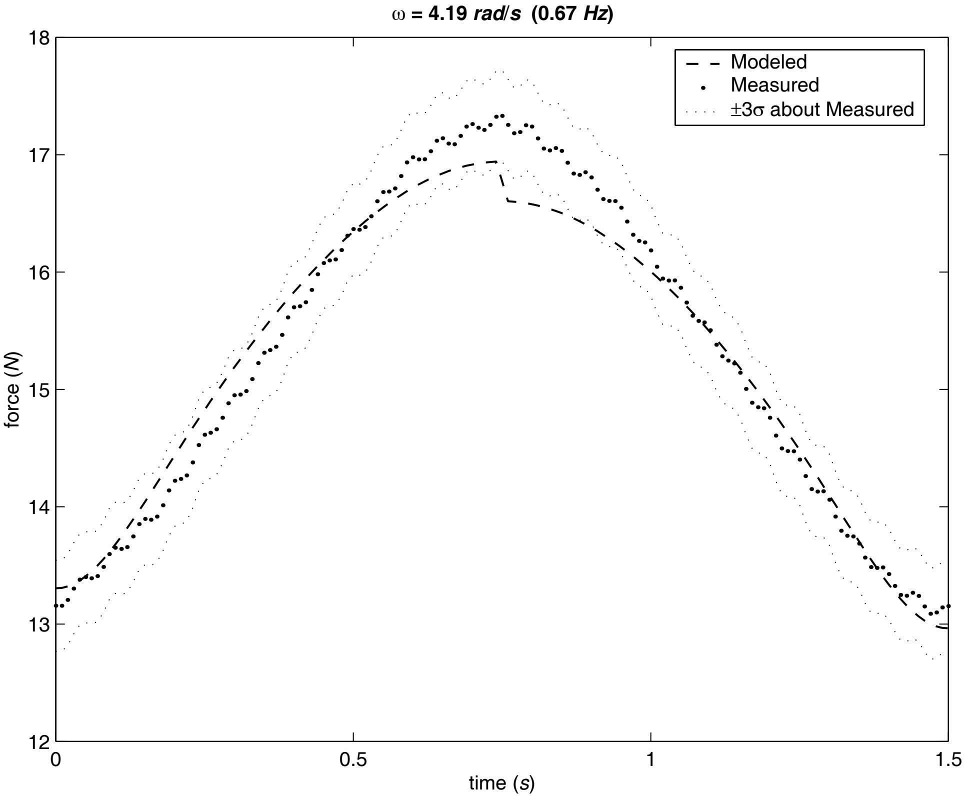
ω = 4.19 rad/s (0.67 Hz)
Modeled
Measured
±3σ about Measured
force (N)
time (s)
18
17
16
15
14
13
12
0
0.5
1
1.5

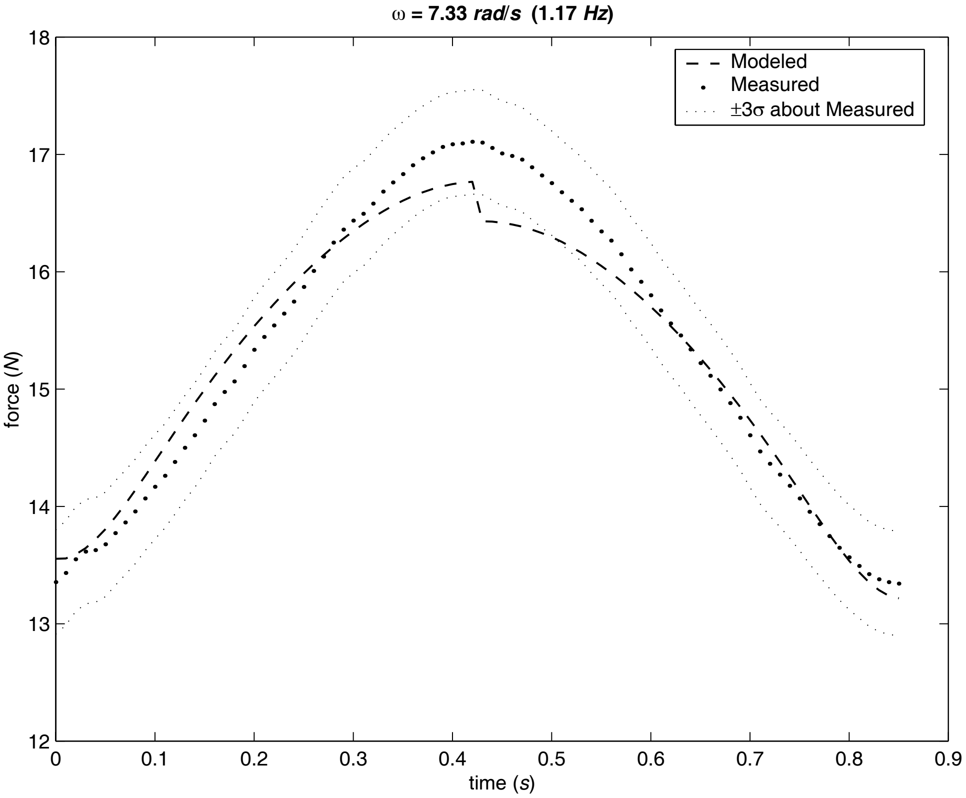
ω = 7.33 rad/s (1.17 Hz)
Modeled
Measured
±3σ about Measured
force (N)
time (s)
18
17
16
15
14
13
12
0
0.1
0.2
0.3
0.4
0.5
0.6
0.7
0.8
0.9

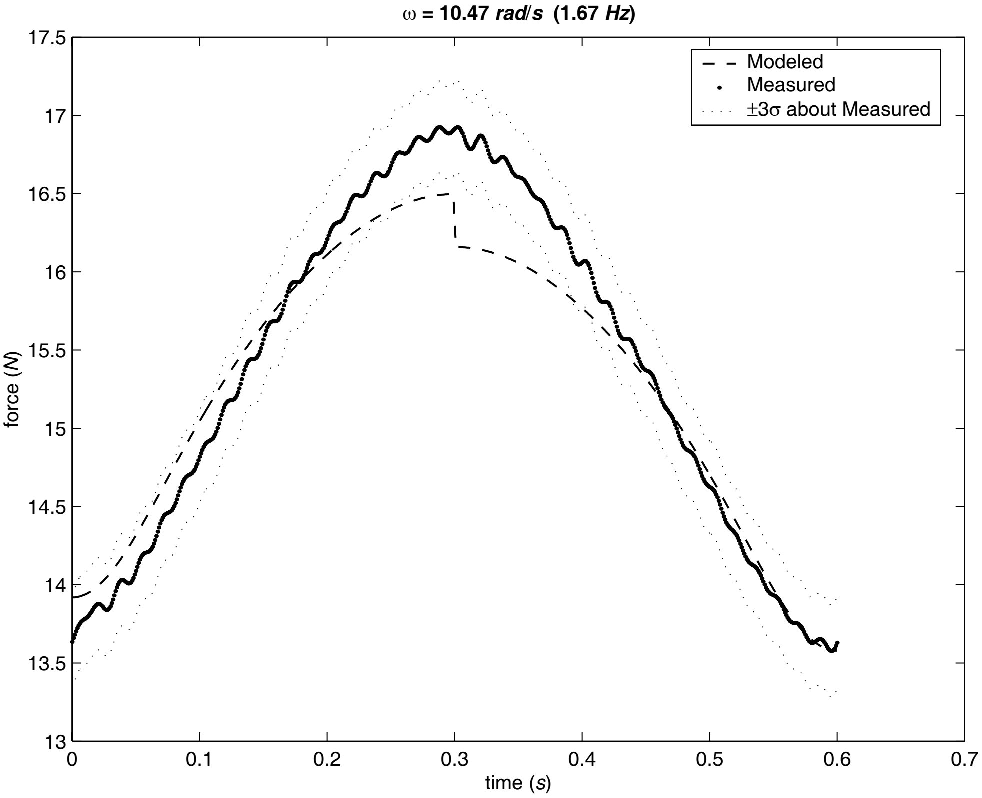
ω = 10.47 *rad/s* (1.67 *Hz*)
Modeled
Measured
±3σ about Measured
force (*N*)
time (*s*)
17.5
17
16.5
16
15.5
15
14.5
14
13.5
13
0
0.1
0.2
0.3
0.4
0.5
0.6
0.7

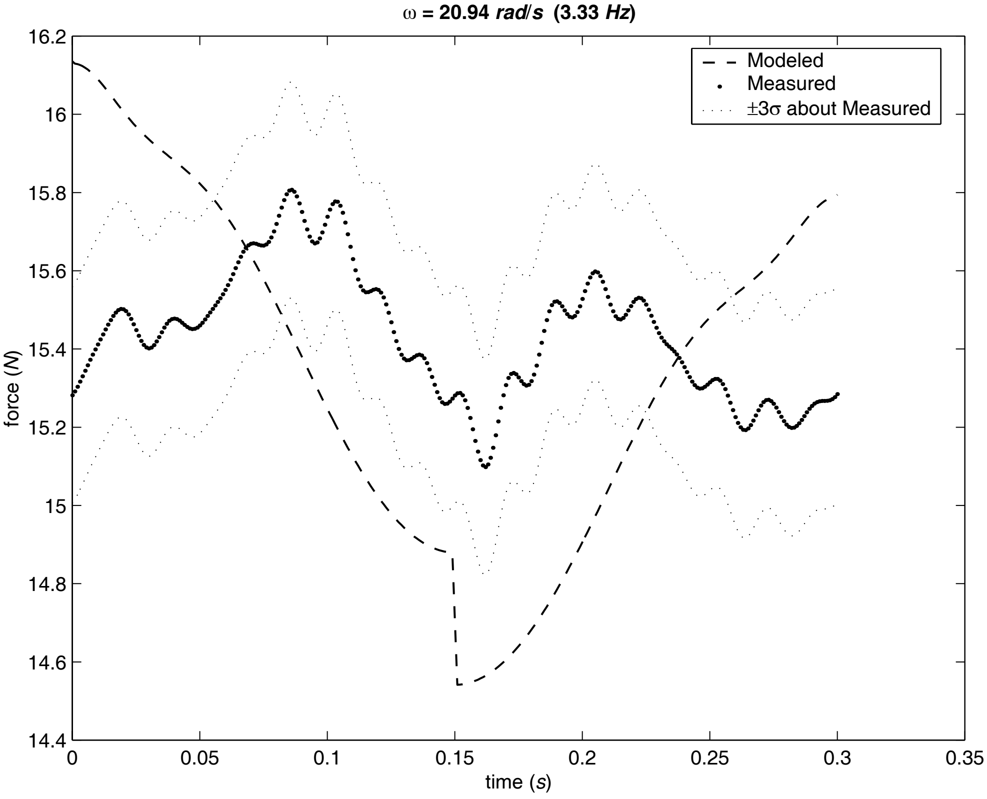
ω = 20.94 *rad/s* (3.33 *Hz*)
Modeled
Measured
±3σ about Measured
force (*N*)
time (*s*)
16.2
16
15.8
15.6
15.4
15.2
15
14.8
14.6
14.4
0
0.05
0.1
0.15
0.2
0.25
0.3
0.35

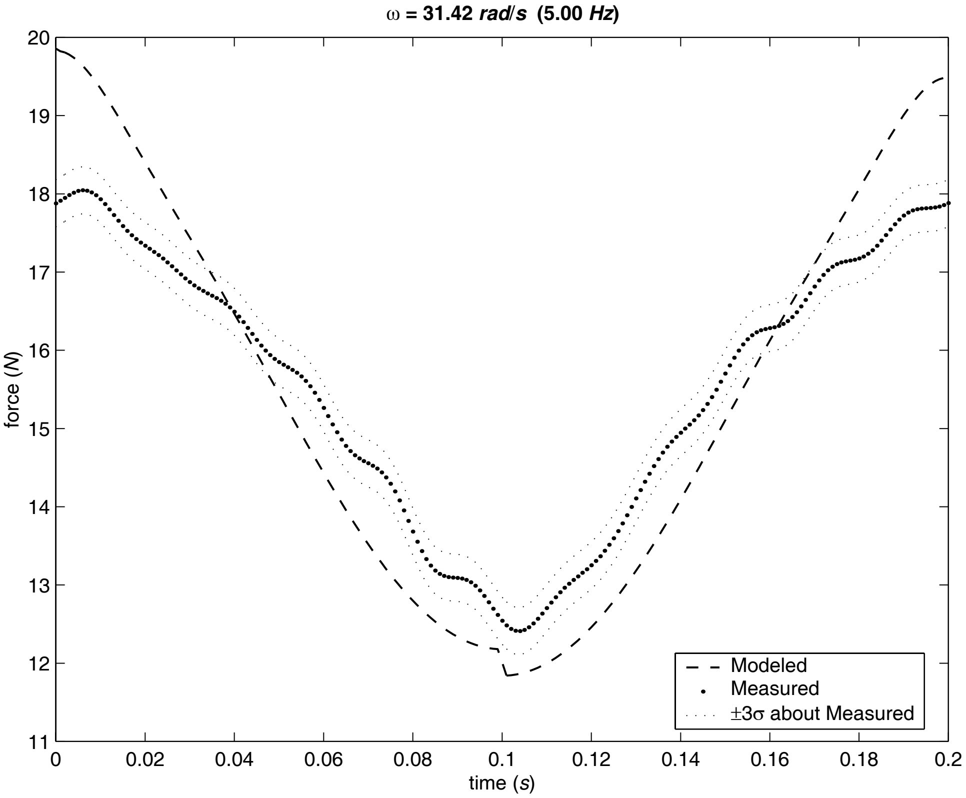
ω = 31.42 rad/s (5.00 Hz)
force (N)
time (s)
20
19
18
17
16
15
14
13
12
11
0
0.02
0.04
0.06
0.08
0.1
0.12
0.14
0.16
0.18
0.2
Modeled
Measured
±3σ about Measured

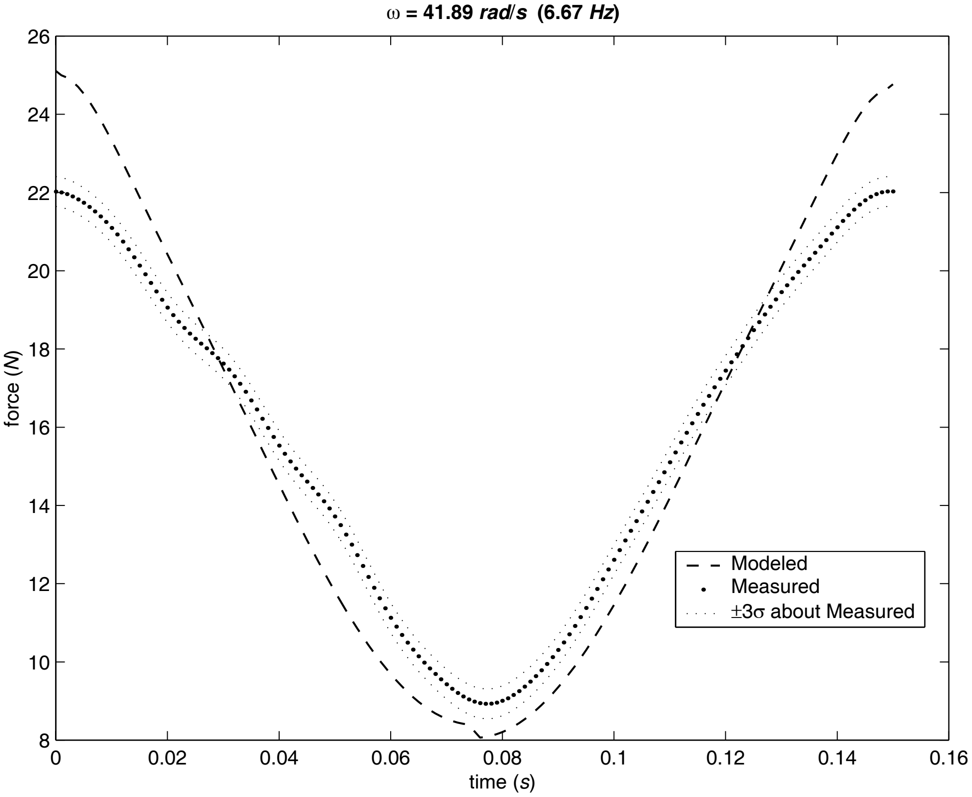
ω = 41.89 rad/s (6.67 Hz)
force (N)
time (s)
26
24
22
20
18
16
14
12
10
8
0
0.02
0.04
0.06
0.08
0.1
0.12
0.14
0.16
Modeled
Measured
±3σ about Measured

B.4 MECHANISM CLASS 1B-G I (CONTINUED)

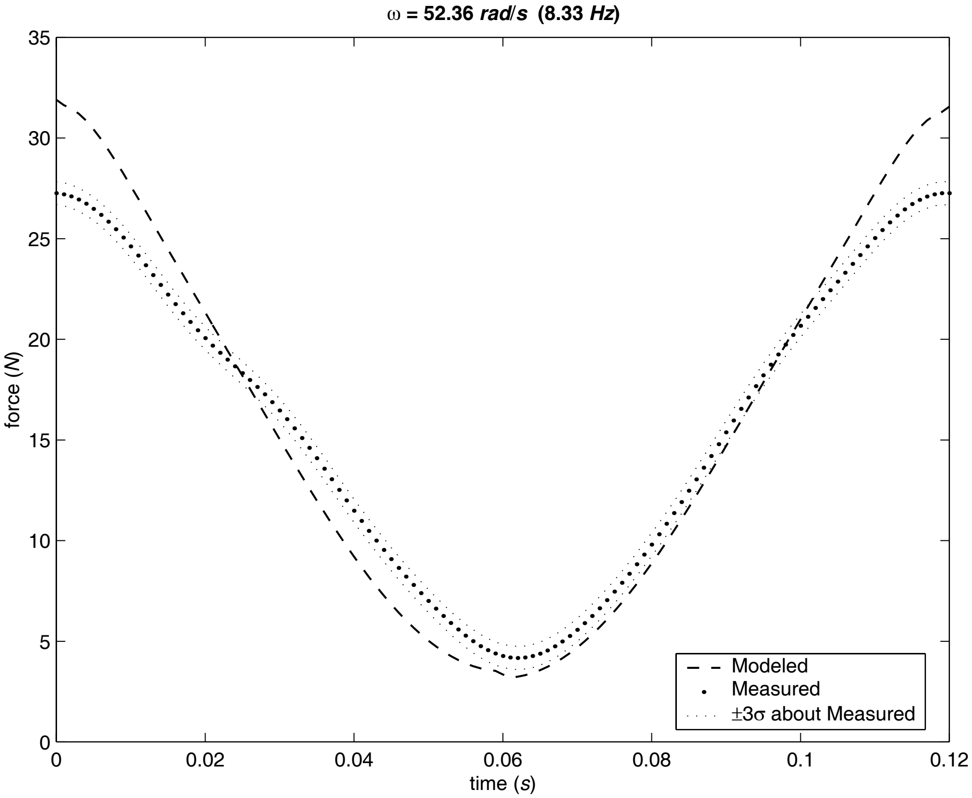

B.5 Mechanism Class 1B-g II

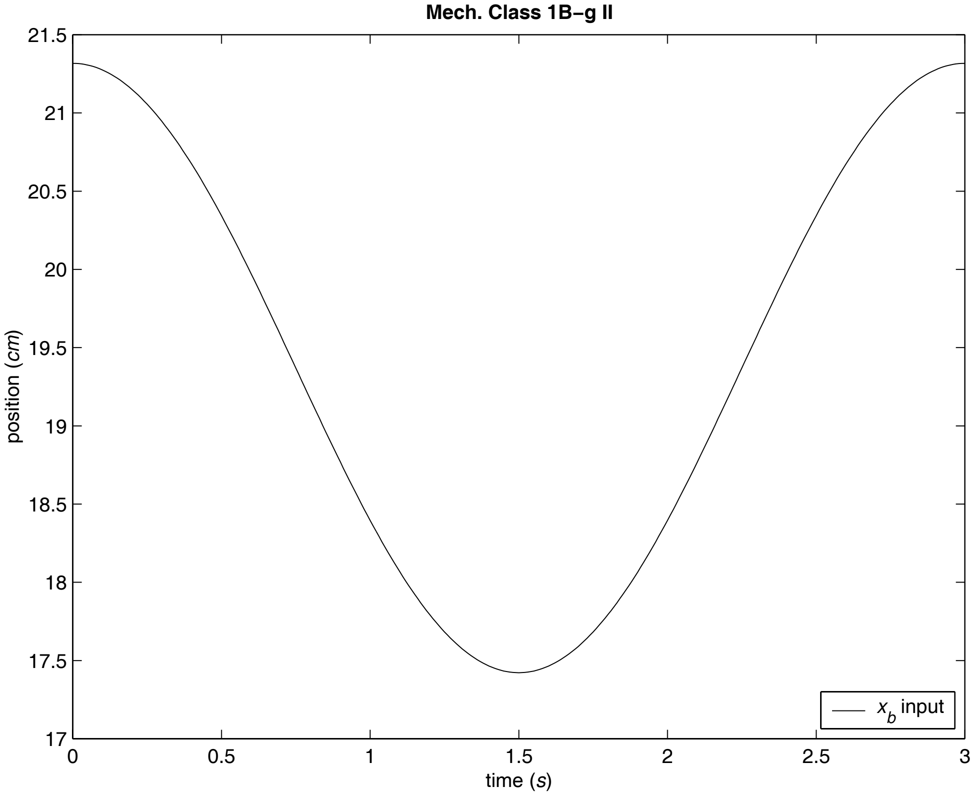

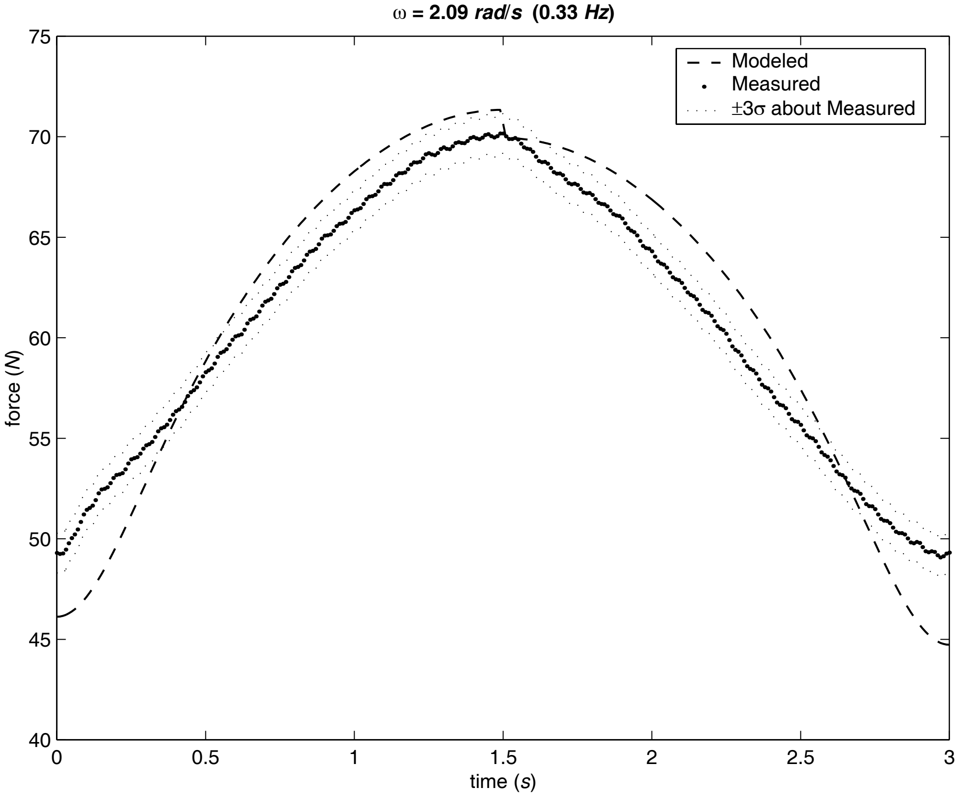

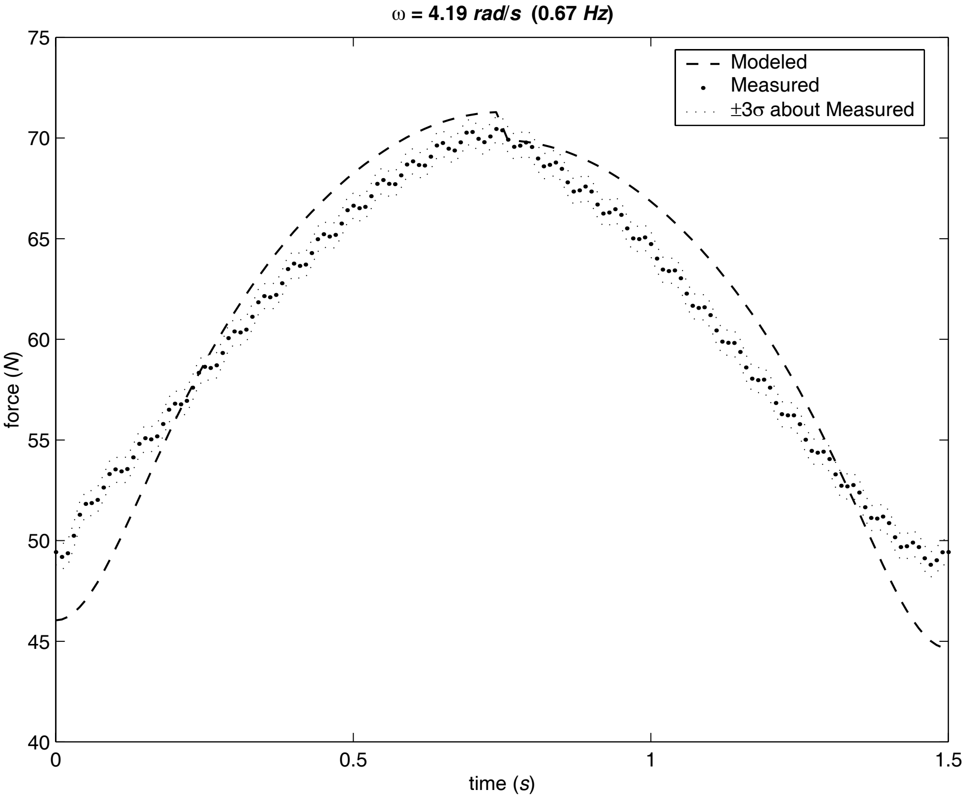
ω = 4.19 rad/s (0.67 Hz)
Modeled
Measured
±3σ about Measured
force (N)
time (s)
75
70
65
60
55
50
45
40
0
0.5
1
1.5

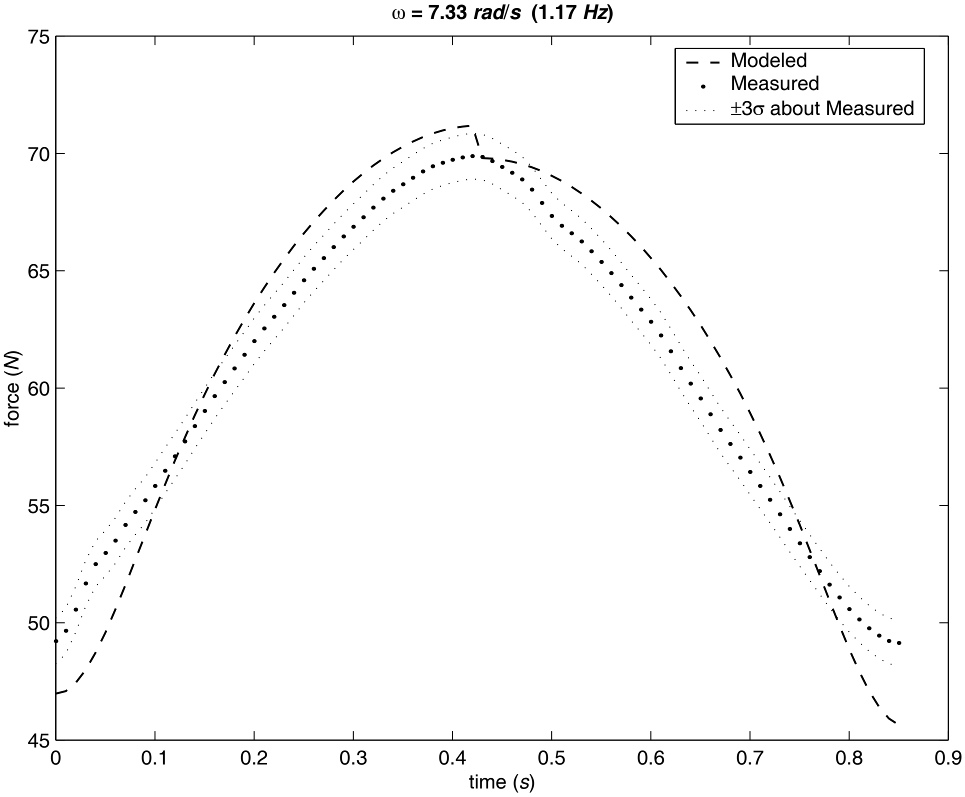
ω = 7.33 rad/s (1.17 Hz)
Modeled
Measured
±3σ about Measured
force (N)
time (s)
75
70
65
60
55
50
45
0
0.1
0.2
0.3
0.4
0.5
0.6
0.7
0.8
0.9

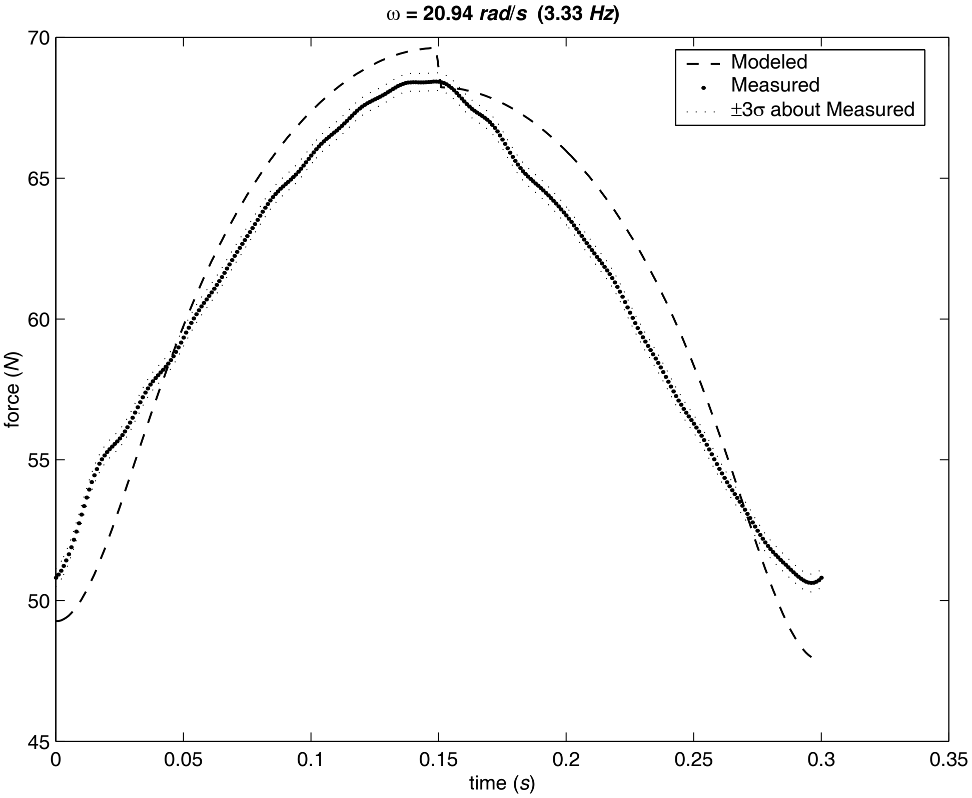
ω = 20.94 rad/s (3.33 Hz)
Modeled
Measured
±3σ about Measured
force (N)
time (s)
70
65
60
55
50
45
0
0.05
0.1
0.15
0.2
0.25
0.3
0.35

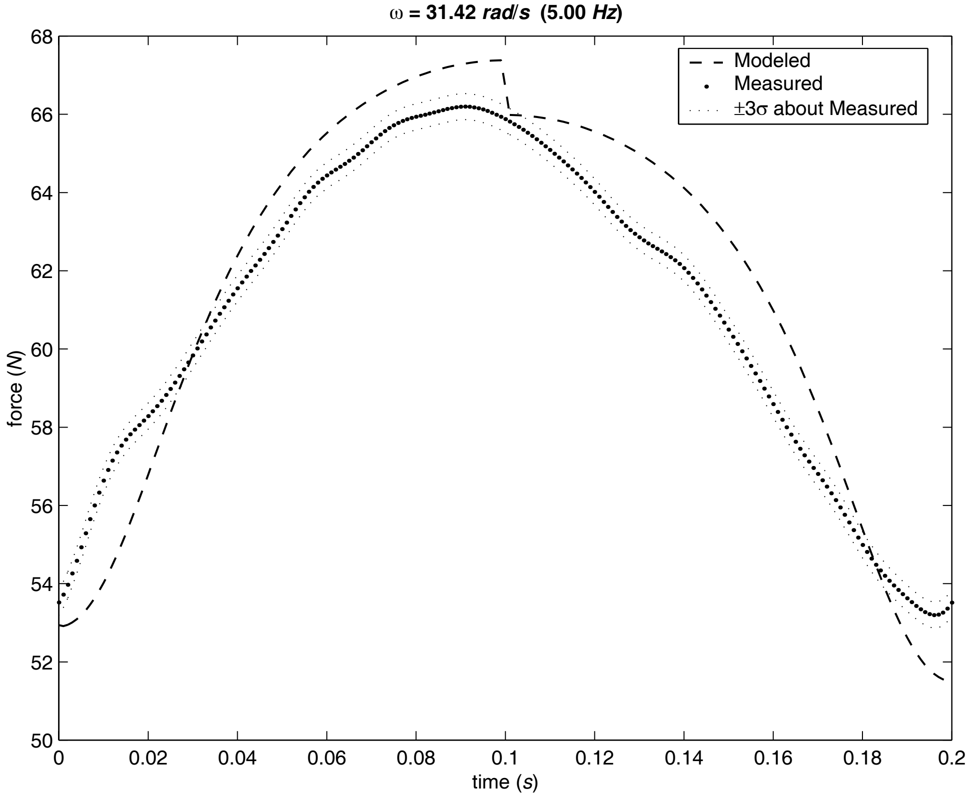
ω = 31.42 rad/s (5.00 Hz)
Modeled
Measured
±3σ about Measured
force (N)
time (s)
68
66
64
62
60
58
56
54
52
50
0
0.02
0.04
0.06
0.08
0.1
0.12
0.14
0.16
0.18
0.2

B.5 MECHANISM CLASS 1B-G II (CONTINUED)

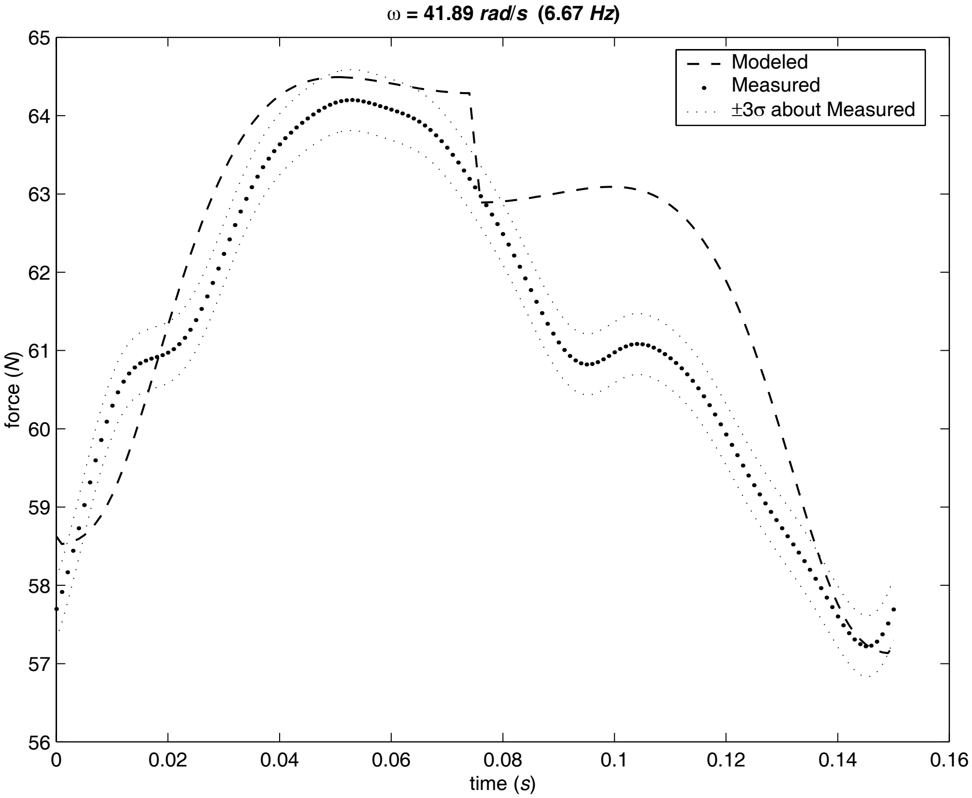

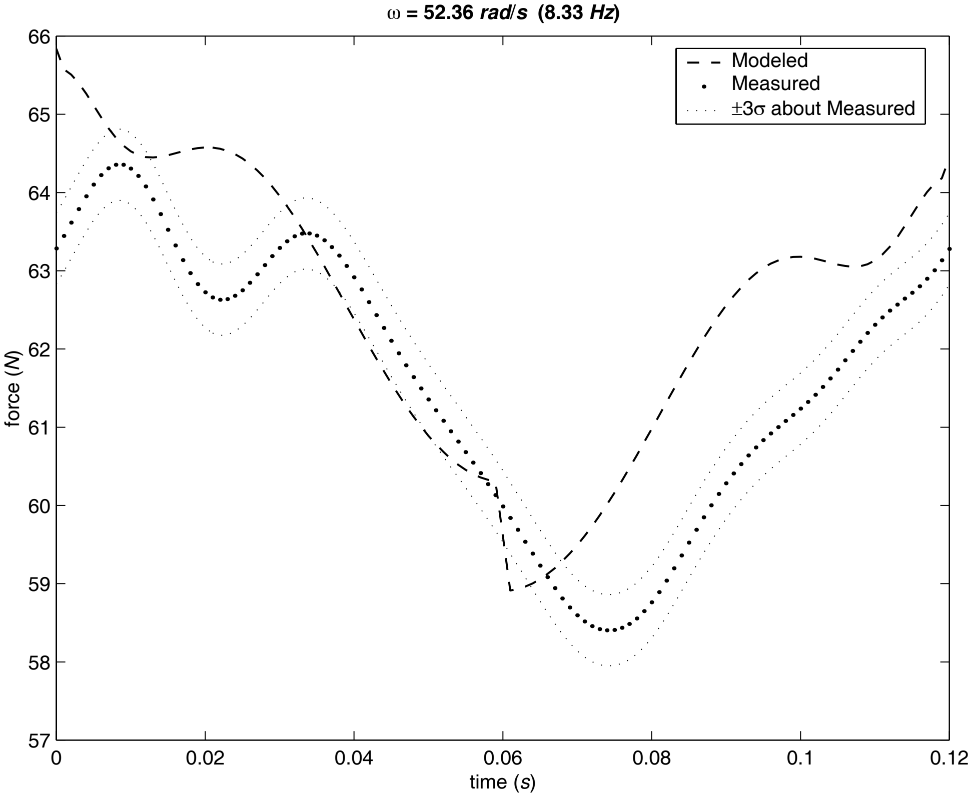

B.5 MECHANISM CLASS 1B-G II (CONTINUED)

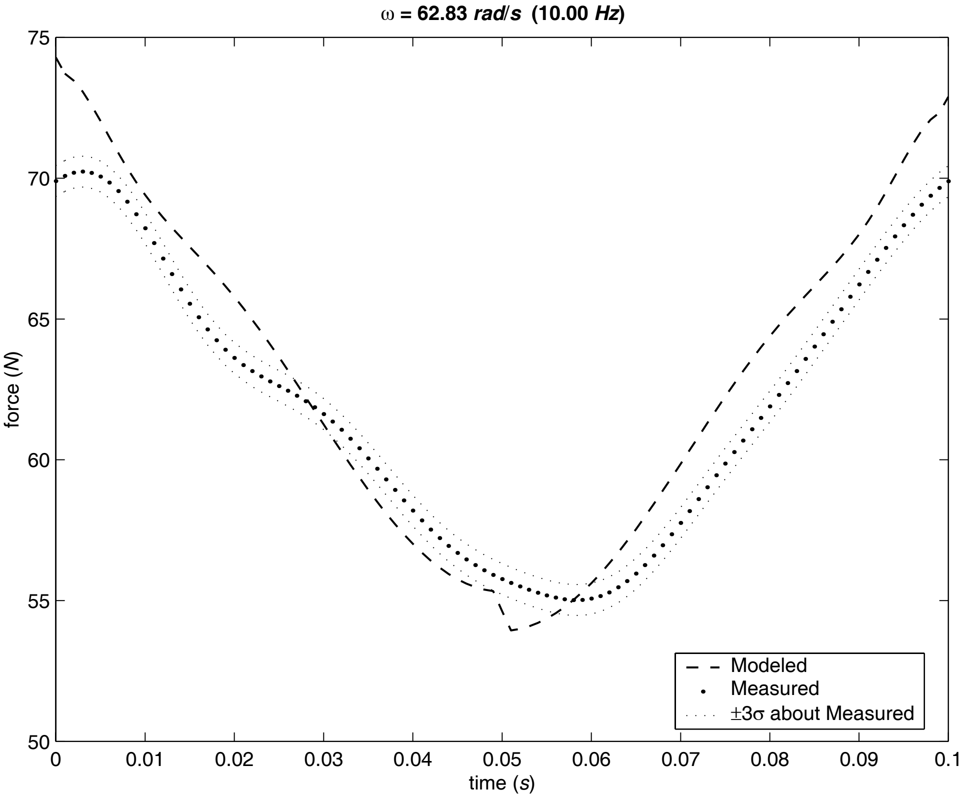

APPENDIX C Static Data

This appendix contains the static data used to empirically determine the Coulomb friction coefficient C and the unmodeled torque τ_{um} for the dynamic model using a least-squares fit, as discussed in Section 3.5 *Determining Coulomb Friction and Unmodeled Torque* on page 27.

Static data for mechanisms Class 1A-d II, Class 1A-d III, Class 1B-g I, and Class 1B-g II is presented. Graphical data for Class 1A-d I has already been given in Section 3.5. The experimentally determined values for C and τ_{um} for each of the four mechanisms is given in Table 7.1.

C.1 Mechanism Class 1A-d II

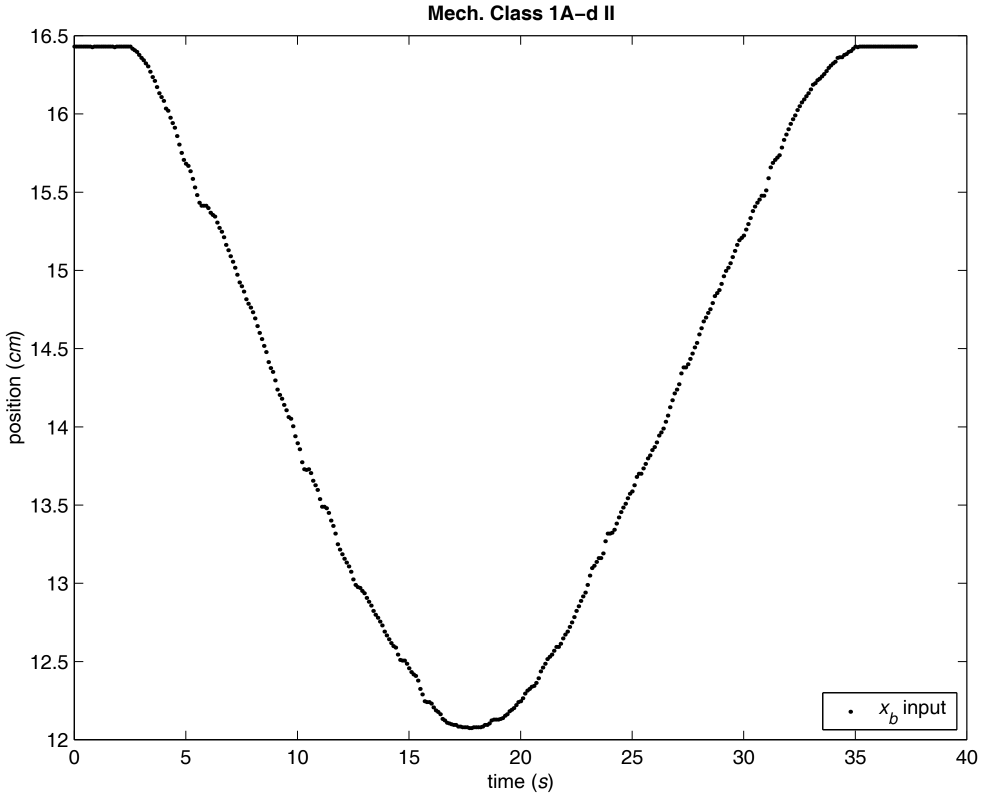

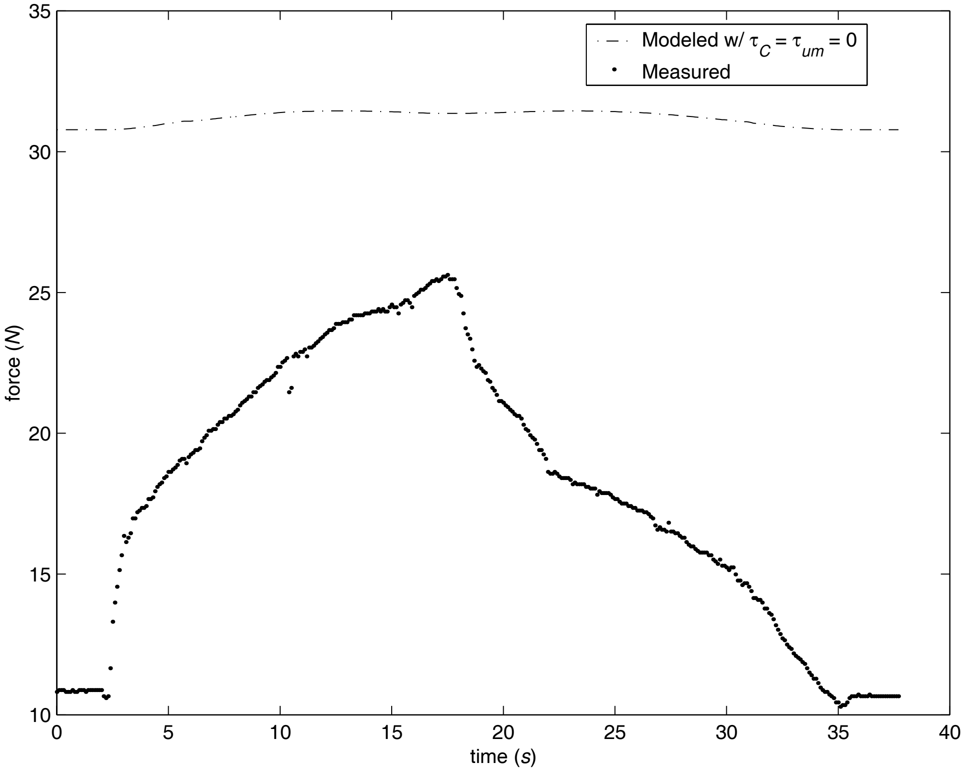

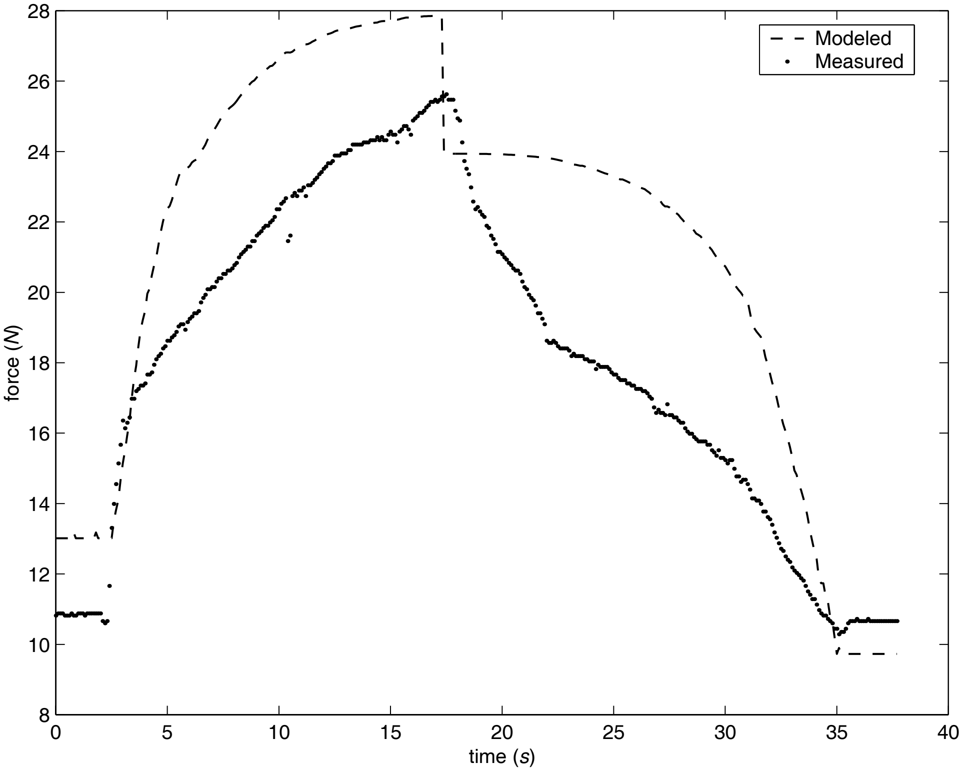
Modeled
Measured
force (N)
time (s)
28
26
24
22
20
18
16
14
12
10
8
0
5
10
15
20
25
30
35
40

C.2 Mechanism Class 1A-d III

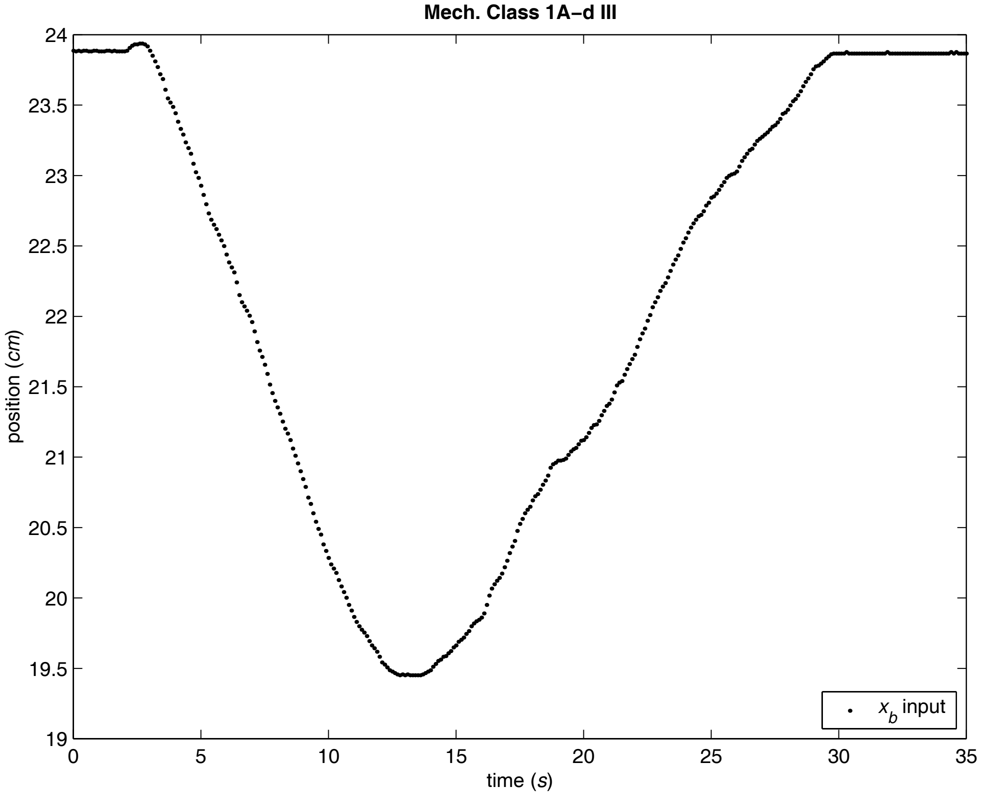

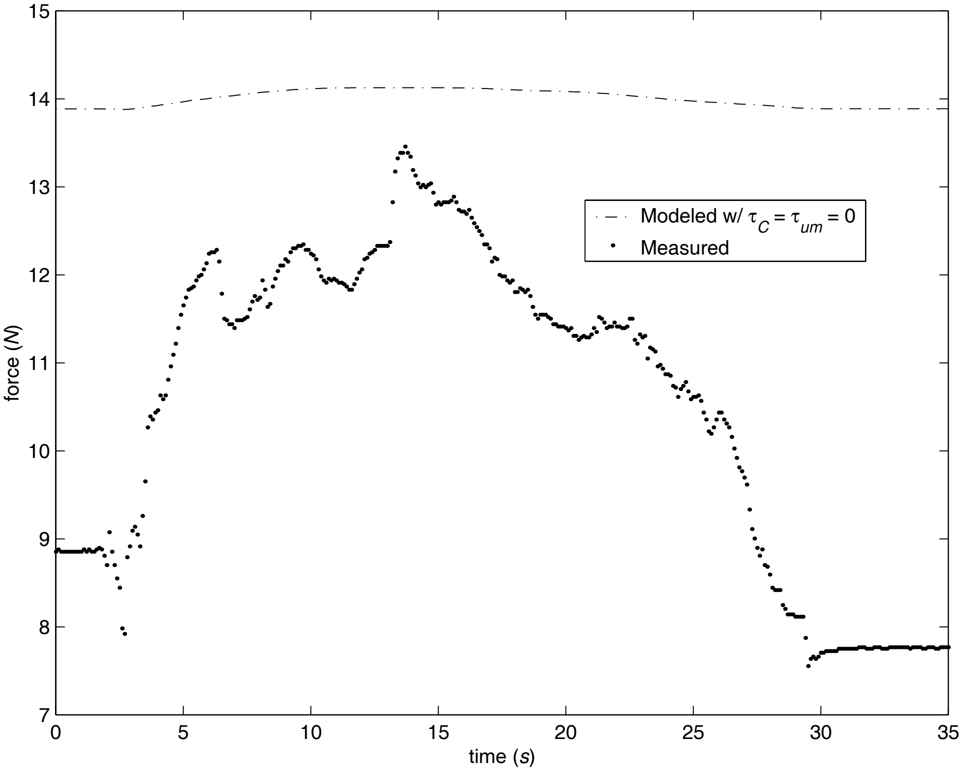

C.2 MECHANISM CLASS 1A-D III (CONTINUED)

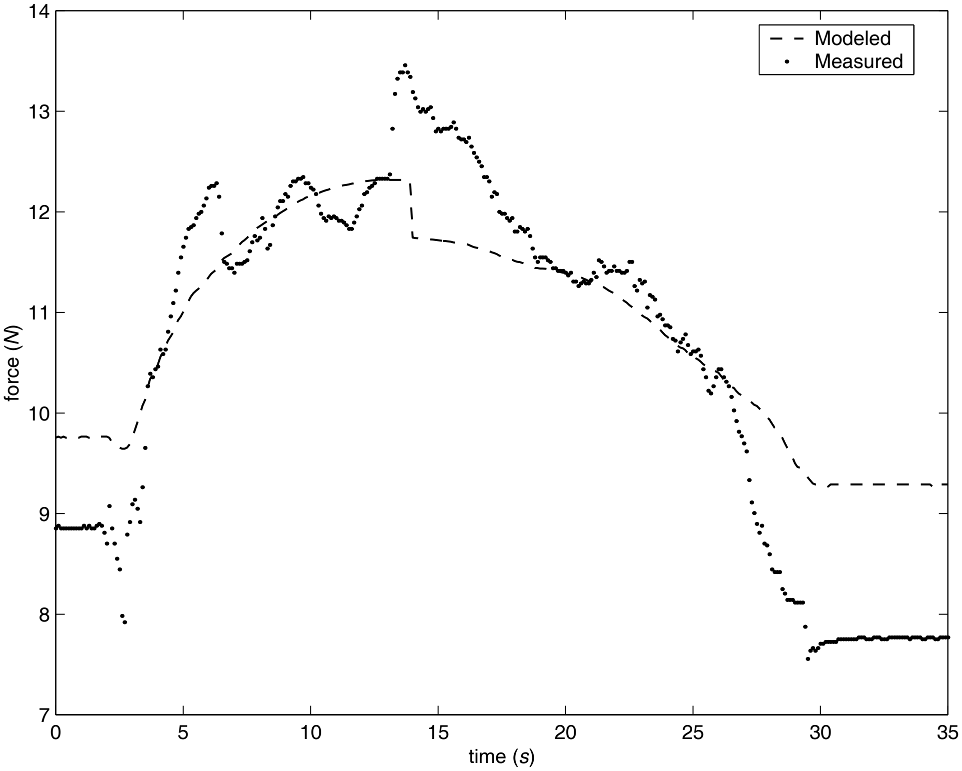

C.3 Mechanism Class 1B-g I

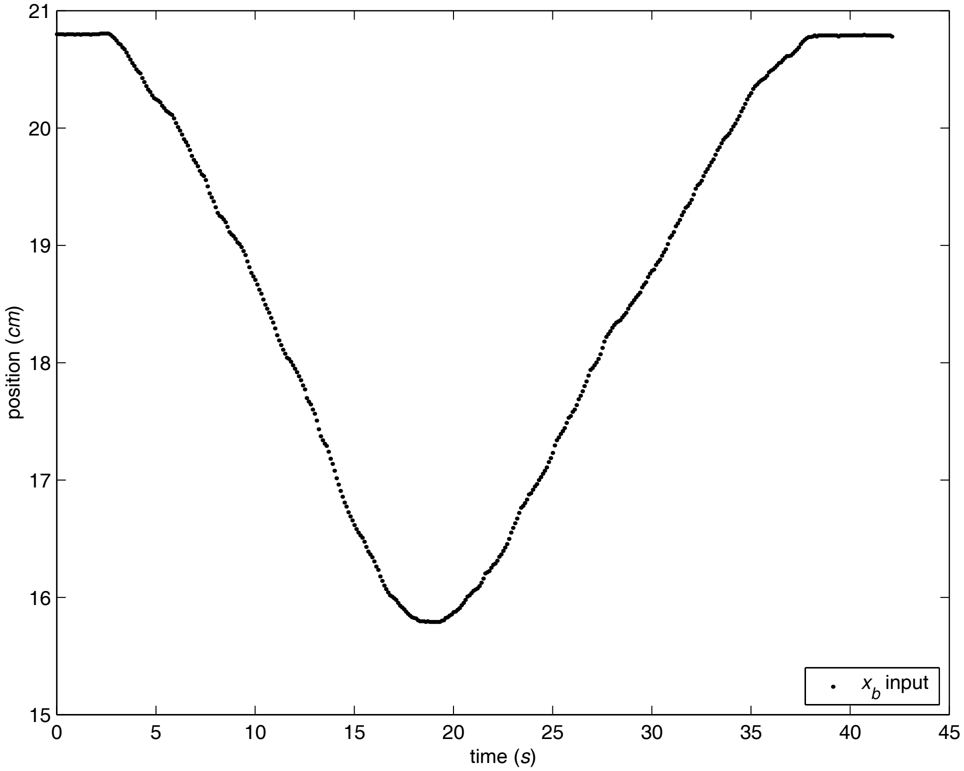

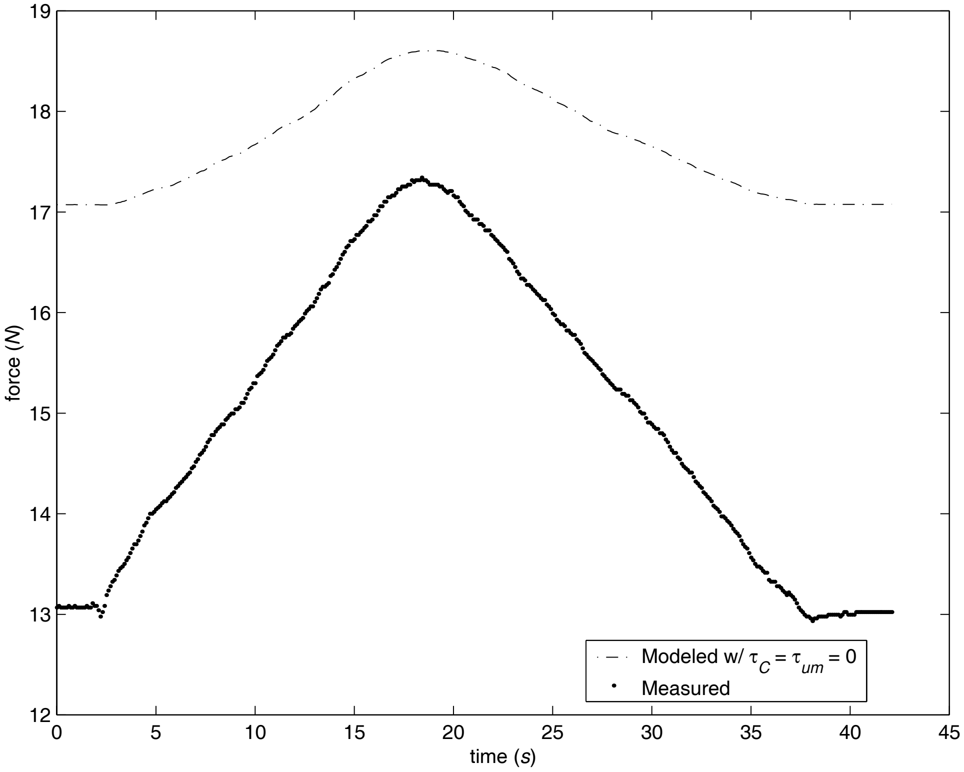

C.3 MECHANISM CLASS 1B-G I (CONTINUED)

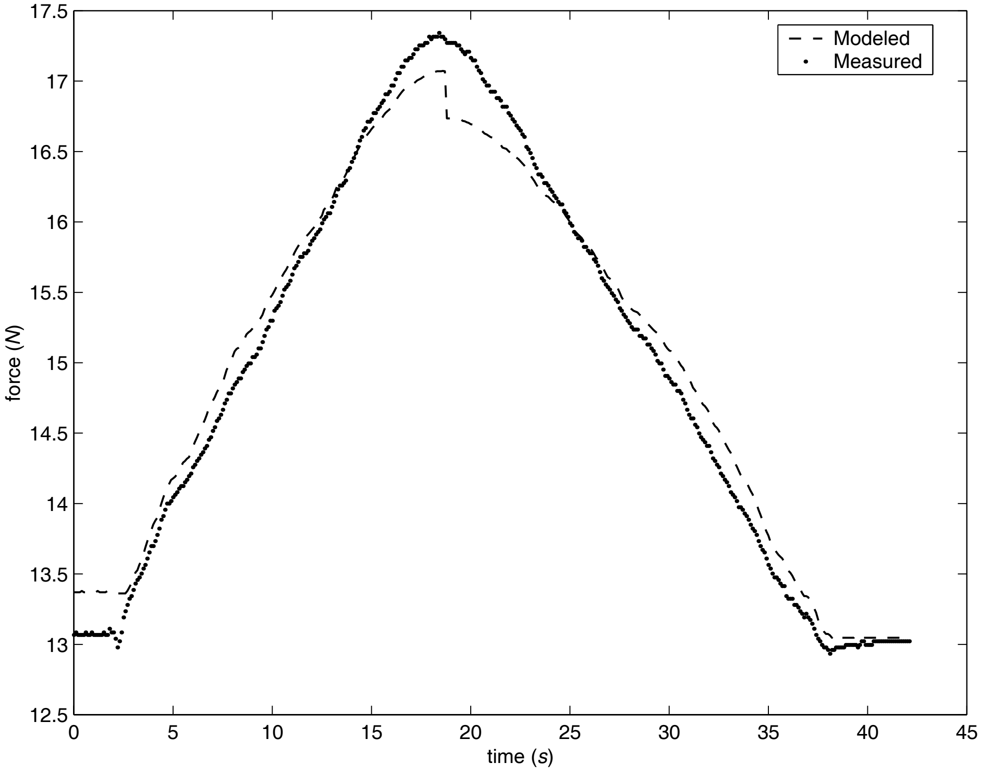

C.4 Mechanism Class 1B-g II

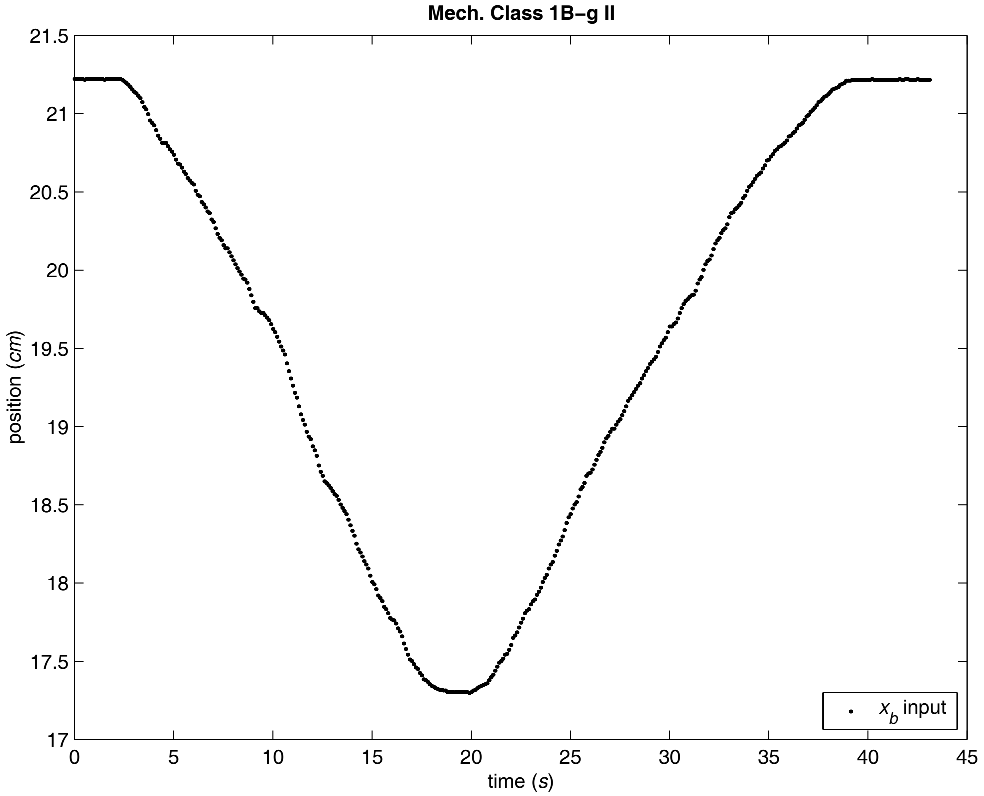

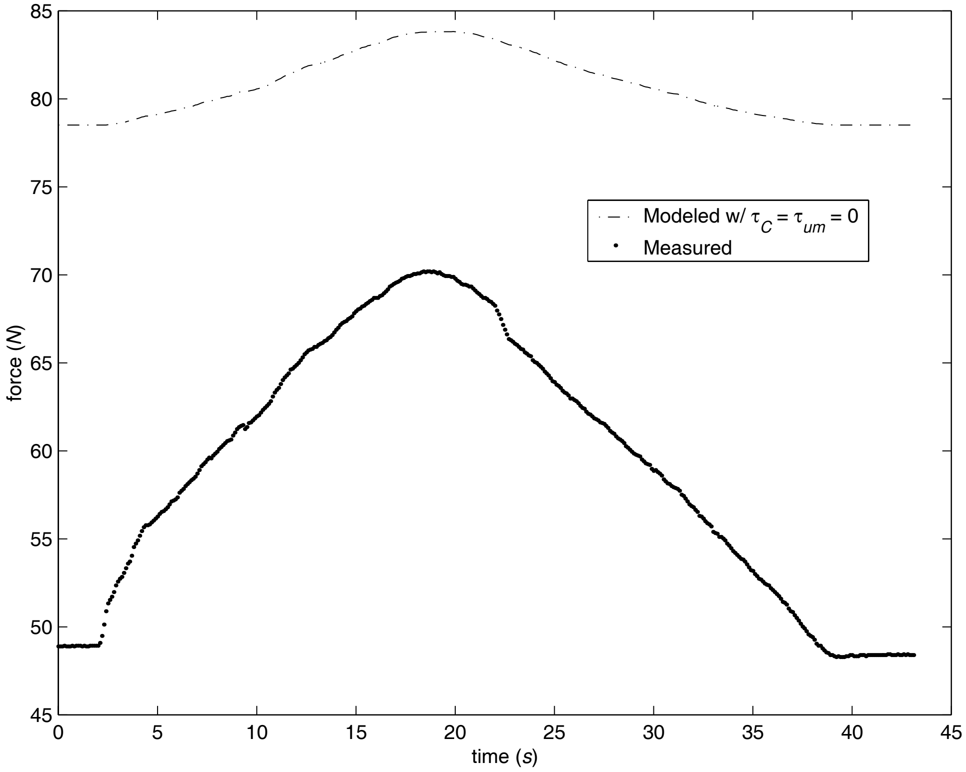

C.4 MECHANISM CLASS 1B-G II (CONTINUED)

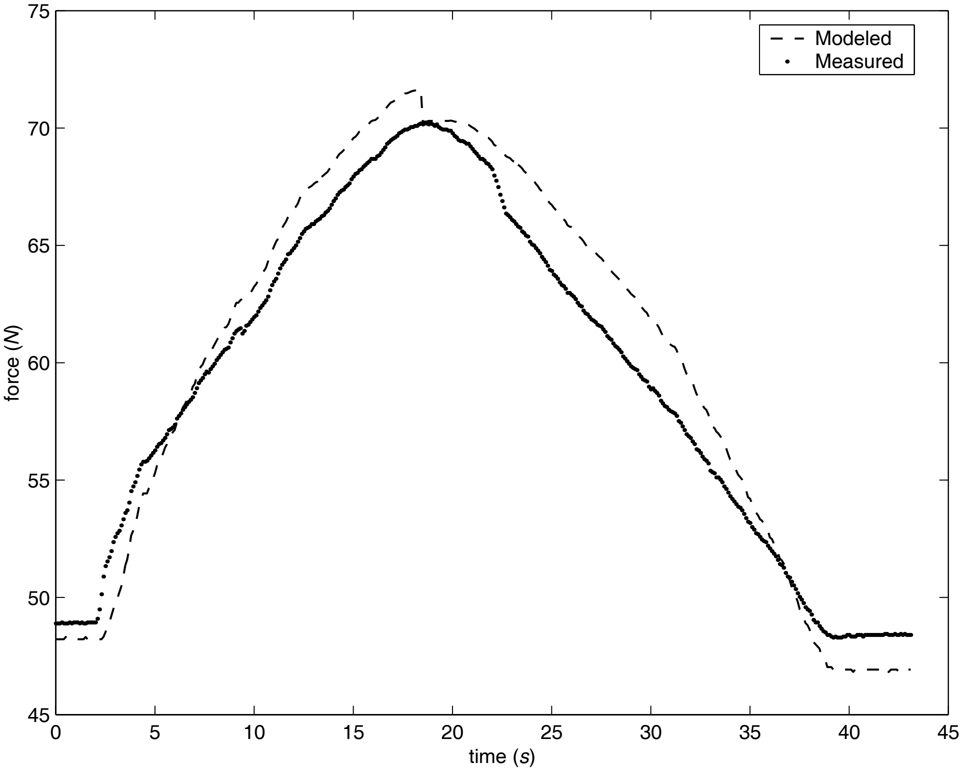

APPENDIX D

Supplemental Code

This appendix contains the batch file for the finite-element ANSYS® force-deflection model of compliant constant-force mechanism Class 1A-d I, as plotted in Figure 3.7. The flexible segment is divided into 20 elements, and the force is calculated over 40 positions across the full range of the mechanism's designed deflection. The model assumes an ideal mechanism with no friction.

Also included here is the core Matlab® code for simulating the generalized equation of motion of the dynamic model.

D.1 ANSYS® Batch File

```
/BATCH  by Brent Weight
/COM,ANSYS RELEASE  5.7    UP20001208       14:58:59    04/06/2001
/input,start57,ans     ,/ansys_inc/ansys57/docu/  ,,,,,,,,,,,,,,,,1
/show, x11
! /menu, on
/GRA,POWER
/GST,ON
/PLO,INFO,3
/COL,PBAK,ON,1,BLUE
/PREP7
!*
ET,1,BEAM3
!*
!*
!*
R,1,.025,1.3e-6, , , , ,
!*
R,2,1,1, , , , ,
!*
MPTEMP,,,,,,,,
MPTEMP,1,0
MPDATA,EX,1,,30e6
MPDATA,PRXY,1,,
MPTEMP,,,,,,,,
MPTEMP,1,0
MPDE,EX,1
MPDE,EY,1
MPDE,EZ,1
MPDE,NUXY,1
MPDE,NUYZ,1
MPDE,NUXZ,1
MPDE,PRXY,1
MPDE,PRYZ,1
MPDE,PRXZ,1
MPDE,GXY,1
MPDE,GYZ,1
MPDE,GXZ,1
MPDATA,EX,1,,3E+07
MPDATA,PRXY,1,,.3
FLST,3,1,8
FITEM,3,0,0,0
K, ,P51X
FLST,3,3,8
FITEM,3,2.162,0.1E-02,0
FITEM,3,2.162,0.1E-02,0
FITEM,3,5.122,0,0
K, ,P51X
LSTR,       1,       2
LSTR,       3,       4
CM,_Y,LINE
LSEL, , , ,       1
CM,_Y1,LINE
CMSEL,S,_Y
!*
!*
CMSEL,S,_Y1
LATT,1,2,1, , , ,
CMSEL,S,_Y
CMDELE,_Y
```

```
CMDELE,_Y1
!*
CM,_Y,LINE
LSEL, , , ,        2
CM,_Y1,LINE
CMSEL,S,_Y
!*
!*
CMSEL,S,_Y1
LATT,1,1,1, , , ,
CMSEL,S,_Y
CMDELE,_Y
CMDELE,_Y1
!*
/UI,MESH,OFF
FLST,5,1,4,ORDE,1
FITEM,5,2
CM,_Y,LINE
LSEL, , , ,P51X
CM,_Y1,LINE
CMSEL,,_Y
!*
LESIZE,_Y1, , ,20, , , , ,1
!*
FLST,5,1,4,ORDE,1
FITEM,5,1
CM,_Y,LINE
LSEL, , , ,P51X
CM,_Y1,LINE
CMSEL,,_Y
!*
LESIZE,_Y1, , ,7, , , , ,1
!*
FLST,2,2,4,ORDE,2
FITEM,2,1
FITEM,2,-2
LMESH,P51X
!CM,_Y1,ELEM
!CHECK,ESEL,WARN
!CMSEL,S,_Y1
!CMDELE,_Y1
!*
NPLOT
/PNUM,KP,0
/PNUM,LINE,0
/PNUM,AREA,0
/PNUM,VOLU,0
/PNUM,NODE,1
/PNUM,TABN,0
/PNUM,SVAL,0
/NUMBER,0
!*
/PNUM,ELEM,0
/REPLOT
!*
ksel,s,kp,,4
nslk,s
*get,nkp4,node,0,num,max
nsel,all
ksel,all
NLIST,ALL, , , ,NODE,NODE,NODE
FLST,4,2,1,ORDE,2
FITEM,4,2
```

```
FITEM,4,9
CP,1,UX,P51X
FLST,4,2,1,ORDE,2
FITEM,4,2
FITEM,4,9
CP,2,UY,P51X
FINISH
/SOLU
ANTYPE,0
NLGEOM,1
NROPT,AUTO, ,
LUMPM,0
EQSLV, , ,0,
PREC,0
PIVCHECK,1
SSTIF
PSTRES
TOFFST,0,
DK,1, ,0, ,0,UX,UY, , , , ,
DK,4, ,0, ,0,UY,ROTZ , , , , ,
DK,4, ,-1*1.873/40, ,0,UX, , , , , ,
lswrite,1
DK,4, ,-2*1.873/40, ,0,UX, , , , , ,
lswrite,2
DK,4, ,-3*1.873/40, ,0,UX, , , , , ,
lswrite,3
DK,4, ,-4*1.873/40, ,0,UX, , , , , ,
lswrite,4
DK,4, ,-5*1.873/40, ,0,UX, , , , , ,
lswrite,5
DK,4, ,-6*1.873/40, ,0,UX, , , , , ,
lswrite,6
DK,4, ,-7*1.873/40, ,0,UX, , , , , ,
lswrite,7
DK,4, ,-8*1.873/40, ,0,UX, , , , , ,
lswrite,8
DK,4, ,-9*1.873/40, ,0,UX, , , , , ,
lswrite,9
DK,4, ,-10*1.873/40, ,0,UX, , , , , ,
lswrite,10
DK,4, ,-11*1.873/40, ,0,UX, , , , , ,
lswrite,1
DK,4, ,-12*1.873/40, ,0,UX, , , , , ,
lswrite,12
DK,4, ,-13*1.873/40, ,0,UX, , , , , ,
lswrite,13
DK,4, ,-14*1.873/40, ,0,UX, , , , , ,
lswrite,14
DK,4, ,-15*1.873/40, ,0,UX, , , , , ,
lswrite,15
DK,4, ,-16*1.873/40, ,0,UX, , , , , ,
lswrite,16
DK,4, ,-17*1.873/40, ,0,UX, , , , , ,
lswrite,17
DK,4, ,-18*1.873/40, ,0,UX, , , , , ,
lswrite,18
DK,4, ,-19*1.873/40, ,0,UX, , , , , ,
lswrite,19
DK,4, ,-20*1.873/40, ,0,UX, , , , , ,
lswrite,20
DK,4, ,-21*1.873/40, ,0,UX, , , , , ,
lswrite,21
DK,4, ,-22*1.873/40, ,0,UX, , , , , ,
```

```
lswrite,22
DK,4, ,-23*1.873/40, ,0,UX, , , , , ,
lswrite,23
DK,4, ,-24*1.873/40, ,0,UX, , , , , ,
lswrite,24
DK,4, ,-25*1.873/40, ,0,UX, , , , , ,
lswrite,25
DK,4, ,-26*1.873/40, ,0,UX, , , , , ,
lswrite,26
DK,4, ,-27*1.873/40, ,0,UX, , , , , ,
lswrite,27
DK,4, ,-28*1.873/40, ,0,UX, , , , , ,
lswrite,28
DK,4, ,-29*1.873/40, ,0,UX, , , , , ,
lswrite,29
DK,4, ,-30*1.873/40, ,0,UX, , , , , ,
lswrite,30
DK,4, ,-31*1.873/40, ,0,UX, , , , , ,
lswrite,31
DK,4, ,-32*1.873/40, ,0,UX, , , , , ,
lswrite,32
DK,4, ,-33*1.873/40, ,0,UX, , , , , ,
lswrite,33
DK,4, ,-34*1.873/40, ,0,UX, , , , , ,
lswrite,34
DK,4, ,-35*1.873/40, ,0,UX, , , , , ,
lswrite,35
DK,4, ,-36*1.873/40, ,0,UX, , , , , ,
lswrite,36
DK,4, ,-37*1.873/40, ,0,UX, , , , , ,
lswrite,37
DK,4, ,-38*1.873/40, ,0,UX, , , , , ,
lswrite,38
DK,4, ,-39*1.873/40, ,0,UX, , , , , ,
lswrite,39
DK,4, ,-40*1.873/40, ,0,UX, , , , , ,
lswrite,40


lsSOLVE,1,40,1
FINISH
/POST26
NSOL,2,nkp4,U,X,ux
RFORCE,3,nkp4,F,X,fx
/output,ansysoutput
PRVAR,1,2,3, , , , , ,
/output
FINISH
```

D.2 Matlab® Dynamic Model Simulation

```
        clear all; close all;

        format long

        addpath mechparams;

        directlst =
{'config1Adi_dynamic_sgft','config1Adii_dynamic','config1Adiii_dynamic','config1Bgi_dynami
c','config1Bgii_dynamic'};
        mechlst = {'Class1Ad_I','Class1Ad_II','Class1Ad_III','Class1Bg_I','Class1Bg_II'};
        yminlst = [0 0 0 0 0];
        ymaxlst = [22 22 6 10 60];

        for j = 1:5
           %read in or define mechanism parameters
           eval(['[config,mechnum,mechparam] = ',char(mechlst(j)),';']);
           direct = directlst(j);

           r2 = mechparam(1);  %m
           r3 = mechparam(2);  %m
           r6 = mechparam(3);  %m
           m2 = mechparam(4);  %kg
           m3 = mechparam(5);  %kg
           ms = mechparam(6);  %kg
           k1 = mechparam(7);  %N-m
           k2 = mechparam(8);  %N-m
           k3 = mechparam(9);  %N-m
           Fnom = mechparam(10);  %N
           C = mechparam(11);  %N-m
           tauum = mechparam(12);  %N-m

           maxxb = r2+r3+r6;  %m
           minxb = maxxb - .40*(r2+r3);  %m
           maxxb = maxxb - 1/10*(maxxb-minxb);  %give a pre-load (pre-displacement)

           pktopkxb = maxxb-minxb;
           meanxb = mean([maxxb minxb]);

           N = 400;  % resolution of final plot
           endw = 150;
           w = linspace(0.1,endw,N);  %rad/s

           meanFmod = zeros(1,N);
           magFmod = zeros(1,N);
           for i = 1:N
              %generate an input xb
              t = linspace(0,2*pi/w(i),100);
              xb = 1/2*pktopkxb*cos(w(i)*t)+meanxb;

              paramlen = [r2,r3,r6];
              [theta2,theta2d,theta2dd] = gettheta2s(paramlen,t,xb);  %theta2, theta2d,
theta2dd in rad, rad/s, rad/s^2

              parameom = [r2,r3,m2,m3,ms,k1,k2,k3,length(t)];
              [tauFb,pxbptheta2] = eqofmotion(parameom,theta2,theta2d,theta2dd);  %tauFb in
Newton-meters, pxbptheta2 in meters
              parameomnoms = [r2,r3,m2,m3,0,k1,k2,k3,length(t)];
              [tauFbnoms,pxbptheta2] = eqofmotion(parameomnoms,theta2,theta2d,theta2dd);
              parameomnom2m3ms = [r2,r3,0,0,0,k1,k2,k3,length(t)];
```

```
             [tauFbnom2m3ms,pxbptheta2] = eqofmo-
tion(parameomnom2m3ms,theta2,theta2d,theta2dd);
             parameomfourm2 = [r2,r3,4*m2,m3,ms,k1,k2,k3,length(t)];
             [tauFbfourm2,pxbptheta2] = eqofmo-
tion(parameomfourm2,theta2,theta2d,theta2dd);
             parameomfourthms = [r2,r3,m2,m3,1/4*ms,k1,k2,k3,length(t)];
             [tauFbfourthms,pxbptheta2] = eqofmotion(parameom-
fourthms,theta2,theta2d,theta2dd);

             tauC = C*theta2.*sign(theta2d);

             Qtheta2 = tauFb + tauC + tauum;  %N-m
             Qtheta2notaus = tauFb;  %N-m
             Qtheta2noms = tauFbnoms + tauC + tauum;  %N-m
             Qtheta2nom2m3ms = tauFbnom2m3ms + tauC + tauum;  %N-m
             Qtheta2fourm2 = tauFbfourm2 + tauC + tauum;  %N-m
             Qtheta2fourthms = tauFbfourthms + tauC + tauum;  %N-m

             Fb = Qtheta2./pxbptheta2;   %N
             Fbnotaus = Qtheta2notaus./pxbptheta2;   %N
             Fbnoms = Qtheta2noms./pxbptheta2;   %N
             Fbnom2m3ms = Qtheta2nom2m3ms./pxbptheta2;   %N
             Fbfourm2 = Qtheta2fourm2./pxbptheta2;   %N
             Fbfourthms = Qtheta2fourthms./pxbptheta2;   %N

             Fmod = -2*Fb;   %N
             Fmodnotaus = -2*Fbnotaus;   %N
             Fmodnoms = -2*Fbnoms;   %N
             Fmodnom2m3ms = -2*Fbnom2m3ms;   %N
             Fmodfourm2 = -2*Fbfourm2;   %N
             Fmodfourthms = -2*Fbfourthms;   %N

             meanFmod(i) = mean(Fmod);
             meanFmodnotaus(i) = mean(Fmodnotaus);
             meanFmodnoms(i) = mean(Fmodnoms);
             meanFmodnom2m3ms(i) = mean(Fmodnom2m3ms);
             meanFmodfourm2(i) = mean(Fmodfourm2);
             meanFmodfourthms(i) = mean(Fmodfourthms);

             medianFmod(i) = median(Fmod);
             medianFmodnotaus(i) = median(Fmodnotaus);
             medianFmodnoms(i) = median(Fmodnoms);
             medianFmodnom2m3ms(i) = median(Fmodnom2m3ms);
             medianFmodfourm2(i) = median(Fmodfourm2);
             medianFmodfourthms(i) = median(Fmodfourthms);

             ampFmod(i) = max(Fmod) - min(Fmod);
             ampFmodnotaus(i) = max(Fmodnotaus) - min(Fmodnotaus);
             ampFmodnoms(i) = max(Fmodnoms) - min(Fmodnoms);
             ampFmodnom2m3ms(i) = max(Fmodnom2m3ms) - min(Fmodnom2m3ms);
             ampFmodfourm2(i) = max(Fmodfourm2) - min(Fmodfourm2);
             ampFmodfourthms(i) = max(Fmodfourthms) - min(Fmodfourthms);
          end

          configstr = strcat('\bfMech.',{' '},config,{' '},mechnum,'\rm');

          figure
          subplot(211)
          plot3 = plot(w,meanFmod,'k',w,meanFmodnoms,'k-',w,meanFmodnom2m3ms,'k-
.',w,meanFmodfourm2,'k--',w,meanFmodfourthms,'k:',w,meanFmodnotaus,'k-.');
          set(plot3(1),'LineWidth',1.5)  %triple the size of meanFmod line
          set(plot3(6),'LineWidth',1.5)  %triple the size of meanFmodnotaus line
          ylabel('mean force (\itN\rm)')
```

```
           if j ~= 1
              title(configstr)
           end
           %axis([0 endw 38 46])
           V = axis;
           axis([0 endw V(3) V(4)])
           subplot(212)
           plot5 = plot(w,ampFmod,'k',w,ampFmodnoms,'k-',w,ampFmodnom2m3ms,'k-
.',w,ampFmodfourm2,'k--',w,ampFmodfourthms,'k:',w,ampFmodnotaus,'k-.');
           set(plot5(1),'LineWidth',1.5)  %triple the size of ampFmod line
           set(plot5(6),'LineWidth',1.5)  %triple the size of ampFmodnotaus line
           ylabel('peak-to-peak force (\itN\rm)')
           xlabel('\omega (\itrad\rm/\its\rm)')
           legend('Modeled_{ }^{ }','Modeled w/ \itm\rm_{\its\rm} = 0','Modeled w/
\itm\rm_2 = \itm\rm_3 = \itm\rm_{\its\rm} = 0','Modeled w/ \itm\rm_2 = 4\itm\rm_2','Modeled
w/ \itm\rm_{\its\rm} = (1/4)\itm\rm_{\its\rm}','Modeled w/ \tau_{\itC\rm} =
\tau_{\itum\rm} = 0',4)
           axis([0 endw yminlst(j) ymaxlst(j)])

           figure
           subplot(211)
           plot3 = plot(w,medianFmod,'k',w,medianFmodnoms,'k-',w,medianFmodnom2m3ms,'k-
.',w,medianFmodfourm2,'k--',w,medianFmodfourthms,'k:',w,medianFmodnotaus,'k-.');
           set(plot3(1),'LineWidth',1.5)  %triple the size of medianFmod line
           set(plot3(6),'LineWidth',1.5)  %triple the size of medianFmodnotaus line
           ylabel('median force (\itN\rm)')
           if j ~= 1
              title(configstr)
           end
           %axis([0 endw 38 46])
           V = axis;
           axis([0 endw V(3) V(4)])
           subplot(212)
           plot5 = plot(w,ampFmod,'k',w,ampFmodnoms,'k-',w,ampFmodnom2m3ms,'k-
.',w,ampFmodfourm2,'k--',w,ampFmodfourthms,'k:',w,ampFmodnotaus,'k-.');
           set(plot5(1),'LineWidth',1.5)  %triple the size of ampFmod line
           set(plot5(6),'LineWidth',1.5)  %triple the size of ampFmodnotaus line
           ylabel('peak-to-peak force (\itN\rm)')
           xlabel('\omega (\itrad\rm/\its\rm)')
           legend('Modeled_{ }^{ }','Modeled w/ \itm\rm_{\its\rm} = 0','Modeled w/
\itm\rm_2 = \itm\rm_3 = \itm\rm_{\its\rm} = 0','Modeled w/ \itm\rm_2 = 4\itm\rm_2','Modeled
w/ \itm\rm_{\its\rm} = (1/4)\itm\rm_{\its\rm}','Modeled w/ \tau_{\itC\rm} =
\tau_{\itum\rm} = 0',4)
           axis([0 endw yminlst(j) ymaxlst(j)])

           saveplot = 1;
           if saveplot
              figfilestr = strcat('savedplots\',char(direct),'\','frequencyplots')
              print(gcf,'-deps',figfilestr)
           end
        end




        function [ret_theta2,ret_theta2d,ret_theta2dd] = gettheta2s(paramlen,t,xb)

        % Input:  t, xb(t), r2, r3, r6.
        % Output:  theta2(t), theta2d(t), and theta2dd(t), numerically calculates time
derivatives.

        r2 = paramlen(1);
        r3 = paramlen(2);
```

```
        r6 = paramlen(3);

        N = length(t);
        dt = (t(N) - t(1))/(N-1);

        useequationmethod = 1;
        if useequationmethod
           theta2 = zeros(1,N);
           for i = 1:N
              theta2(i) = acos(1/2*(xb(i)^2-2*xb(i)*r6+r6^2+r2^2-r3^2)/(r2*(xb(i)-r6)));
           end
        end

        usesecantmethod = 0;  %quickly becoming outdated for quick code
        if usesecantmethod
           % generate plot for secant method's initial guess at t0
           %xb_val = xb(1);
           %theta2_tmp = 0:pi/100:pi;
           %f = (r2*cos(theta2_tmp) + (r3^2 - r2^2*(sin(theta2_tmp)).^2).^(1/2) + r6) -
xb_val;
           %theta2_tmp_deg = theta2_tmp*180/pi;
           %figure
           %plot(theta2_tmp_deg,f)
           %xlabel('theta2 tmp deg')
           %ylabel('f(theta2 tmp deg)')
           %grid

           guess(1) = 20;
           guess(2) = 21;

           % convert guess to radians
           guess(1) = guess(1)*pi/180;
           guess(2) = guess(2)*pi/180;

           % fid = fopen('out.txt','a');

           for r = 1:N
              xb_val = xb(r);

              %secant method
              tol = 1e-9;
              err = 100;
              idx = 3;
              while err > tol
                 num = ((guess(idx-1) - guess(idx-2))*func(guess(idx-1),xb_val,paramlen));
                 denom = (func(guess(idx-1),xb_val,paramlen)-func(guess(idx-
2),xb_val,paramlen));
                 guess(idx) = guess(idx-1) - num/denom;
                 % fprintf(fid,'iter = %g, denom = %g\n', r, denom);
                 err = abs(guess(idx)-guess(idx-1));
                 idx = idx + 1;
              end
              theta2(r) = guess(idx-1);
              % fprintf(fid,'guess(1) = %g, guess(2) = %g\n',guess(1),guess(2));
           end
           % fclose(fid);
        end


        % get theta2d and theta2dd using centered differences,
        % and extrapolate for end points

        % test when theta2 simple
```

```
        % theta2 = sin(t);

        % first derivative
        theta2d(2:N-1) = (theta2(3:N) - theta2(1:N-2))/(2*dt);
        theta2d(1) = extrap(t(2:3),theta2d(2:3),t(1));
        theta2d(N) = extrap(t(N-2:N-1),theta2d(N-2:N-1),t(N));

        % second derivative
        theta2dd(2:N-1) = (theta2(3:N) + theta2(1:N-2) - 2*theta2(2:N-1))/dt^2;
        theta2dd(1) = extrap(t(2:3),theta2dd(2:3),t(1));
        theta2dd(N) = extrap(t(N-2:N-1),theta2dd(N-2:N-1),t(N));

        ret_theta2 = theta2;
        ret_theta2d = theta2d;
        ret_theta2dd = theta2dd;



        function [tauFb,pxbptheta2] = eqofmotion(parameom,theta2,theta2d,theta2dd)

        %units: tauFb in Newton-meters, pxbptheta2 in meters

        r2 = parameom(1);
        r3 = parameom(2);
        m2 = parameom(3);
        m3 = parameom(4);
        ms = parameom(5);
        k1 = parameom(6);
        k2 = parameom(7);
        k3 = parameom(8);
        N = parameom(9);

        xi = zeros(1,N);
        staticterm = zeros(1,N);
        tauFb = zeros(1,N);
        pxbptheta2 = zeros(1,N);  %partial of xb w/ respect to theta2
        for i = 1:N
           xi(i) = r3^2-r2^2*sin(theta2(i))^2;
        end
        for i = 1:N
           staticterm(i) = k1*theta2(i) + k2*(theta2(i)+asin(r2/
r3*sin(theta2(i))))*(1+r2*cos(theta2(i))/sqrt(xi(i))) + k3*asin(r2*sin(theta2(i))/
r3)*r2*cos(theta2(i))/(sqrt(xi(i)));
        end
        for i = 1:N
           tauFb(i) = ((sin(theta2(i))^3*cos(theta2(i))^3*r2^6/
(xi(i)^2)+sin(theta2(i))^3*cos(theta2(i))^2*r2^5/(xi(i)^(3/2))-
sin(theta2(i))^3*cos(theta2(i))*r2^4/xi(i)+sin(theta2(i))*cos(theta2(i))^3*r2^4/
xi(i)+2*sin(theta2(i))*cos(theta2(i))^2*r2^3/(sqrt(xi(i)))-sin(theta2(i))^3*r2^3/
(sqrt(xi(i)))+cos(theta2(i))*sin(theta2(i))*r2^2)*ms+(1/
2*sin(theta2(i))^3*cos(theta2(i))^2*r2^5/(xi(i)^(3/2))+1/
3*r3^2*cos(theta2(i))^3*sin(theta2(i))*r2^4/(xi(i)^2)-1/2*sin(theta2(i))^3*r2^3/
(sqrt(xi(i)))+sin(theta2(i))*cos(theta2(i))^2*r2^3/
(sqrt(xi(i)))+cos(theta2(i))*sin(theta2(i))*r2^2-1/
3*r3^2*cos(theta2(i))*sin(theta2(i))*r2^2/xi(i))*m3)*theta2d(i)^2+(1/
3*m2*r2^2+(sin(theta2(i))^2*cos(theta2(i))^2*r2^4/
xi(i)+2*sin(theta2(i))^2*cos(theta2(i))*r2^3/
(sqrt(xi(i)))+sin(theta2(i))^2*r2^2)*ms+(sin(theta2(i))^2*cos(theta2(i))*r2^3/
(sqrt(xi(i)))+r2^2+1/3*r3^2*cos(theta2(i))^2*r2^2/xi(i)-
cos(theta2(i))^2*r2^2)*m3)*theta2dd(i)+staticterm(i);
           pxbptheta2(i) = -r2*sin(theta2(i))-r2^2*sin(theta2(i))*cos(theta2(i))/
(sqrt(r3^2-r2^2*sin(theta2(i))^2));
        end
```

```
function yi = extrap(x,y,xi)

% linear extrapolates a point, given two other points
% (uses same syntax as interp1)

% passes tests for equally spaced x-grid points

yi = (xi - x(1))*(y(2)-y(1))/(x(2)-x(1)) + y(1);
```